NAVAL POSTGRADUATE SCHOOL
Monterey, California

Numerical Simulation of Drifter Response
to Labrador Sea Convection

by

R. Harcourt
L. Jiang
R. W. Garwood

February 1997

19980227 046

[DTIC QUALITY INSPECTED 8

NAVAL POSTGRADUATE SCHOOL

MONTEREY, CALIFORNIA 93943-5000
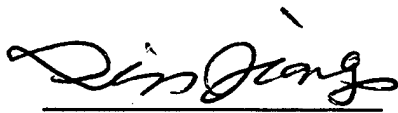
RADM Marsha J. Evans
Superintendent

This report was prepared for and funded by the Office of Naval Research , Arlington, VA 2217-5660.

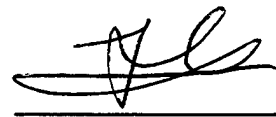Reproduction of all or part of this report is authorized.

This report was prepared by:
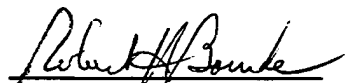

Ramsey Harcourt
Research Associate

Lin Jiang
Research Assistant Prof.

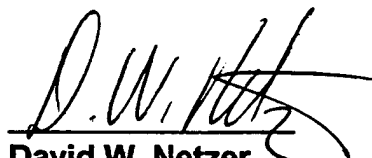Roland W. Garwood
Professor

Reviewed by:

Released by:

ROBERT H. BOURKE
Professor and Chairman
Department of Oceanography

David W. Netzer
Dean of Research

REPORT DOCUMENTATION PAGE

Form Approved OMB No. 0704-0188

1. AGENCY USE ONLY *(Leave blank)*	2. REPORT DATE February 1997	3. REPORT TYPE AND DATES COVERED Technical Report, February 1997

4. TITLE AND SUBTITLE Numerical Simulation of Drifter Response to Labrador Sea Convection	5. FUNDING NUMBERS N0001496WR30051
6. AUTHORS: Ramsey Harcourt, Lin Jiang, and R. W. Garwood	
7. PERFORMING ORGANIZATION NAME(S) AND ADDRESS(ES) Oceanography Department, Naval Postgraduate School, Monterey CA 93943-5122	8. PERFORMING ORGANIZATION REPORT NUMBER NPS-OC-98-001
9. SPONSORING/MONITORING AGENCY NAME(S) AND ADDRESS(ES): Office of Naval Research, Code 322 OM, Arlington, VA 22217-5660	10. SPONSORING/MONITORING AGENCY REPORT NUMBER

11. SUPPLEMENTARY NOTES: The views expressed in this report are those of the authors and do not reflect the official policy or position of the Department of Defense or the U.S. Government.

12a. DISTRIBUTION/AVAILABILITY STATEMENT Approved for public release; distribution is unlimited.	12b. DISTRIBUTION CODE A

13. ABSTRACT *(maximum 200 words)*

This report describes numerical simulation of two types of idealized drifters: pure Lagrangian drifters and the isobaric drifters. A large-eddy (LES) model was used to predict the fully-turbulent non-hydrostatic evolution of the oceanic flow fields that are typical of the Labrador Sea. The LES simulation indicates that either free or forced convection may dominate, depending upon the magnitudes of the wind stress and the net surface heat fluxed out of the ocean surface. Free convection predominates in the winter regimes of the periphery of the polar seas, especially in the very deeply-convecting regions of open water adjacent to marginal ice zones. Forced convection is more dominant in the stable ice-covered regions of the polar seas experiencing strong wind-stirring and kinetic energy exchange with the ice. Forced convection may be an important precursor to free convection, and the organized cells of forced convection may help dilate the ice field to enhance heat and buoyancy exchange between the OPBL and the atmosphere.

14. SUBJECT TERMS: Ocean convection, air-sea interaction, drifter simulation			15. NUMBER OF PAGES
			16. PRICE CODE
17. SECURITY CLASSIFICATION OF REPORT Unclassified	18. SECURITY CLASSIFICATION OF THIS PAGE Unclassified	19. SECURITY CLASSIFICATION OF ABSTRACT Unclassified	20. LIMITATION OF ABSTRACT UL

Approved for public release; distribution is unlimited.

TABLE OF CONTENTS

ABSTRACT

This report describes numerical simulation of two types of idealized drifters: (i) pure Lagrangian, and (ii) isobaric. A Large-Eddy Simulation (LES) model was used to predict the fully-turbulent nonhydrostatic evolution of the oceanic flow fields that are typical of the wintertime Labrador Sea with steady surface wind forcing. The LES simulation indicates that either free or forced convection may dominate, depending upon the magnitudes of the wind stress, the net surface heat fluxed out of the ocean surface, and the mixed layer depth. Free convection dominates in the winter regimes of the periphery of the polar seas, especially in the very deeply-convecting regions of open water adjacent to marginal ice zones. Forced convection is more dominant in the stable ice-covered regions of the polar seas experiencing strong wind-stirring and kinetic energy exchange with the wind and the ice. Forced convection may be an important precursor to free convection, and the organized rolls of forced convection may help dilate the ice field to enhance heat and buoyancy exchange between the oceanic planetary boundary layer (OPBL) and the atmosphere.

With the pre-computed LES velocity, pressure and salinity fields, the performance of the two drifter types is evaluated. The terms of the turbulent kinetic energy (TKE) budget, heat flux, and temperature variance observed by these drifters are evaluated and compared with the Eulerian calculations from the numerical experiments. The dissipation rate of the TKE is estimated by budget closure.

The numerical simulation indicates that the Lagrangian drifters can potentially resolve well the turbulent kinetic energy, the heat flux, and the turbulent transport, depending upon sensor accuracy on board the drifter. The Lagrangian drifter is also able to define the time-dependent vertical and horizontal scales of the convecting plumes. Compared with the Lagrangian drifters, the isobaric drifter sampling statistics are biased because these approximately fixed-depth drifters seek out convergence zones. The isobaric drifters are particularly useful for tracking more energetic convective plumes near the surface and return flow at depth. The isobaric drifters are also able to measure maximum-likely vertical velocity. A combination of Lagrangian and isobaric drifters may be best to both track the convecting plumes and to measure the heat flux correctly. The present simulation provides some new insight into the response of typical drifters to convective oceanic flow fields, and it forms a solid basis for future simulations of realistic drifters - with more specifications incorporated into the drifter models.

ACKNOWLEDGEMENTS

FIGURES

TKE transport ($\overline{w'^3}$) and the dotted line and the dot-dash line represent the components of the horizontal TKE transport $\overline{wu'^2}$ and $\overline{wv'^2}$.

1. INTRODUCTION

Labrador Sea Water, formed by deep convection, is a central component of the thermohaline circulation of the North Atlantic Ocean. It is induced by cooling and salinization of already weakly stable surface water to the point where the column mixes and entrains to great depth (Lazier, 1973; Clarke and Gascard, 1983). This cold, dense water then spreads away from the formation site and is advected into the North Atlantic. The mechanisms of the convective process remain poorly understood because they are difficult to observe and to model due to their short-period of occurrence and intermittent features [Garwood, 1991; Garwood *et al.* 1994,; Jones and Marshall, 1993; Legg and Marshall, 1994; Scott and Leaman, 1991, Arata, 1994; Bedell, 1995]. The Office of Naval Research Labrador Sea Convection experiment provides an excellent opportunity to bring together a group of scientists, both observationalists and theoretical modellers, to investigate the deep convection in the Labrador Sea and to advance our understanding of convective processes.

The immediate practical objective of this study is to simulate the observation of oceanic convection by different types of drifters. A Large-Eddy Simulation (LES) model is being used to predict the fully-turbulent nonhydrostatic evolution of the flow field, together with temperature and salinity in response to surface cooling and wind stress, typical of wintertime conditions in the Labrador Sea.

Basic types of drifters to be tested first include: (i) isobaric floats [Kearns and Rossby, 1993]; (ii) high-drag Lagrangian floats (e. g. the design of D'Asaro, personal communication, 1994; Davis, 1982, 1991; Davis *et al*, 1992). With the precomputed LES velocity, pressure, temperature and salinity fields, the performance of all of the Lagrangian Drifter Models (LDM's) and their respective sensors are evaluated. The simulation of drifter behavior is of paramount importance for the Labrador Sea field experiment, and this is the initial goal for this project. To meet this goal, we conducted a parameter range study: Rossby number-dependence for deep convection by varying parameters f, Q_o, τ, and h. A variety of LES cases

1

with different values of Coriolis parameter (f), surface forcing (Q_o and τ), and mixing depth (h) have been spun up to a statistical steady state and solutions analyzed and archived.

We conducted simulations of field observations of heat flux, vertical convective velocity, thermal variance, tracer fluxes and tracer variances, using precomputed LES fields, to determine the optimal or preferred observational strategies to best resolve the oceanic heat flux and turbulent convection as measured by the variances and covariances. Additionally, the simulated drifter time series are evaluated spectrally, for frequency response. Error analysis is a function of the drifter design and the LES model limitations due to subgrid errors associated with the subgrid parameterization of turbulent fluxes.

2. LARGE-EDDY SIMULATION

2.1. Model Description

A nonhydrostatic numerical model for high Reynolds number turbulent flow was used to predict the ocean surface velocity, pressure, temperature and salinity fields. LES, which was originally developed for application to the atmospheric boundary layer by Moeng [1984], has been adapted to prediction of nonhydrostatic deep convection [Garwood et al., 1994; Paluszkiewicz et al., 1994] by including the important thermodynamic effects for the equation of state at low temperature and high pressure [Garwood, 1991]. The Boussinesq equations plus heat and salinity budgets are used to explicitly calculate the three-dimensional large-eddy velocity, pressure, salinity, and potential temperature fields:

$$\frac{du}{dt} = -\frac{1}{\rho}\frac{\partial p}{\partial x} + fv - 2\Omega_y w + \frac{\partial \tau_{xx}}{\partial x} + \frac{\partial \tau_{xy}}{\partial y} + \frac{\partial \tau_{xz}}{\partial z} \tag{1}$$

$$\frac{dv}{dt} = -\frac{1}{\rho}\frac{\partial p}{\partial y} - fu + \frac{\partial \tau_{xy}}{\partial x} + \frac{\partial \tau_{yy}}{\partial y} + \frac{\partial \tau_{yz}}{\partial z} \tag{2}$$

$$\frac{dw}{dt} = -\frac{1}{\rho}\frac{\partial p}{\partial z} + \alpha g(\theta - \theta_0) + 2\Omega_y u + \frac{\partial \tau_{xz}}{\partial x} + \frac{\partial \tau_{yz}}{\partial y} + \frac{\partial \tau_{zz}}{\partial z} \tag{3}$$

$$\frac{\partial u}{\partial x} + \frac{\partial v}{\partial y} + \frac{\partial w}{\partial z} = 0 \tag{4}$$

2

$$\frac{dS}{dt} = \frac{\partial \tau_{sx}}{\partial x} + \frac{\partial \tau_{sy}}{\partial y} + \frac{\partial \tau_{sz}}{\partial z} \tag{5}$$

$$\frac{d\theta}{dt} = \frac{\partial \tau_{\theta x}}{\partial x} + \frac{\partial \tau_{\theta y}}{\partial y} + \frac{\partial \tau_{\theta z}}{\partial z} \tag{6}$$

Here u, v and w are the easterly, northerly and vertical velocity components, f is the vertical Coriolis parameter, and $2\Omega_y$ is the horizontal Coriolis parameter, and the total derivative is $\frac{d}{dt} = \frac{\partial}{\partial t} + u\frac{\partial}{\partial x} + v\frac{\partial}{\partial y} + w\frac{\partial}{\partial z}$. The subgrid-scale (SGS) stresses are τ_{ij}, and τ_{si} and $\tau_{\theta i}$ are the SGS salinity and temperature fluxes.

$$\tau_{ij} = K_M \left(\frac{\partial u_i}{\partial x_j} + \frac{\partial u_j}{\partial x_i} \right) \tag{7}$$

$$\tau_{si} = K_s \left(\frac{\partial S}{\partial x_i} \right) \tag{8}$$

$$\tau_{\theta i} = K_\theta \left(\frac{\partial \theta}{\partial x_i} \right) \tag{9}$$

The SGS fluxes are parameterized with eddy mixing coefficients ($K_{M,S,\theta}$) that are time- and space-dependent and calculated with second order turbulence closure, following Deardorff [1973, 1980], with

$$K_M = 0.11\lambda \sqrt{e} \tag{10}$$

and

$$K_S = K_\theta = [1 + (2\lambda)/L]K_M \tag{11}$$

The subgrid turbulent kinetic energy (TKE) length scale λ is equal to the grid scale L,

$$\lambda = L = (\Delta x \Delta y \Delta z)^{1/3} \tag{12}$$

unless the stratification is stable, when it is

$$\lambda = \lambda_s = 0.76\sqrt{e}N \tag{13}$$

3

if $\lambda_s < L$, where N is the buoyancy frequency, and e is the subgrid (unresolved) TKE. It is computed by solving the budget for subgrid TKE,

$$\frac{de}{dt} = \tau_{ij}\frac{\partial u_i}{\partial x_j} - g(\alpha\tau_{\theta3} + \beta\tau_{s3}) + \frac{\partial}{\partial x_i}\left(2K_M\frac{\partial e}{\partial x_i}\right) - \varepsilon \qquad (14)$$

where the four terms on the right of (14) are subgrid shear production, buoyancy flux, turbulent transport, and viscous dissipation. Subgrid dissipation (ε) is modeled as a function of the subgrid TKE,

$$\varepsilon = (0.19 + 0.74\lambda / L)e^{1.5} / \lambda \qquad (15)$$

The prognostic equations (1-6) for resolved scale momentum, salinity and potential temperature are solved using second order, centered finite differencing in the vertical and the pseudospectral method of Fox and Orszag [1973] in the horizontal. Time advancement is accomplished using the Adams-Bashforth scheme. More extensive details concerning the subgrid scale fluxes and the numerical method are provided by Moeng [1984] and Garwood *et al.* [1994].

For the numerical results shown here, the predicted eddy viscosity is on the order of 0.1 m^2s^{-1} or less, and the LES Reynolds number is of order 10^3 or larger. The pseudospectral method allows use of a high-wavenumber cutoff filter to define the resolved scales and to remove the small-scale aliasing without artificially damping the resolved scale motions. Thus the high Reynolds number causes a robust turbulence spectrum to be achieved that has a well defined inertial subrange with the correct -5/3 slope.

2.2. LES Simulated Convective Oceanic Flows

2.2.1. Free Convection: Rayleigh-Benard Cells

The first numerical experiment is conducted for thermally-driven winter Labrador Sea free convection, without salinity. The purpose is to provide the flows fields for the drifter performance study, and to verify the TKE budget estimates. For the purely thermal

convection in this experiment, the model domain is 6.4 km each horizontal side and is 2.05 km in the vertical, as shown in **Figure 1**. The ocean was assumed initially quiescent and horizontally homogeneous with the temperature profile typical of the Labrador Sea during winter. Convection is initiated with application of a constant upward surface heat flux of 400 W/m^2. With negligible surface wind forcing (wind speed 1 m/s), a slip condition was prescribed for the surface velocity, allowing the surface temperature field to be freely advected by the buoyancy-driven convection. Without an underlying salinity stratification, there was no loss of TKE to entrainment damping or to radiating internal waves. In strong surface cooling and freezing, the surface buoyancy flux $\overline{bw}|_0$ predominates over the wind stress (τ), and the free convection velocity scale, w_*, exceeds the friction velocity, $u_* = (\tau/\rho)^{1/2}$. The free convection velocity scale is determined by the net buoyant production of TKE in the Oceanic Planetary Boundary Layer (OPBL), $w_*^3 = \int_{-h}^{0} \overline{bw}\,dz$ (see Guest *et al*, 1995)

The LES simulation was continued for several days, until turbulence filled the model domain and a statistical equilibrium was approximated. Then drifters were released and their sampling of the thermal and velocity fields was collected for a period of about a week. **Figure 1** shows the model domain configuration and the initial locations of the drifters. The drifters are located at the center of each quadrant. The upper 4 (surface) drifters are 25 meters from the surface, the subsequent vertical interval between adjacent drifters is 50 meters. A total of 160 drifters were released. The Z axis is positive downward.

Horizontal sections showing the temperature fields and velocity fields have a considerable degree of organization. **Figure 2** shows a snapshot of the surface horizontal velocity field overlaid on the relative temperature field (detrended with the temporal mean temperature, hereafter the temperature refers to the relative temperature) at the surface. Red represents warm water and blue represents cold water. Particularly noteworthy are the organized mesoscale features that somewhat resemble Rayleigh-Benard cells [Carsey and Garwood, 1993]. Unlike Rayleigh-Benard cells, however, these are nonstationary cells that are influenced by both planetary rotation and the small scale three-dimensional turbulent vortices. The large cells are warmer and divergent, and they rotate anticyclonically. These warmer

5

regions are fed by rising water that diverges at the surface and begins to spin under the influence of Coriolis. With a maximum horizontal velocity of about 10 cm/s and a horizontal scale size (D) of about 1.5 km, the largest cells have a local Rossby number of about 0.6. The coldest near surface water lies in linear convergence lines between the expanding warm cells and has a large cyclonic vorticity that is accentuated by the vertical stretching induced by sinking. The local Rossby number of the sinking plumes is therefore much greater than unity. The lower panel of **Figure 2** shows a blow-up of the lower left corner of the flow field where the cyclonic rotation of a converging plume is evident. The relative temperature range of the drifter here is about 32 millidegrees, from -0.020°C to 0.012°C, where 0°C is the mean (relative) temperature. The temperature distribution is considerably skewed, with a significantly greater surface area of positive relative temperature than negative relative temperature.

For the Rayleigh-Benard circulation in **Figure 2**, if ice is present the pattern of divergence and convergence at the surface is also expected to enhance heat loss to the atmosphere and freezing by advecting ice away from the surface areas of divergence that are relatively warm. The orientation of the wind stress relative to the horizontal component of planetary rotation (Ω_y) has been shown to influence the depth of forced convection in other LES experiments. At the periphery of the polar seas, the magnitude of Ω_y is sufficiently large (at 60°N it is half the value at the equator), to be significant for ocean mixing and convection in response to passing atmospheric cyclones and anticyclones, with oceanic convection enhanced beneath east winds and inhibited beneath west winds [Garwood *et al.*, 1985].

Figures 3 and **4** shows snapshots of the horizontal velocity fields overlaid on the temperature field at the mid-depth (1000 m) and near the bottom (2000 m). At the mid-depth and near the bottom there exist both regions of colder sinking plumes and rising returning warmer water. The anticyclonically rotating warmer water intrudes into the colder sinking plumes. At the mid-depth the turbulence is more isotropic, and both strong cyclonic and anticyclonic eddies are evident. Also, note that the temperature range is only about 5×10^{-3} °C, but this is sufficient to support a vertical heat flux of 400 W/m^2 because of the magnitude of

the vertical velocities. Near the bottom the large cells of the cold regions represent the plumes impacting the bottom and causing anticyclonic diverging flows. Meanwhile the warmer water near the bottom rises and rotates cyclonically as illustrated by the blow-up of the temperature and velocity field. The LES simulated flow fields, together with the measurements of the Lagrangian and isobaric drifters will help to understand the transport and entrainment processes associated with these predicted features.
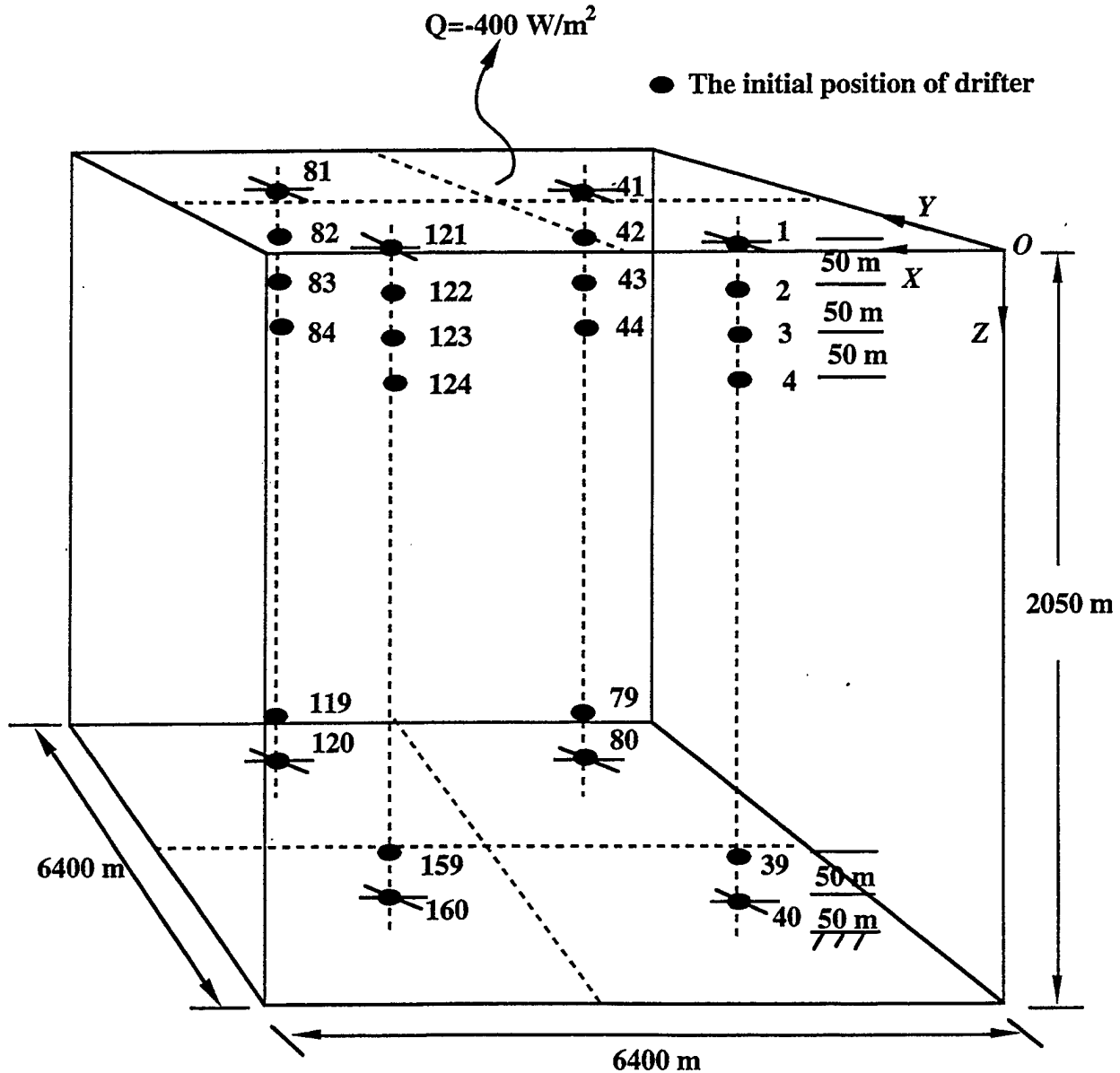
Figure 1. The schematic diagram of the model domain configuration and the initial locations of the drifters.
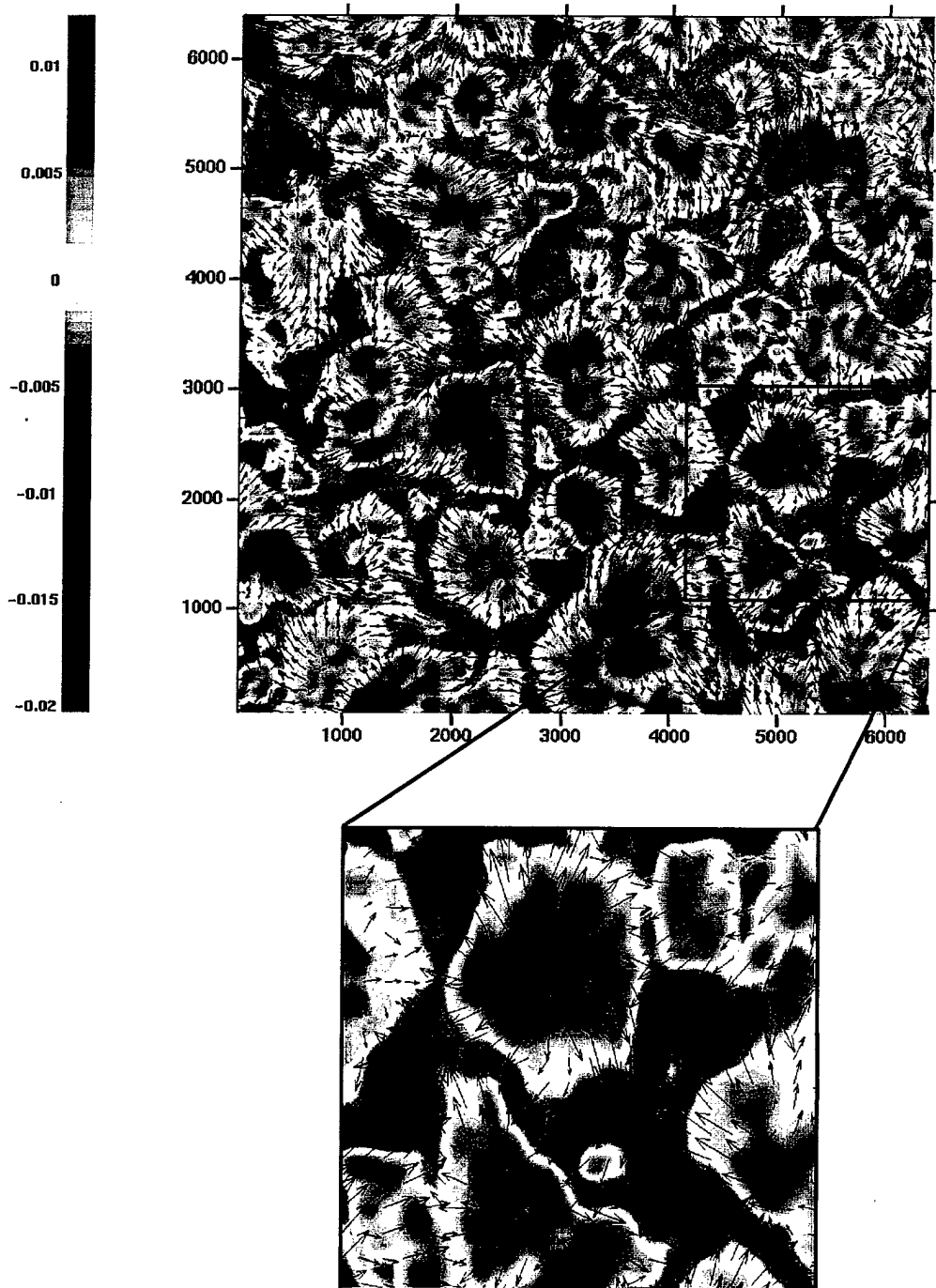
Figure 2. Snapshot of the surface, showing strong cyclonic circulation in convergence zones (blue is colder) at the edge of anticyclonic Rayleigh-Benard cells (red is warmer), forced with 400 W/m^2 heat loss and 1 m/s wind. The relative temperature scale shows that the temperature range of about 32 millidegrees.
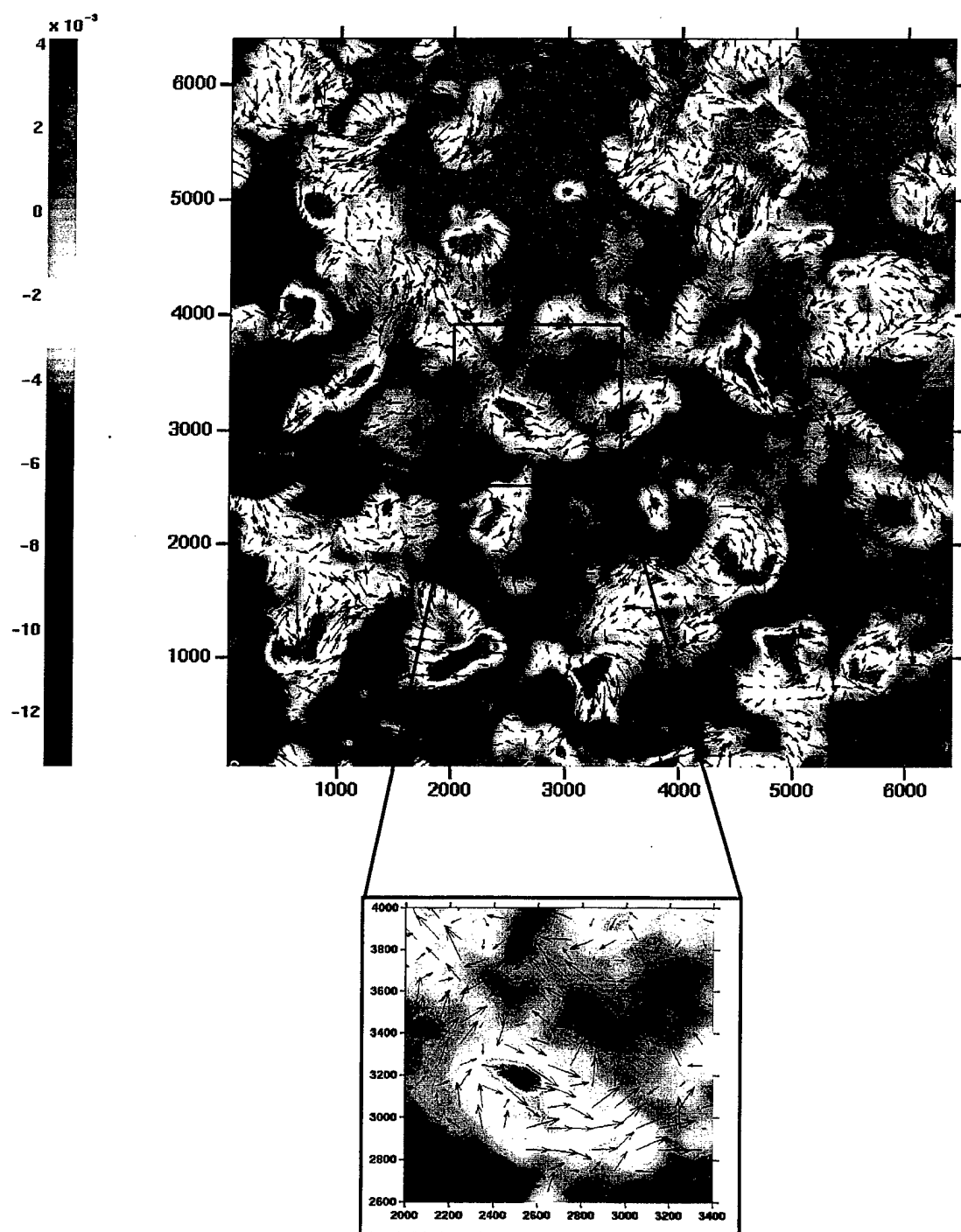
Figure 3. Snapshot of T, U, and V fields at mid-depth (1000 m) forced with 400 W/m^2 heat loss and 1 m/s wind.
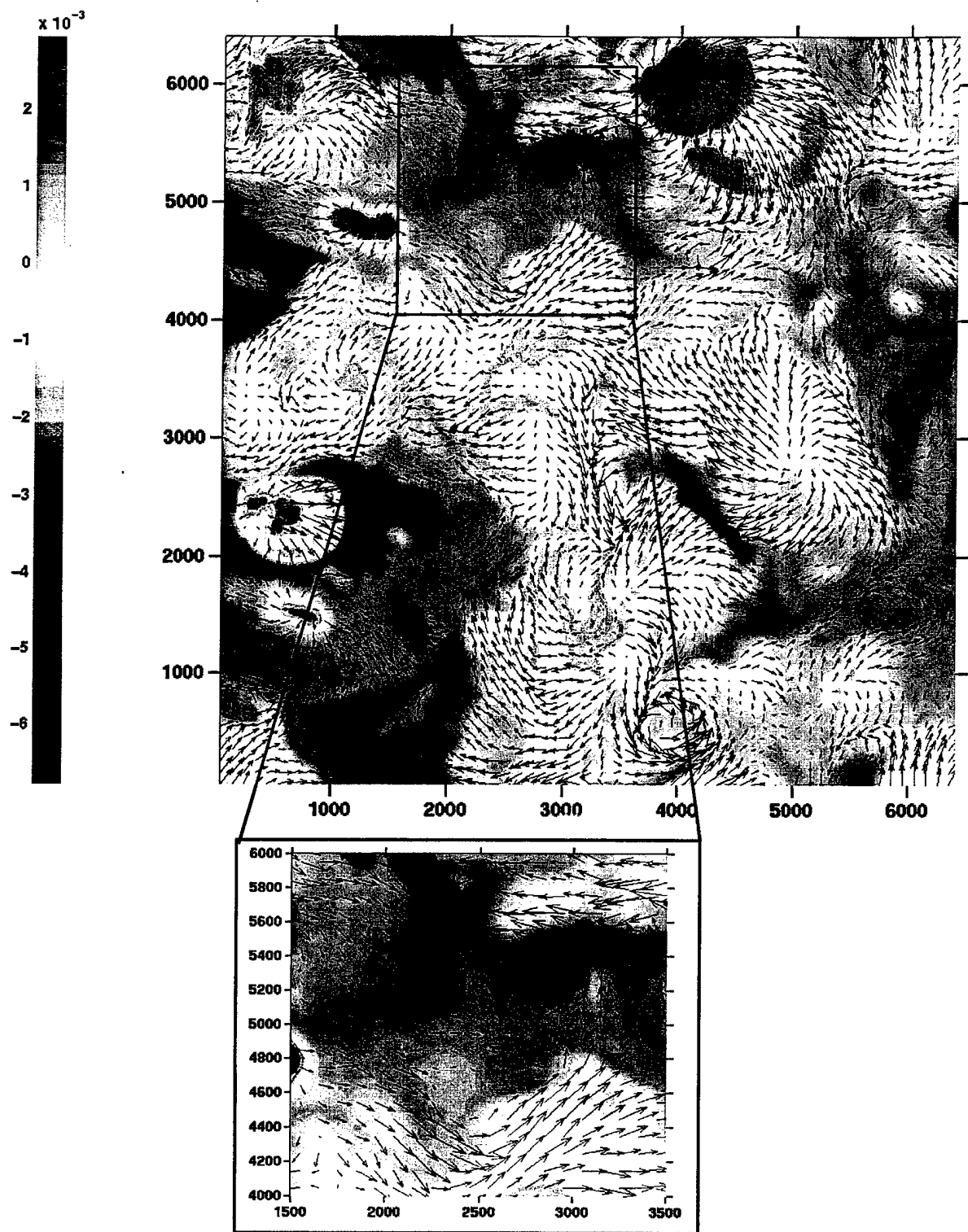
Figure 4. Snapshot of T, U, and V fields near the bottom (2000 m) forced with 400 W/m^2 heat loss and 1 m/s wind.

2.2.2. Forced Convection: Horizontal Roll Vortices

To determine the relative roles of forced (wind-driven) and free (buoyancy-driven) convection as a function of mixing depth (h), wind stress (τ), and surface cooling (Q) in deep convection regimes like the Labrador Sea, we conducted LES simulation for two cases with a combination of wind forcing and surface heat loss: (1) a surface heat loss of 400 W/m^2 and a 10 m/s wind; (2) a surface heat loss of 400 W/m^2 and a 20 m/s wind. **Table 1** shows the OPBL parameters versus depth for polar sea conditions with surface forcing of 10 m/s and 20 m/s wind speeds (u_*=1.3 m/s and 2.7 cm/s at z=10 m) and Q_o=400 W/m^2.

TABLE 1. Boundary layer parameters versus depth for Labrador Sea conditions with surface forcing of (a) 10m/s and (b) 20m/s wind speeds and surface heat loss Q_o=400 W/m^2.

wind (m/s)	depth h (m)	w_* (cm/s)	$R_o=(u_*^3+w_*^3)^{1/3}/h\Omega$	u_* (cm/s)	w_*/u_*	h/H_α
10	50	1.33	2.67	1.35	0.98	0.01
10	200	2.11	0.91	1.35	1.57	0.05
10	500	2.89	0.27	1.35	2.14	0.12
10	2000	4.75	0.19	1.35	3.53	0.47
20	50	1.33	4.44	2.69	0.49	0.01
20	200	2.11	1.22	2.69	0.78	0.05
20	500	2.89	0.56	2.69	1.07	0.12
20	2000	4.75	0.20	2.69	1.76	0.47

The increase in the thermal expansion of seawater with depth (thermobaricity) enhances TKE production and the rate of deepening of the mixed layer by normal penetrative convection [Garwood, 1991]. A thermobaricity index (h/H_α) may be defined that is a measure of the increase in the OPBL buoyancy flux due to thermal expansion increase with pressure. As Table 1 indicates, this effect is increasingly important for convection depths greater than a couple hundred meters. The scale H_α is the depth at which the thermal

expansion coefficient (α) doubles over the value at the surface. For near-freezing temperatures in the Greenland Sea, it is about 800 m, and h/H_α may exceed 2 for the deepest values of h [Garwood and Harcourt, 1997]. For the warmer Labrador Sea water, the thermobaricity effect is less important than in the Greenland Sea, and h/H_α is only about 0.5 for the deepest Labrador Sea convection.

Figures 5 and 6 show the snapshots of the T, U, and V fields, forced with 400 W/m² heat loss and with 10 m/s wind, at the surface and the mid-depth (1000 m). With a combination of a 10 m/s wind forcing and a 400 W/m² heat loss at the surface, the vertical convective velocity scale w_* is about 3.5 times the friction velocity, u_*, and the surface temperature field looks very similar to the free convection case (see Figure 2). The free convecting force dominates over the wind-forced convection and the convective flow dynamics. At mid-depth, it appears that smaller plumes are somewhat disrupted and slightly weakened; still the free convective forces dominate over the wind forcing.

In the presence of upward surface buoyancy flux, increased wind stress disrupts the Rayleigh-Benard cells, elongating them to the right (left in southern hemisphere) of the wind direction. Mixed forced and free convection yields a surface pattern of cells that is deformed downwind and to the right of the wind stress, generating horizontal roll vortices that are aligned approximately 45 degrees to the right of the wind direction. Figures 7 and 8 show the snapshots of the T, U, and V fields, forced with 400 W/m² heat loss and with 20 m/s wind, at the surface and the mid-depth (1000 m). The wind stress is in the y-direction, with $u_*=2.7$ cm/s, corresponding to a 20 m/s wind speed at 10 m above the ocean surface. The deepest blue regions are the coldest water that is converging and accelerating 45° to the right of the wind. Here w_* and u_* are about equal. Organized horizontal rolls form that are a kind of Langmuir circulation that derives its energy from the wind stress and the positive buoyancy flux. These roll vortices are analogous to the atmospheric roll vortices [Brown, 1970; Lemone, 1973], as they derive their energy from the mean shear at a free surface without surface gravity waves.
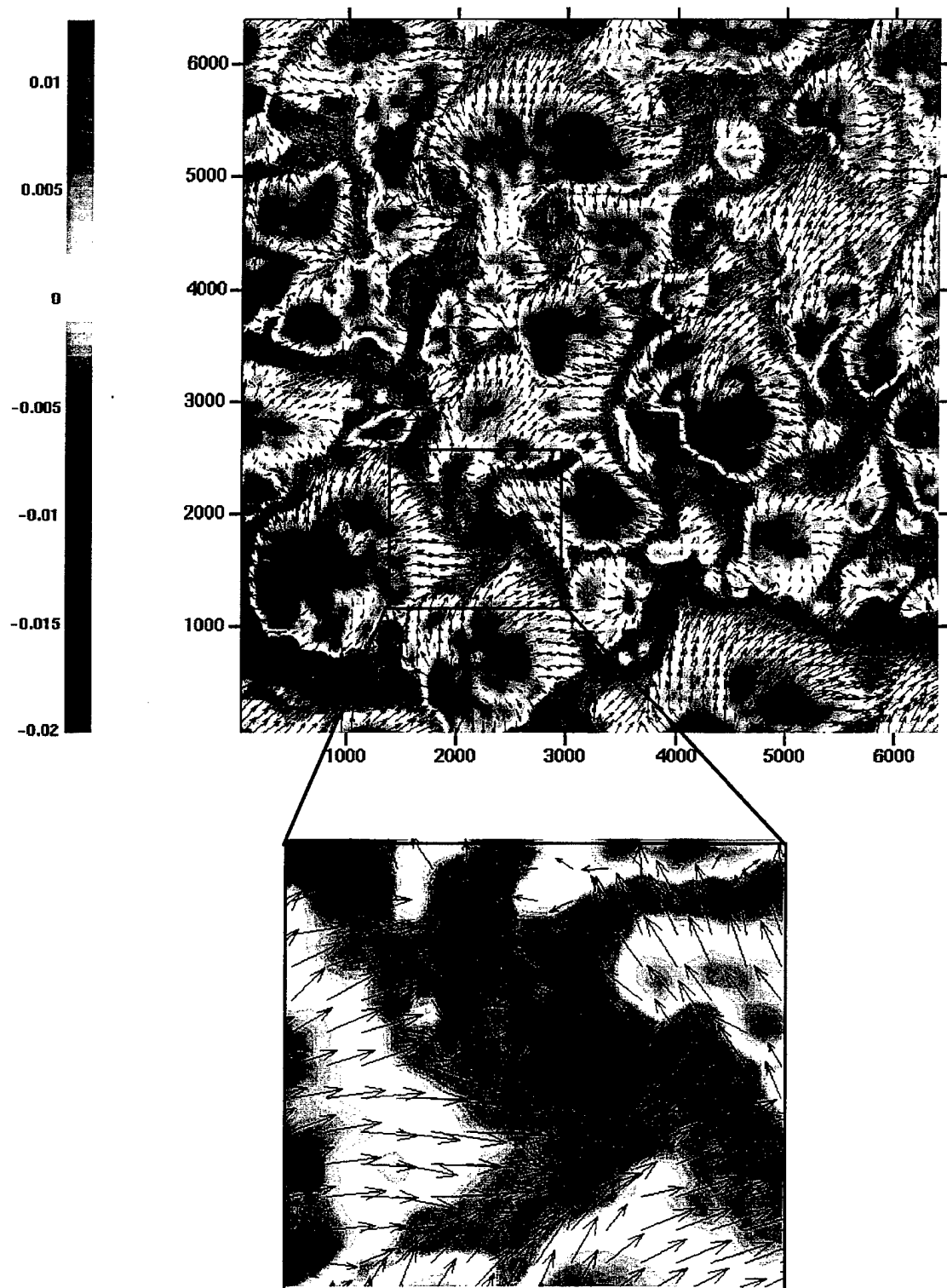
Figure 5. Snapshot of the surface T, U, and V fields, forced with 400 W/m² heat loss and 10 m/s wind.
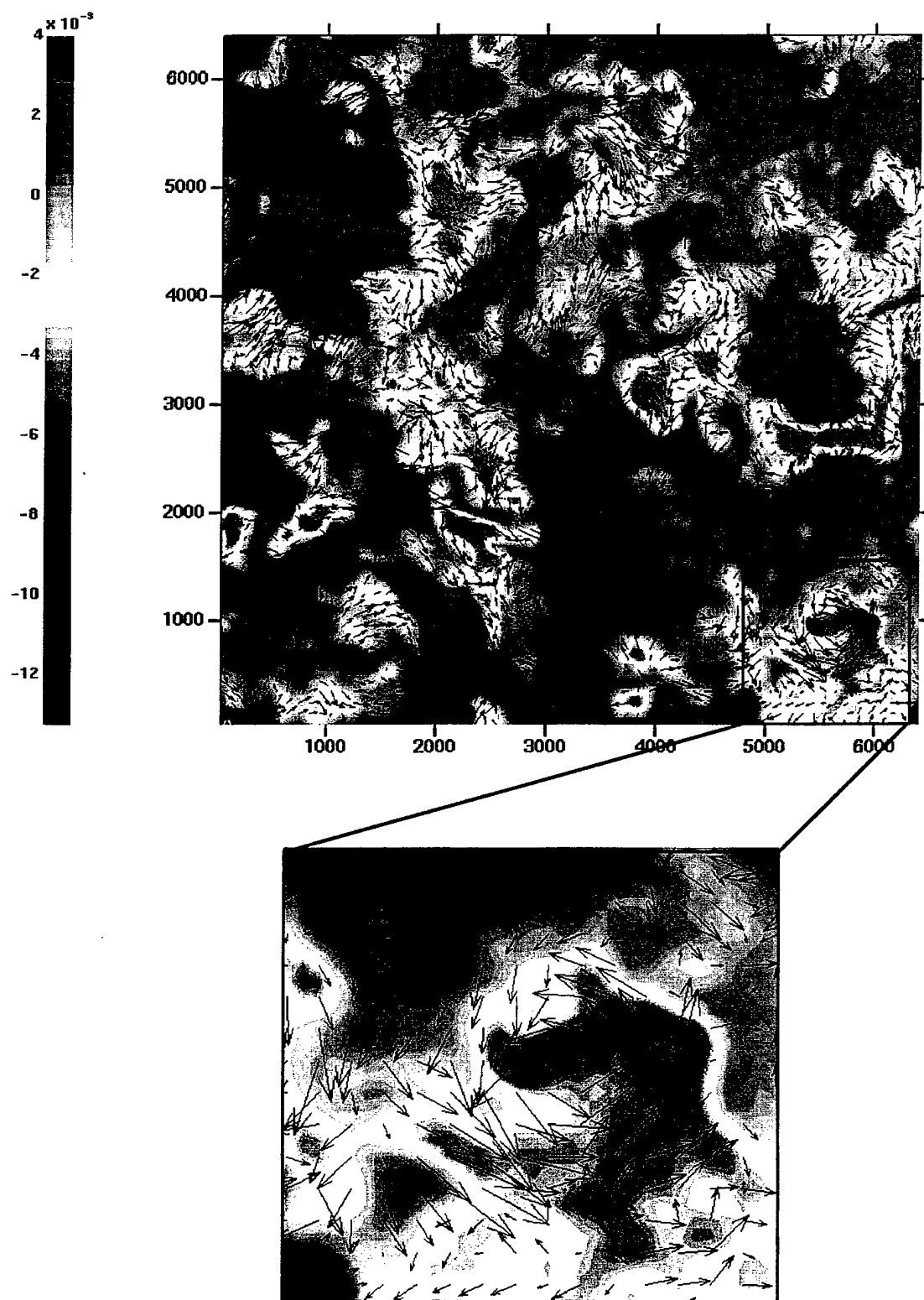
Figure 6. Snapshot of T, U, and V fields at mid-depth (1000 m), forced with 400 W/m^2 heat loss and 10 m/s wind.
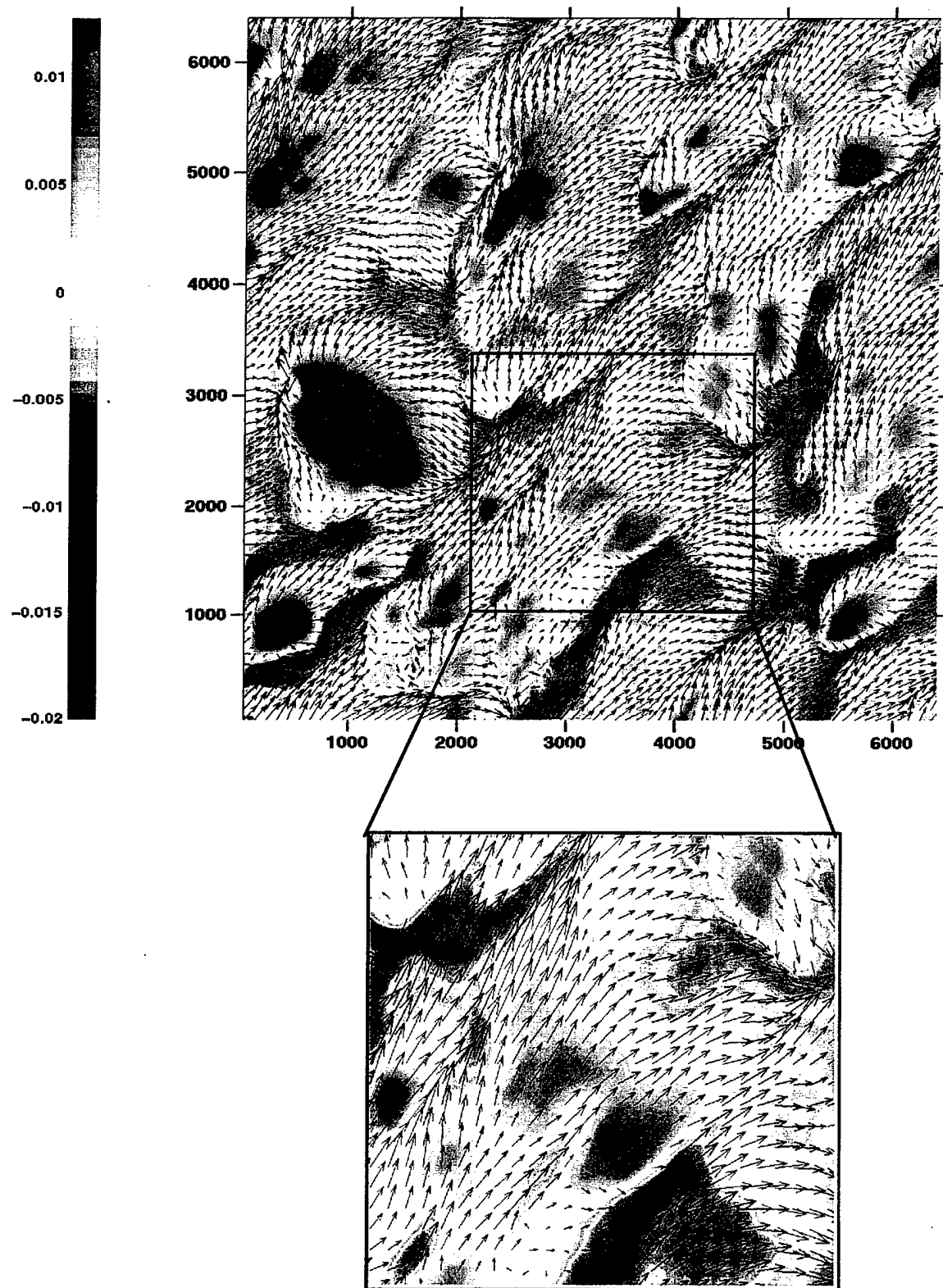
Figure 7. Snapshot of the surface T, U, and V fields, forced with 400 W/m^2 heat loss and 20 m/s wind.
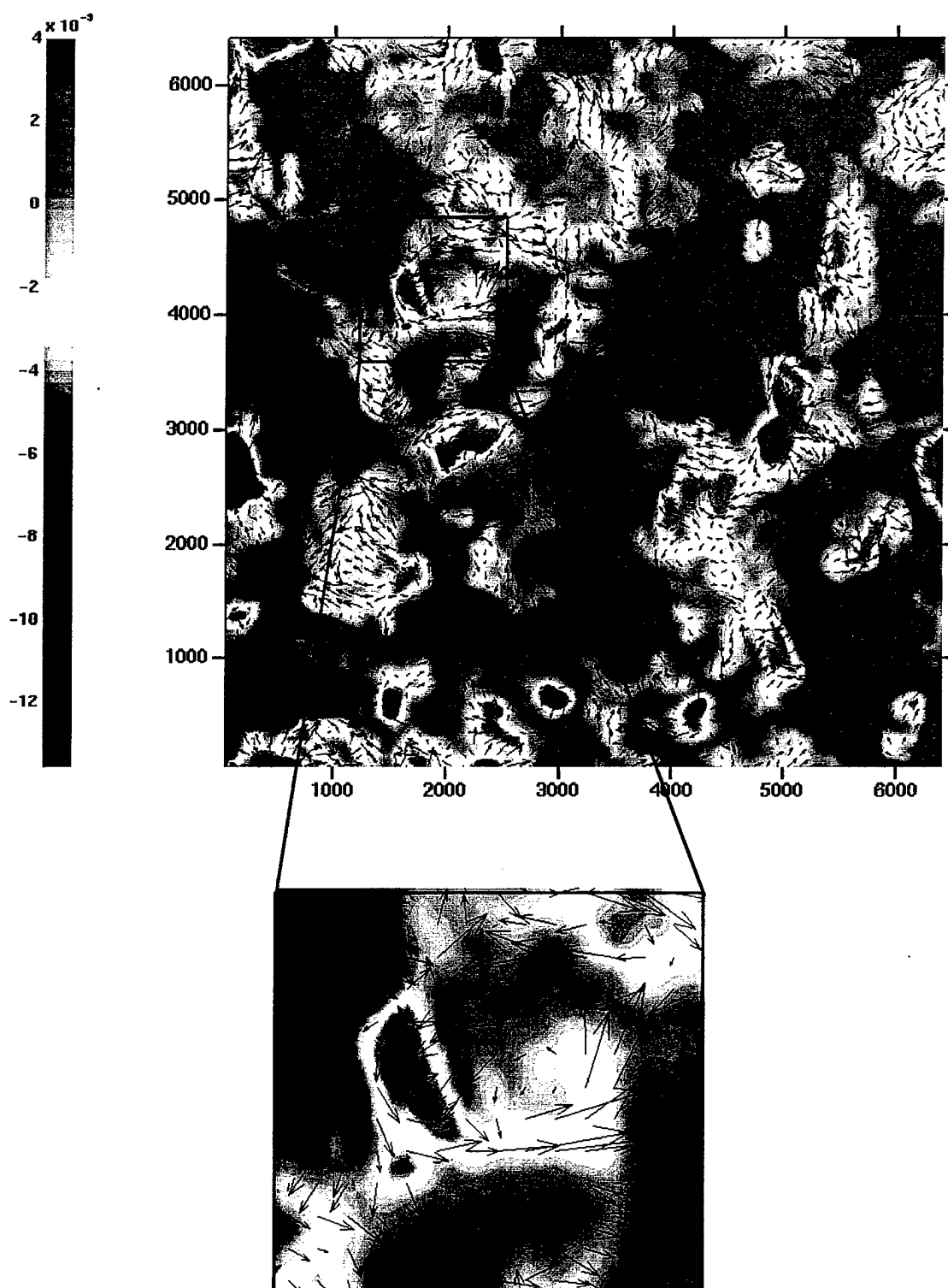
Figure 8. Snapshot of T, U, and V fields at mid-depth (1000 m), forced with 400 W/m² heat loss and 20 m/s wind.

2.2.3. Turbulent Kinetic Energy Distribution

Figure 9 shows the vertical distribution of the temporal and spatial mean of the Eulerian measurements of the TKE $\overline{(u'^2+v'^2+w'^2)}$ for the case 400 W/m² surface heat loss and (a) 1 m/s wind forcing, (b) 10 m/s wind forcing, and (c) 20 m/s wind forcing. The solid line represents the total TKE; the dashed line represents the vertical component of TKE $(\overline{w'^2})$, and the dotted line and the dot-dash line represent the horizontal components of the TKE $\overline{u'^2}$ and $\overline{v'^2}$. For all the cases the vertical TKE $\overline{w'^2}$ is very small near the surface, because the vertical TKE produced by the buoyancy flux is transported to depth, and it is also converted to horizontal TKE $\overline{(u'^2+v'^2)}$ by pressure constraints near the nonslip bottom. A maximum vertical TKE $\overline{w'^2}$ is near mid-depth (400-600 meters), with a peak root-mean-square vertical velocity of about 3 - 4 cm/s. Near the surface the horizontal turbulent kinetic energy peaks as result of the diverging and converging movement associated with the sinking plumes and upward motion of returning warmer water. The horizontal kinetic energy also has a peak near the bottom as result of the diverging movement induced by the impact of descending plumes. Wind forcing apparently increases the horizontal TKE $\overline{(u'^2+v'^2)}$ both near the surface and near the bottom. The larger the wind forcing, the larger the horizontal TKE that has been brought down to depth. Strong wind forcing, Figure 9(b), generates the largest horizontal TKE at the surface and near the bottom, and also generates the largest vertical TKE at 400-600 meters.

The vertical distribution of the temporal and spatial mean of the Eulerian measurements of the transport of the TKE $\overline{w'(u'^2+v'^2+w'^2)}$ corresponding to the three cases is shown in Figure 10 (a-c). The solid line represents the total TKE transport; the dashed line represents the vertical component of TKE transport $(\overline{w'^3})$, and the dotted line and the dot-dash line represent the horizontal components of the TKE transport $\overline{w'u'^2}$ and $\overline{w'v'^2}$. For all the three cases with different wind forcing, there are two maxima in the total TKE transport. One is shallow at around 200 - 300 meters. The other is deep at about 1200 meters. The shallow maximum of TKE transport is associated with the horizontal TKE transport which has a peak

near the surface. The deep maximum in the TKE transport is associated with strong downward transport of the vertical TKE ($\overline{w'^2}$). The horizontal TKE near the bottom is carried upward in the bottom 500 meters as a result of the rising returning warmer water that carries the TKE. The vertical transport component $\overline{w'^3}$ has a negative value at the surface as a result of the downward penetrating plumes that carries TKE downward. The $\overline{w'^3}$ term has a maximum at about 1200 meters depth; this is because the most energetic large plumes occur at mid-depth. At the bottom the w is zero and $\overline{w'^3}$ term is zero. Note that there is an upward transport of TKE due to w in the upper 50 meters. Near the very surface a very large amount of $\overline{w'^2}$ has been converted to $\overline{(u'^2 + v'^2)}$, so the large recirculating plumes actually carried TKE upward in the upper 50 meters. Surface wind forcing has significantly increased the TKE transport throughout the water column. In the 20 m/s wind case, the value of the surface TKE transport maximum surpasses that of the deep maximum due to strong shear production and turbulent mixing. Strong wind forcing also enhances the vertical transport of vertical TKE, $\overline{w'^2}$, as a result of strong wind stirring.

Turbulent Kinetic Energy (area and time averaged) versus Depth

(a) 1 m/s wind case

Figure 9. The vertical distribution of the temporal and spatial mean of the Eulerian measurements of the TKE $\overline{(u'^2+v'^2+w'^2)}$ for the cases with 400 W/m^2 heat loss and (a) 1 m/s wind, (b) 10 m/s wind, and (c) 20 m/s wind. The solid line represents the total TKE; the dashed line represents the vertical component of TKE ($\overline{w'^2}$), and the dotted line and the dot-dash line represent the horizontal components of the TKE $\overline{u'^2}$ and $\overline{v'^2}$.

Turbulent Kinetic Energy (area and time averaged) versus Depth

(b) 10 m/s wind case

Figure 9. The vertical distribution of the temporal and spatial mean of the Eulerian measurements of the TKE $\overline{(u'^2+v'^2+w'^2)}$ for the cases with 400 W/m^2 heat loss and (a) 1 m/s wind, (b) 10 m/s wind, and (c) 20 m/s wind. The solid line represents the total TKE; the dashed line represents the vertical component of TKE $(\overline{w'^2})$, and the dotted line and the dot-dash line represent the horizontal components of the TKE $\overline{u'^2}$ and $\overline{v'^2}$.

20

TKE (area and time averaged) versus Depth Z

(c) 20 m/s wind case

Figure 9. The vertical distribution of the temporal and spatial mean of the Eulerian measurements of the TKE $\overline{(u'^2+v'^2+w'^2)}$ for the cases with 400 W/m² heat loss and (a) 1 m/s wind, (b) 10 m/s wind, and (c) 20 m/s wind. The solid line represents the total TKE; the dashed line represents the vertical component of TKE ($\overline{w'^2}$), and the dotted line and the dot-dash line represent the horizontal components of the TKE $\overline{u'^2}$ and $\overline{v'^2}$.

21

TKE Transport (area and time averaged) versus Depth Z

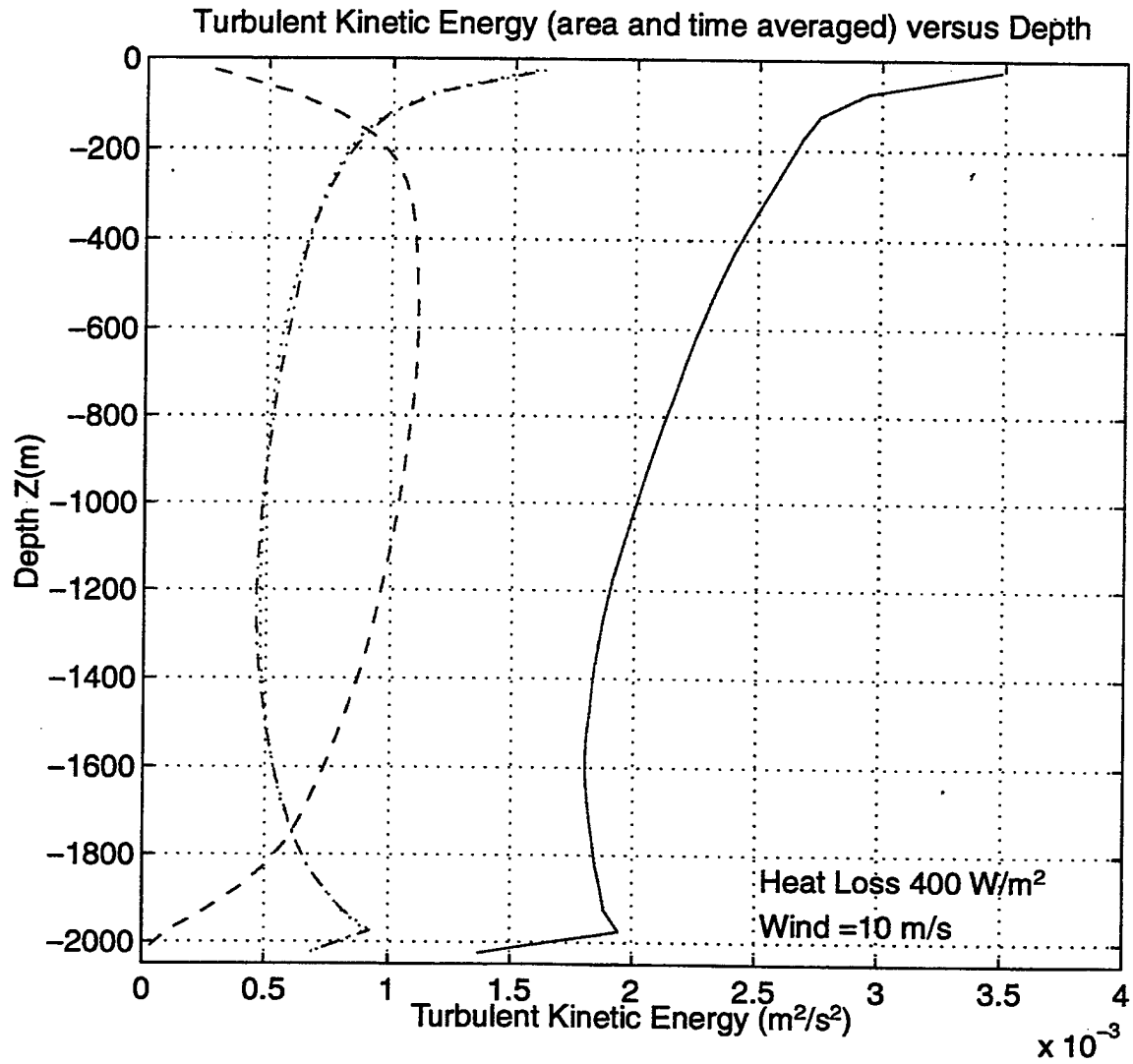Heat Loss 400 W/m²
Wind =1 m/s

(a) 1 m/s wind case

Figure 10. The vertical distribution of the temporal and spatial mean of the Eulerian measurements of the transport of the TKE $\overline{w'(u'^2+v'^2+w'^2)}$ for the cases with 400 W/m² heat loss and (a) 1 m/s wind, (b) 10 m/s wind, and (c) 20 m/s wind. The solid line represents the total TKE transport; the dashed line represents the vertical component of TKE transport $(\overline{w'^3})$, and the dotted line and the dot-dash line represent the horizontal components of the TKE transport $\overline{wu'^2}$ and $\overline{wv'^2}$.

22

TKE Transport(area and time averaged) versus Depth Z

(b) 10 m/s wind case

Figure 10. The vertical distribution of the temporal and spatial mean of the Eulerian measurements of the transport of the TKE $\overline{w'(u'^2+v'^2+w'^2)}$ for the cases with 400 W/m² heat loss and (a) 1 m/s wind, (b) 10 m/s wind, and (c) 20 m/s wind. The solid line represents the total TKE transport; the dashed line represents the vertical component of TKE transport $(\overline{w'^3})$, and the dotted line and the dot-dash line represent the horizontal components of the TKE transport $\overline{wu'^2}$ and $\overline{wv'^2}$.
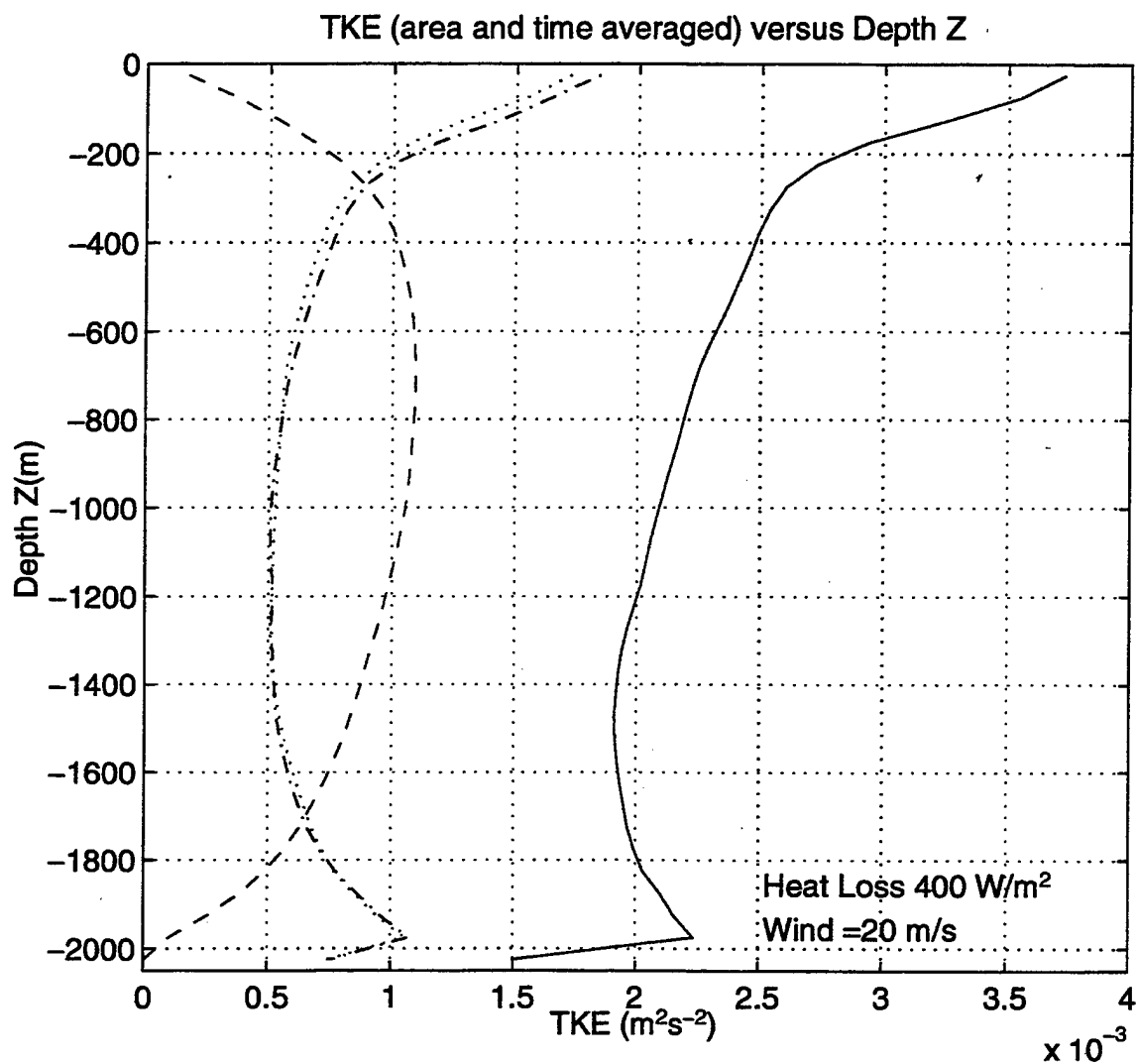
23

(c) 20 m/s wind case

Figure 10. The vertical distribution of the temporal and spatial mean of the Eulerian measurements of the transport of the TKE $\overline{w'(u'^2+v'^2+w'^2)}$ for the cases with 400 W/m^2 heat loss and (a) 1 m/s wind, (b) 10 m/s wind, and (c) 20 m/s wind. The solid line represents the total TKE transport; the dashed line represents the vertical component of TKE transport ($\overline{w'^3}$), and the dotted line and the dot-dash line represent the horizontal components of the TKE transport $\overline{wu'^2}$ and $\overline{wv'^2}$.
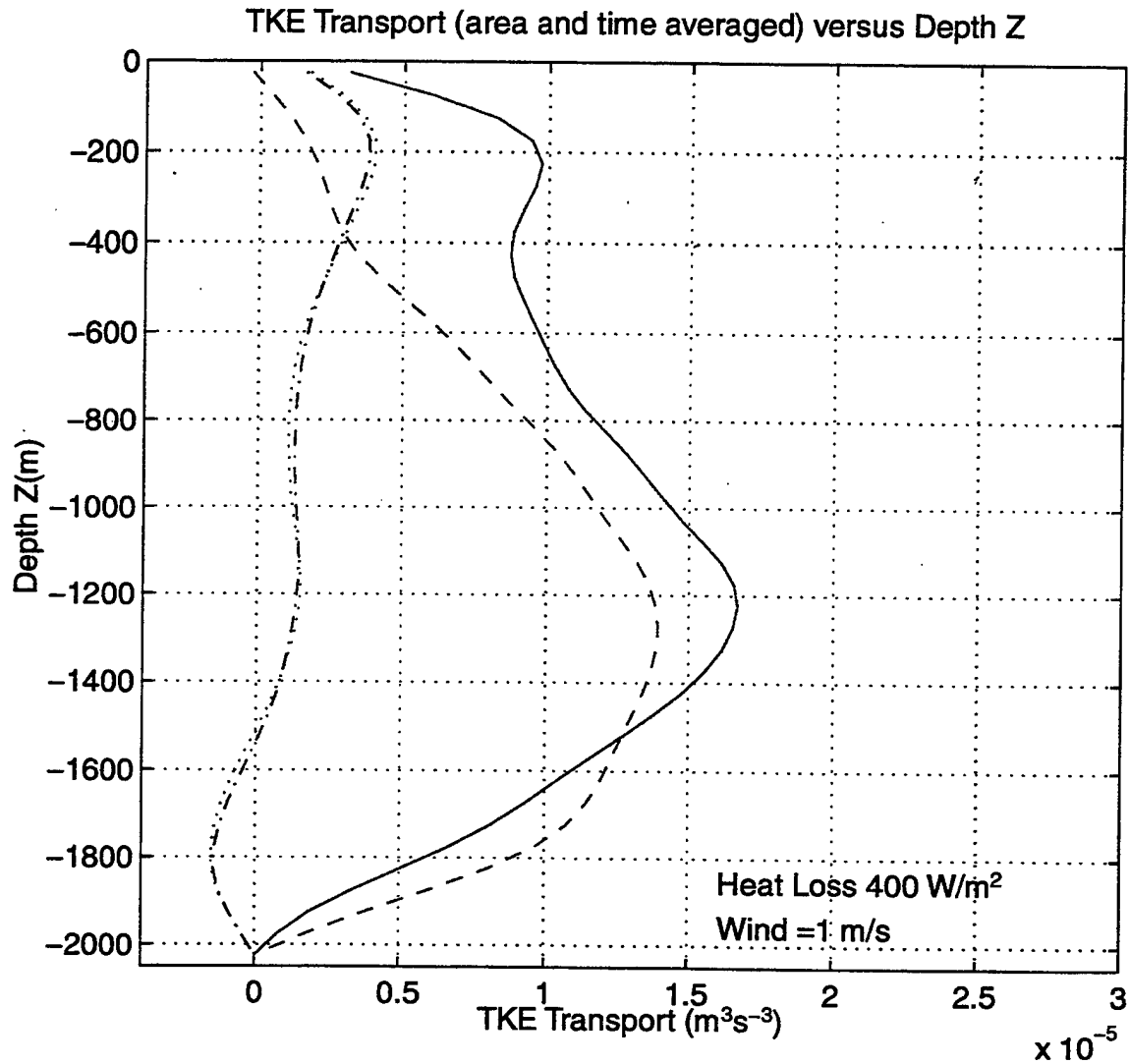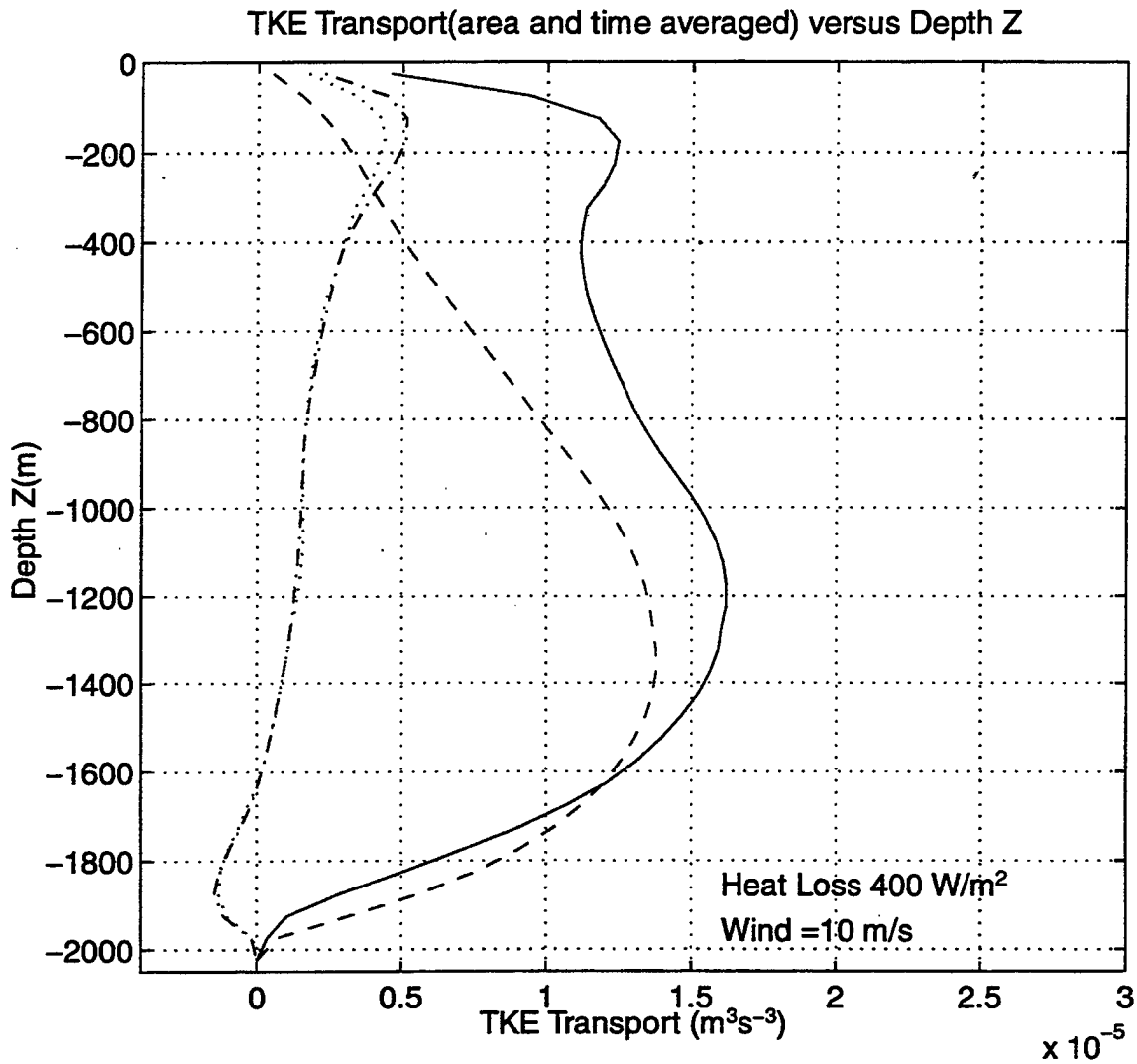
24

For the statistically steady state, the TKE balance equation reads,

$$0 = -\overline{uw}\frac{\partial \bar{u}}{\partial z} - \overline{vw}\frac{\partial \bar{u}}{\partial z} + \alpha g \overline{Tw} + \frac{\partial}{\partial}\left(\frac{\overline{w^3 + wu^2 + wv^2}}{2} + \frac{\overline{wp}}{\rho}\right) - \varepsilon \quad (16)$$

Shear Production   Buoyancy Flux   d(Transport)/dz   Pressure Term   Dissipation

Figure 11 shows the mean turbulent kinetic energy budget with 400 W/m² surface heat flux and 10 m/s wind forcing. The shear production, the buoyancy flux and the transport terms are all found by averaging the moments over the duration of the LES run (20000 time steps x 50 sec = 277 hours) on the Eulerian grid. Dissipation was calculated as a residual assuming a steady state balance.

In the resolved-scale TKE budget, the shear production is a maximum at the surface. This shear production is responsible for the deepening of the planetary boundary layer. The buoyancy flux is zero at the ocean bottom and increases to a maximum near the surface, indicating a flux of cool water downward. The turbulent transport is negative near the surface and positive near the bottom, indicating that the energy is being transported downward from the surface. At 300 m depth, however, there is an upward transport of TKE. This is because near the surface a large amount of $\overline{w'^2}$ has been converted to $\overline{(u'^2 + v'^2)}$, so the large recirculating plumes actually carried TKE upward between 200 to 400 meters. The dissipation term is computed as a residual of this analysis. The pressure transport term is assumed to be small; however, it can be computed directly. In this simulation the dissipation term is rather large and probably results from the combination of the viscous dissipation and the pressure transport term.

Figure 11. The horizontally averaged resolved scale turbulent kinetic energy budget for the case with 400 W/m² surface heat flux and 10 m/s wind forcing.

2.2.4. Heat Flux and Temperature Variance
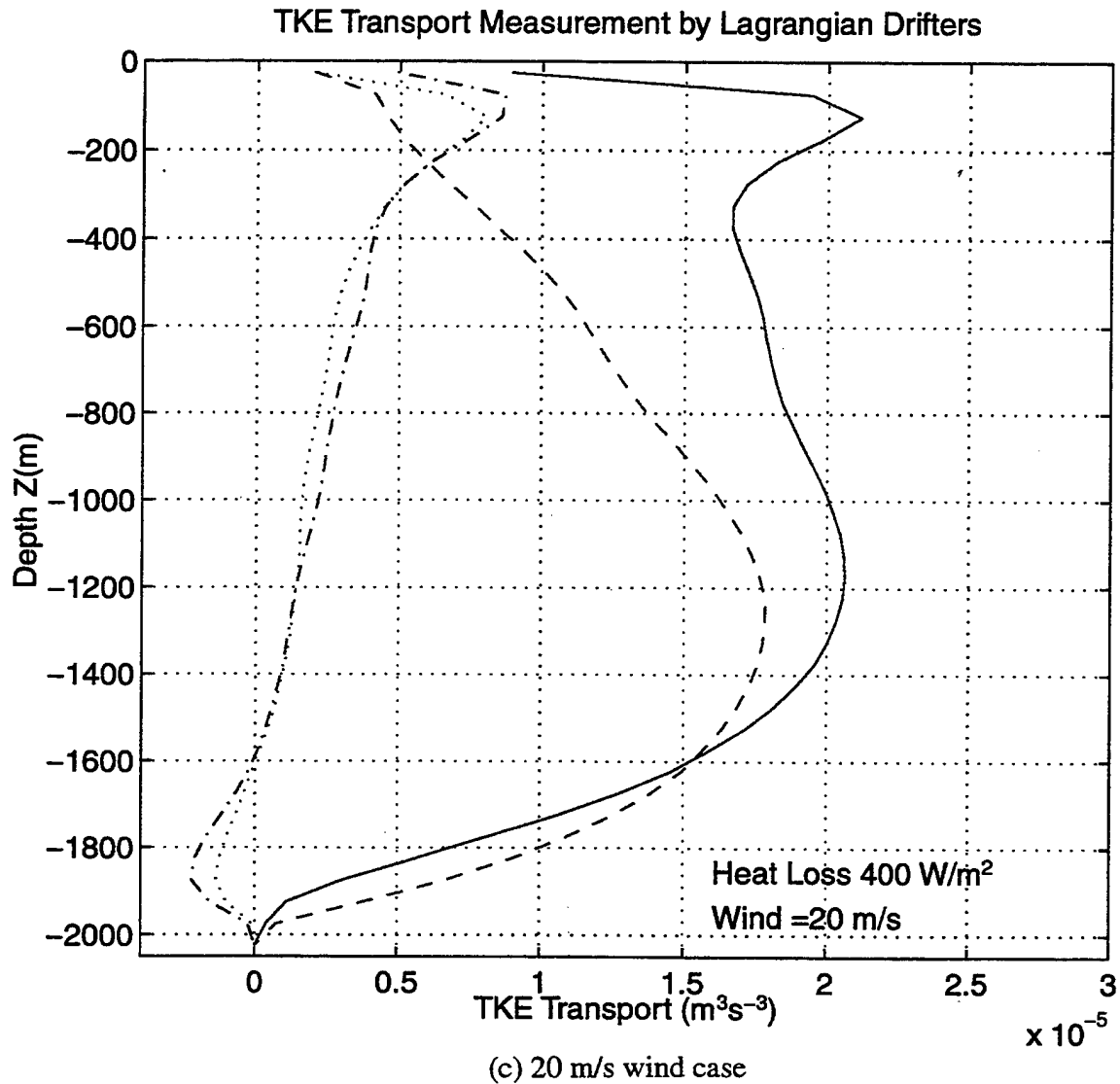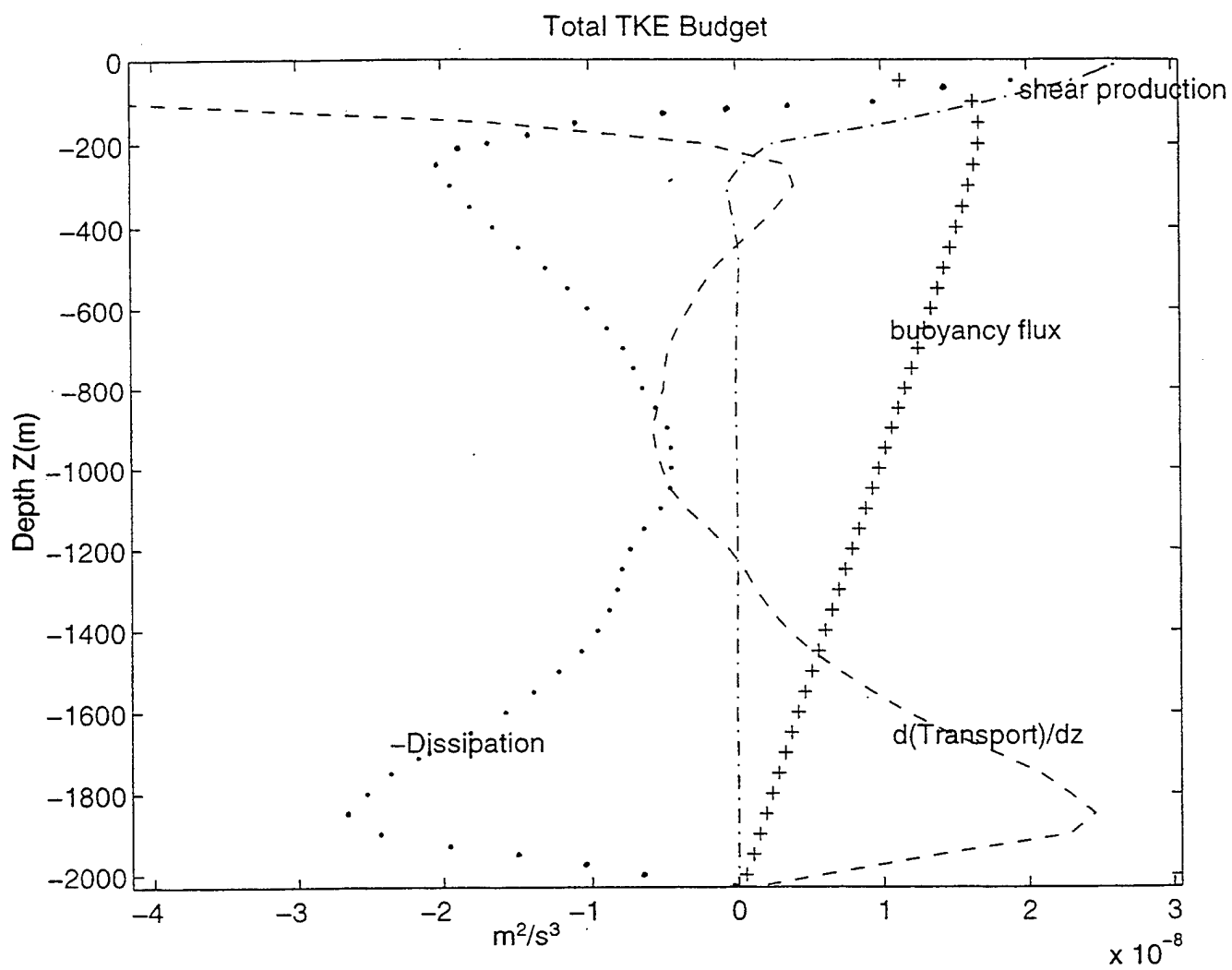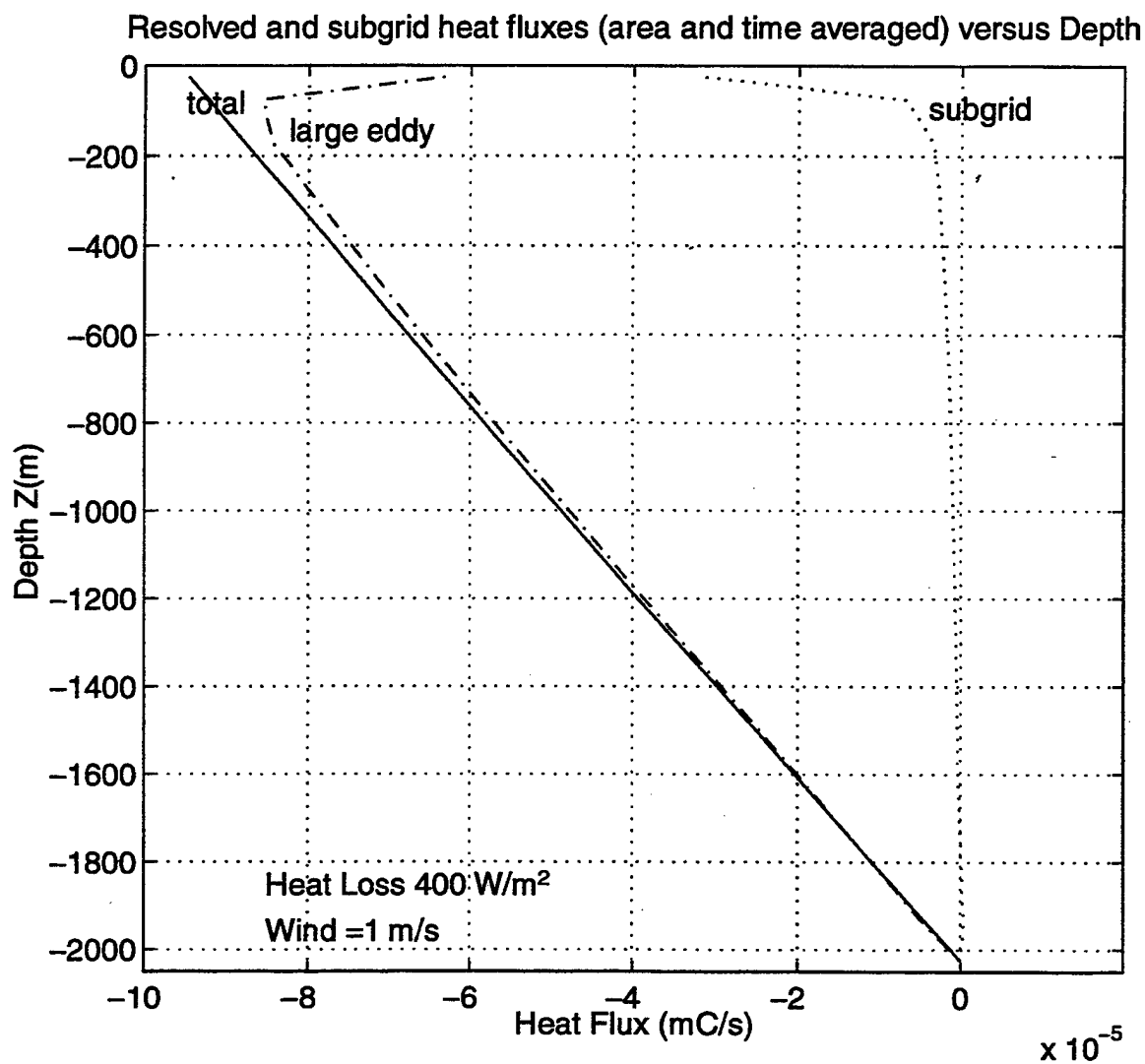
Figure 12 shows the vertical distribution of the temporal and spatial mean of the Eulerian measurements of the heat flux $\overline{w'T'}$ for the cases with 400 W/m2 heat loss and (a) 1 m/s wind, (b) 10 m/s wind, and (c) 20 m/s wind. The solid line is the total heat flux (total of resolved heat flux and subgrid heat flux), the dash-dot line represents the heat flux resolved by the LES model, and the dotted line represents the subgrid heat flux that is not resolved in the LES. In all the three case, the heat flux has a maximum at the surface and decreases linearly to a minimum at the bottom. Near the surface (upper 100 meters - the first 2 grids) large eddies are not resolved very well and subgrid flux has a maximum value. Below depth of 100 meter or so the large eddy flux is very well resolved in all the three cases. The free convection case (with 1 m/s wind forcing) has a smaller unresolved large-eddy flux near the surface than do the forced convection cases (with 10 m/s and 20 m/s wind forcing). With a larger wind (20 m/s), the not-so-well-resolved region extends down to about 200 meters.

Figure 13 shows the corresponding temperature variance $\overline{T'^2}$ versus depth for the three cases with different wind forcing. The free convection case has the largest temperature variance because the wind-induced turbulence in this case is the weakest and the temperature gradient production of temperature variance is the largest among the three cases. In the free convection case, the maximum temperature variance $\overline{T'^2}$ is 3.1×10^{-5} C^2 near the surface. It decreases drastically with depth Z. Though the temperature range is only about 5×10^{-3} °C, this is adequate to support a vertical heat flux of 400 watts/m^2 because of the magnitude of the vertical velocities. The strongest wind forcing (20 m/s) generates the smallest temperature variance near the surface, as the water column has been well mixed due to the wind. This is shown more clearly by analyzing the temperature variance budget. For the statistically steady state, the temperature variance balance equation is,

$$0 = \quad -\overline{T'w'}\frac{\partial \overline{T}}{\partial z} \quad - \quad \frac{\partial}{\partial}\left(\frac{\overline{w'T'^2}}{2}\right) \quad - \quad K_T\left(\overline{\frac{\partial T}{\partial x_i} \cdot \frac{\partial T}{\partial x_i}}\right) \qquad (17)$$

       Gradient Production   d(Transport)/dz   Dissipation

Resolved and subgrid heat fluxes (area and time averaged) versus Depth

(a) 1 m/s wind case

Figure 12. The vertical distribution of the temporal and spatial mean of the Eulerian measurements of the heat flux $\overline{w'T'}$ for the cases with 400 W/m² heat loss and (a) 1 m/s wind, (b) 10 m/s wind, and (c) 20 m/s wind.

(b) 10 m/s wind case

Figure 12. The vertical distribution of the temporal and spatial mean of the Eulerian measurements of the heat flux $\overline{w'T'}$ for the cases with 400 W/m² heat loss and (a) 1 m/s wind, (b) 10 m/s wind, and (c) 20 m/s wind.

Resolved and subgrid heat fluxes (area and time averaged) versus Depth

(c) 20 m/s wind case

Figure 12. The vertical distribution of the temporal and spatial mean of the Eulerian measurements of the heat flux $\overline{w'T'}$ for the cases with 400 W/m² heat loss and (a) 1 m/s wind, (b) 10 m/s wind, and (c) 20 m/s wind.

30

Figure 13. The vertical distribution of the temporal and spatial mean of the Eulerian measurements of the temperature variance $\overline{T'^2}$ for the cases with 400 W/m^2 heat loss and 1 m/s, 10 m/s and 20 m/s wind.

31

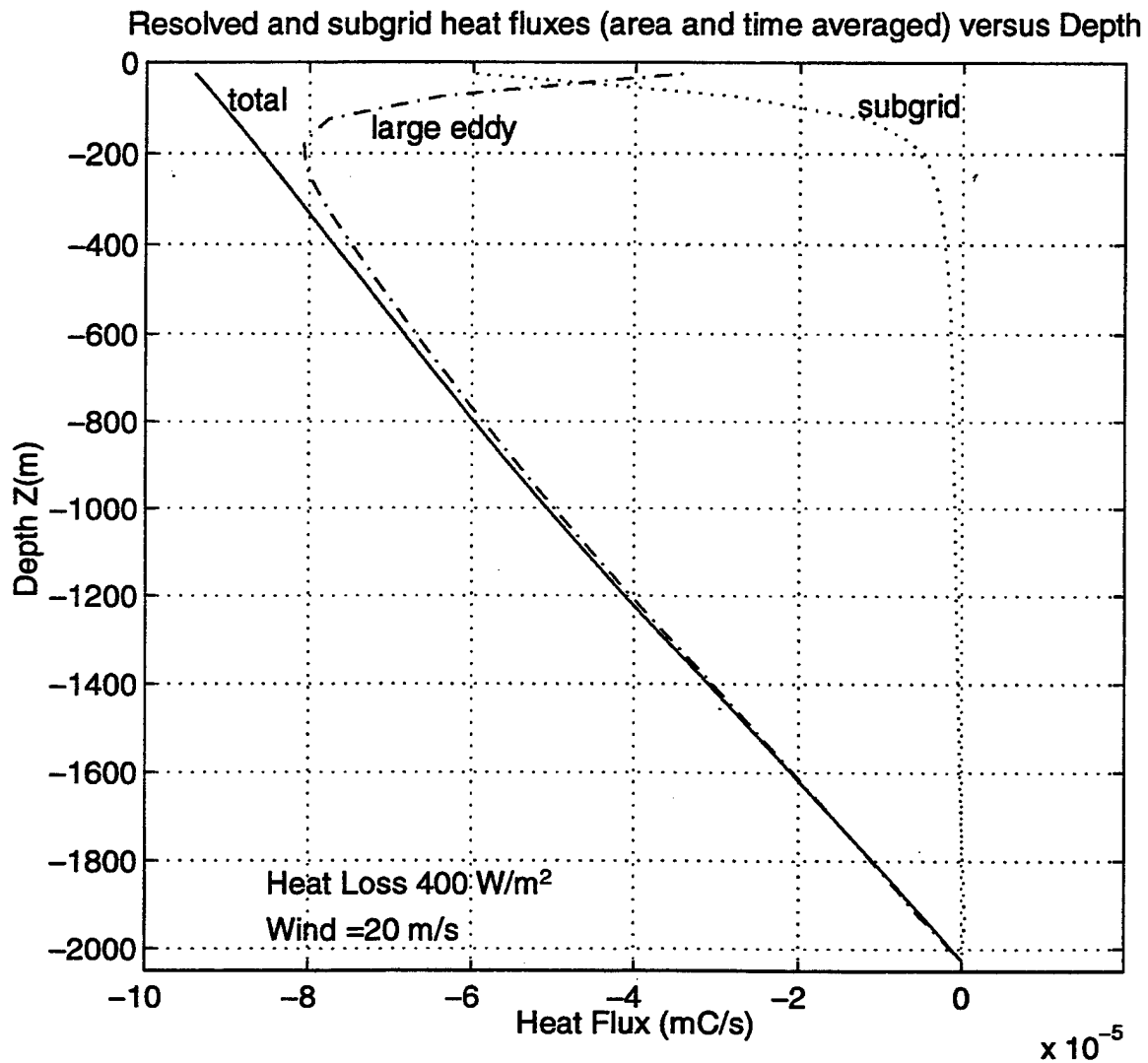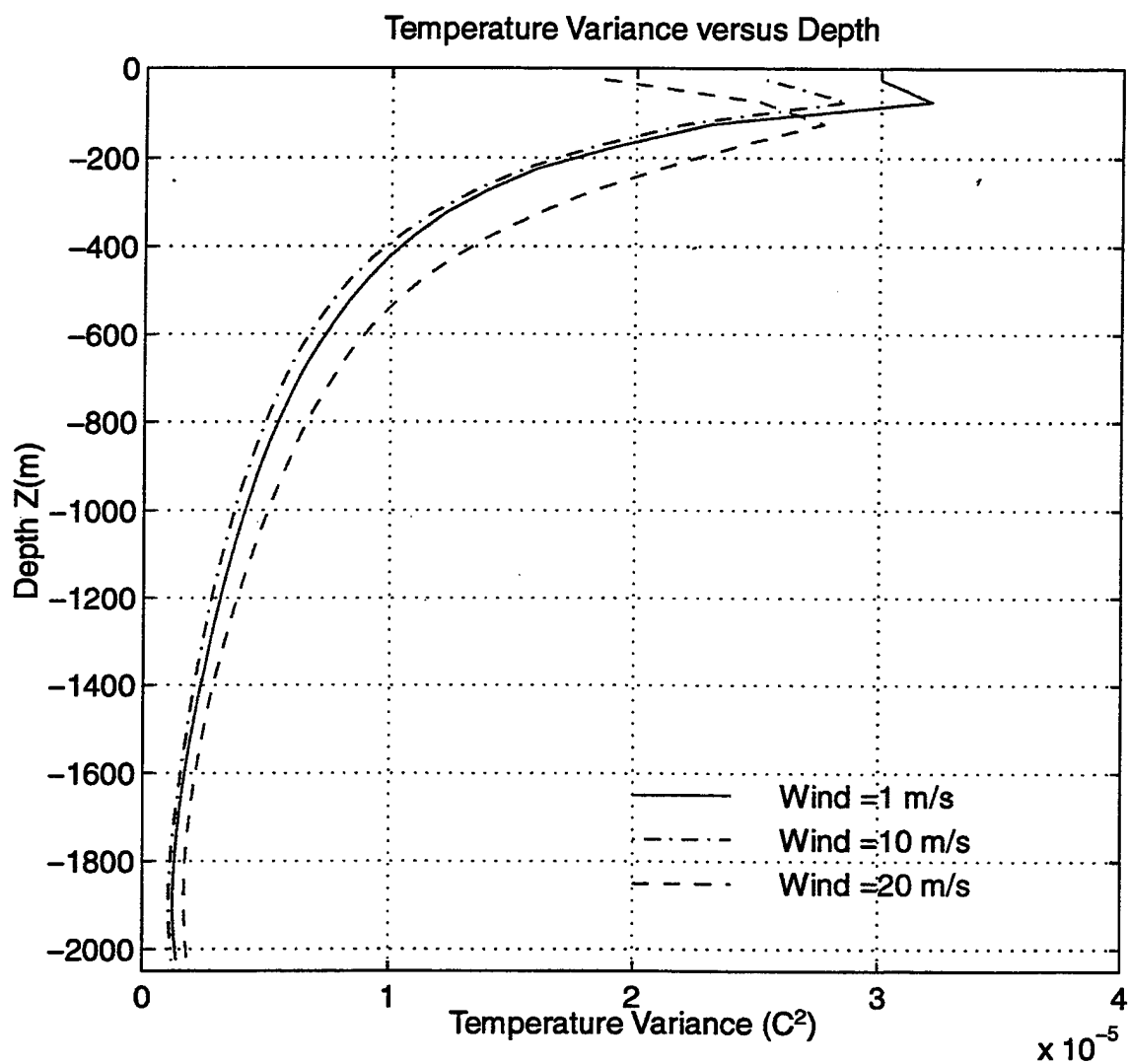# 3. RESPONSE OF DRIFTERS TO CONVECTIVE OCEANIC FLOWS

The behavior of two types of drifters, an idealized pure Lagrangian drifter and an idealized pure isobaric type of drifter, is investigated in the fully-turbulent nonhydrostatic oceanic flow fields that are typical of the Labrador Sea, forced with steady surface cooling and negligible wind forcing. The idealized Lagrangian drifter follows the water particle as a neutrally buoyant float. The idealized isobaric float follows the water particle isobarically, i.e. it is constrained to move only horizontally. With the precomputed LES velocity, pressure and salinity fields, the terms of the turbulent kinetic energy (TKE) budget observed by these drifters are evaluated and compared with the Eulerian measurements from the numerical experiments. The dissipation rate of the TKE is estimated by budget closure from the other TKE equation terms, together with the LES-predicted vertical structure to the budget. The performance of these drifters' models are compared with each other and with the Eulerian observations. We first simulated these idealized drifters to gain insight and a basic understanding of the response of these drifters to typical open convective ocean in the Labrador Sea. The findings acquired here, although idealized, provide us with important information that will later help us to simulate and understand realistic drifters' response to real forcing with real initial ocean conditions.

3.1. Lagrangian Drifter

The Lagrangian drifters are treated as neutrally buoyant floats that follow the water flow. It is expected that the Lagrangian drifter will resolve correctly the mean fields, TKE dissipation, including the mean heat flux, and the time-dependent plume geometry in the LES modeled flow fields. The Lagrangian drifters do not seek out extreme flow conditions in the fields; they follow a plume by chance. The simulated drifters can not resolve the viscous dissipation which is not resolved in the LES fields. Most of the viscous dissipation occurs at the Kolmogorov microscale, on the order of centimeters and smaller which is much less than the grid size in the LES.

3.1.1. The Drifter Trajectories

Figure 14 (a, b, c, d) shows the 3-D perspective view of the locations of Drifters #1, #12, #53, and #154, and the temperature observed by these drifters at that location for 10,000 time steps (one time step = 50 seconds, locations at every 20 time steps were plotted), for the case with 400 W/m^2 heat loss and 1 m/s wind forcing. The temperature has been detrended from the temporal mean. Red indicates the drifter moves into a warmer area and blue indicates the drifter moves into a cold area. The drifter starts from the point with a "X" mark. Drifters #1 and # 12 (Figure 14 (a) and (b)) experience cyclonic rotational downward movement during the 6-day period. The spiral movement starts near the surface as these drifters were caught in a diverging zone - a downward convective plume, as clearly shown by the temperature observation of the drifters. The spiral trajectories approximately give the scale of the descending plumes, which is in the range of 200-500 meters. Also evident in the plots are the rising returning relatively warmer water from bottom, after deflection upward from the bottom. Figure 14 (c) and (d) illustrate another type of movement of the Lagrangian drifters - fast non-rotational sinking. Little rotation is seen in the trajectories of these two drifters. Fast descent was evident as indicated by the dark blue color and the distance between the adjacent drifter positions. The second kind of drifter motion is probably a result of arrest of drifter rotation near the core of the plumes, while the first kind as result of strong shear experienced near the outer edge of the sinking plume.

In the presence of upward surface buoyancy flux, increased wind stress disrupts the Rayleigh-Benard cells. The elongation of the cells to the right of the wind direction is also evident in the surface drifter trajectories. **Figures 15 (a-b)** depicts the 3-D perspective view of the locations of Drifters #1, #12, #53, and #154, and the temperature observed by these drifters for the case with 400 W/m^2 heat loss and 20 m/s wind forcing. The elongation of the cells to the right of the wind direction is more clearly seen in the trajectories of the isobaric drifters near the surface (**Figure 22**).

33
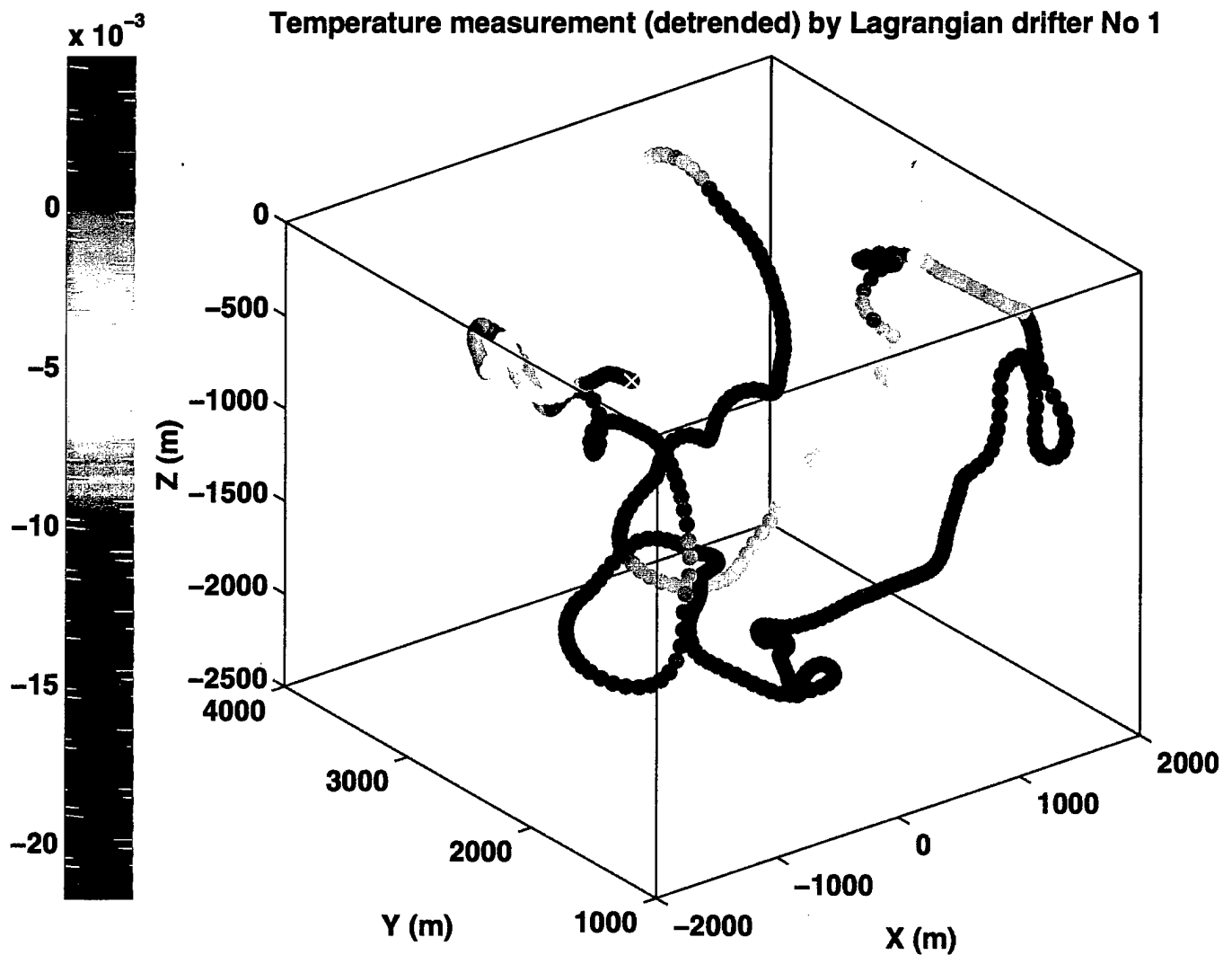
(a) Drifter #1

Figure 14. The 3-D perspective view of the locations of Drifters (a) #1, (b) #12, (c) #53, and (d) #154 and the temperature (T) observed by these drifters at that location, for the case with 400 W/m² heat loss and 1 m/s wind.

34
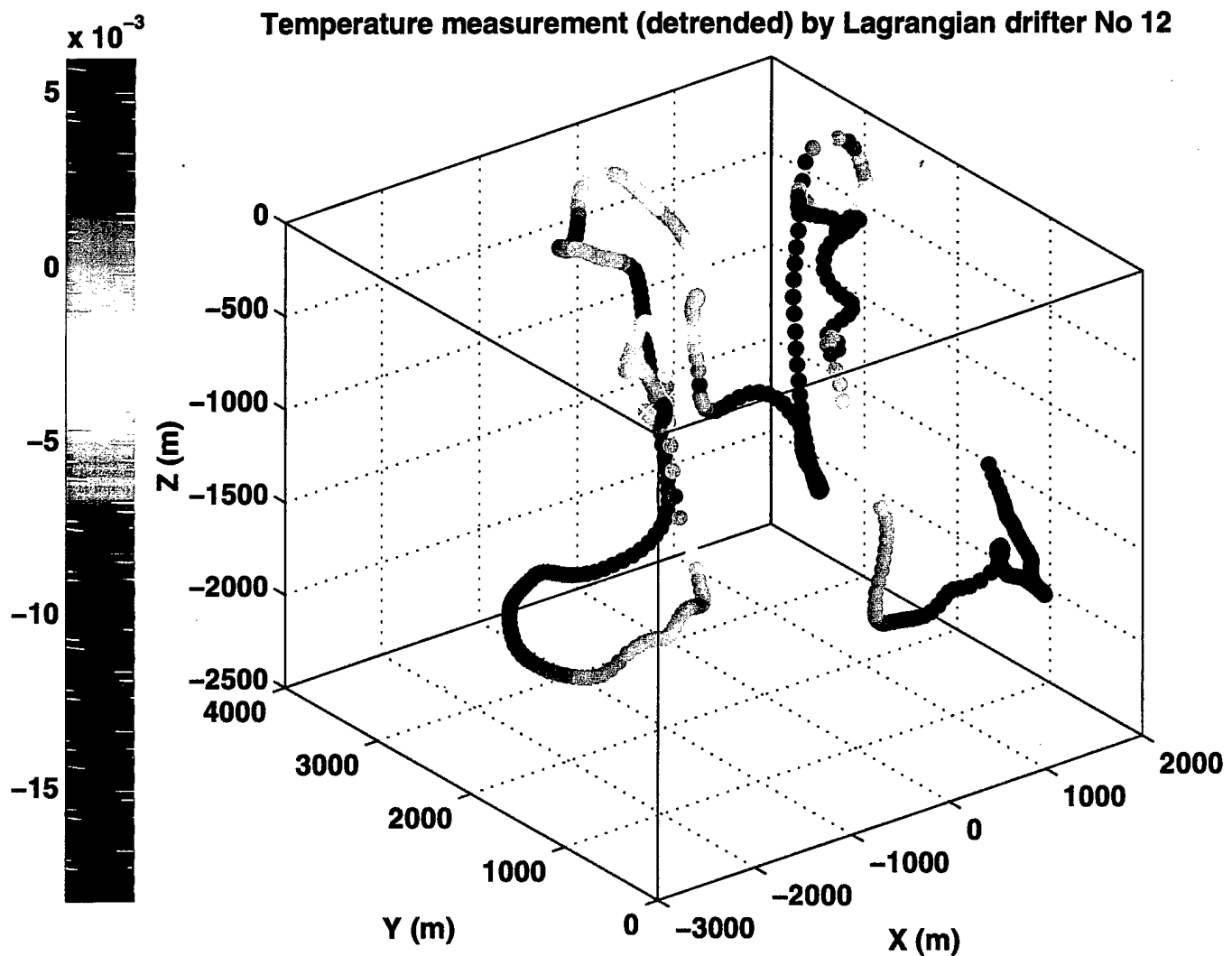
(b) Drifter #12

Figure 14. The 3-D perspective view of the locations of Drifters (a) #1, (b) #12, (c) #53, and (d) #154 and the temperature (*T*) observed by these drifters at that location, for the case with 400 W/m² heat loss and 1 m/s wind.

(c) Drifter #53

Figure 14. The 3-D perspective view of the locations of Drifters (a) #1, (b) #12, (c) #53, and (d) #154 and the temperature (T) observed by these drifters at that location, for the case with 400 W/m^2 heat loss and 1 m/s wind.
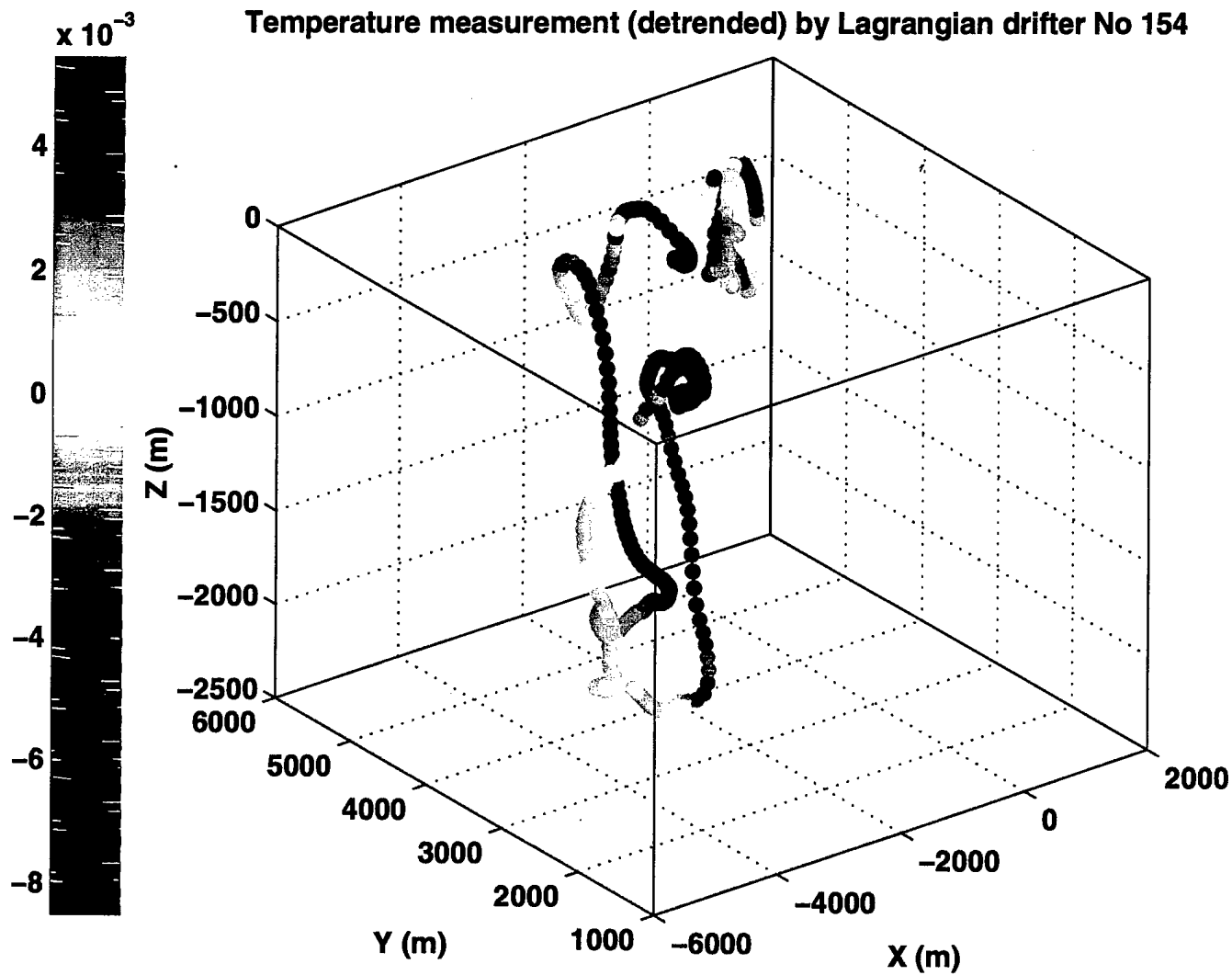
(d) Drifter #154

Figure 14. The 3-D perspective view of the locations of Drifters (a) #1, (b) #12, (c) #53, and (d) #154 and the temperature (T) observed by these drifters at that location, for the case with 400 W/m^2 heat loss and 1 m/s wind.
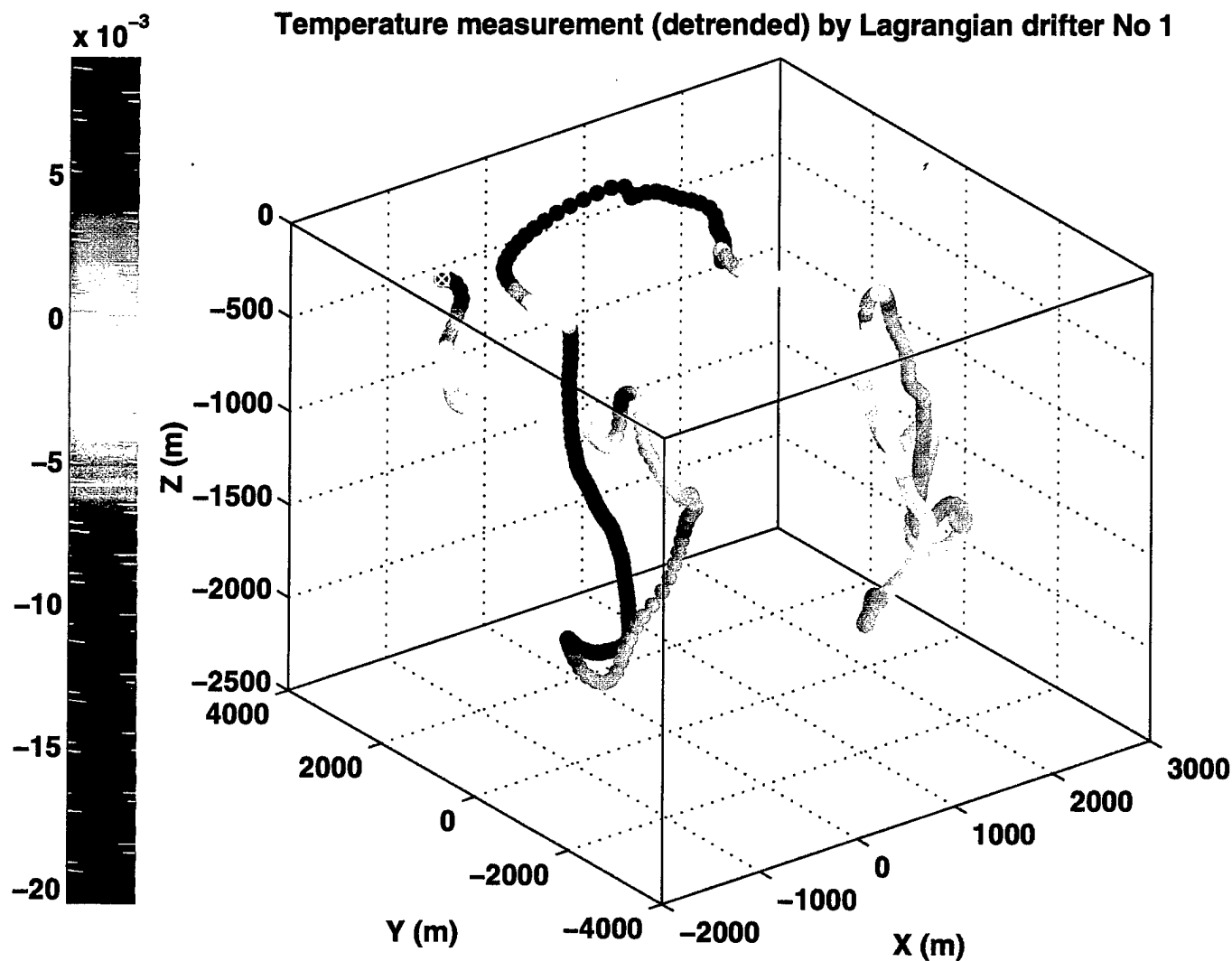
(a) Drifter #1

Figure 15. The 3-D perspective view of the locations of Drifters (a) #1 and (b) #40 and the temperature (T) observed by these drifters at that location, for the case with 400 W/m^2 heat loss and 20 m/s wind.
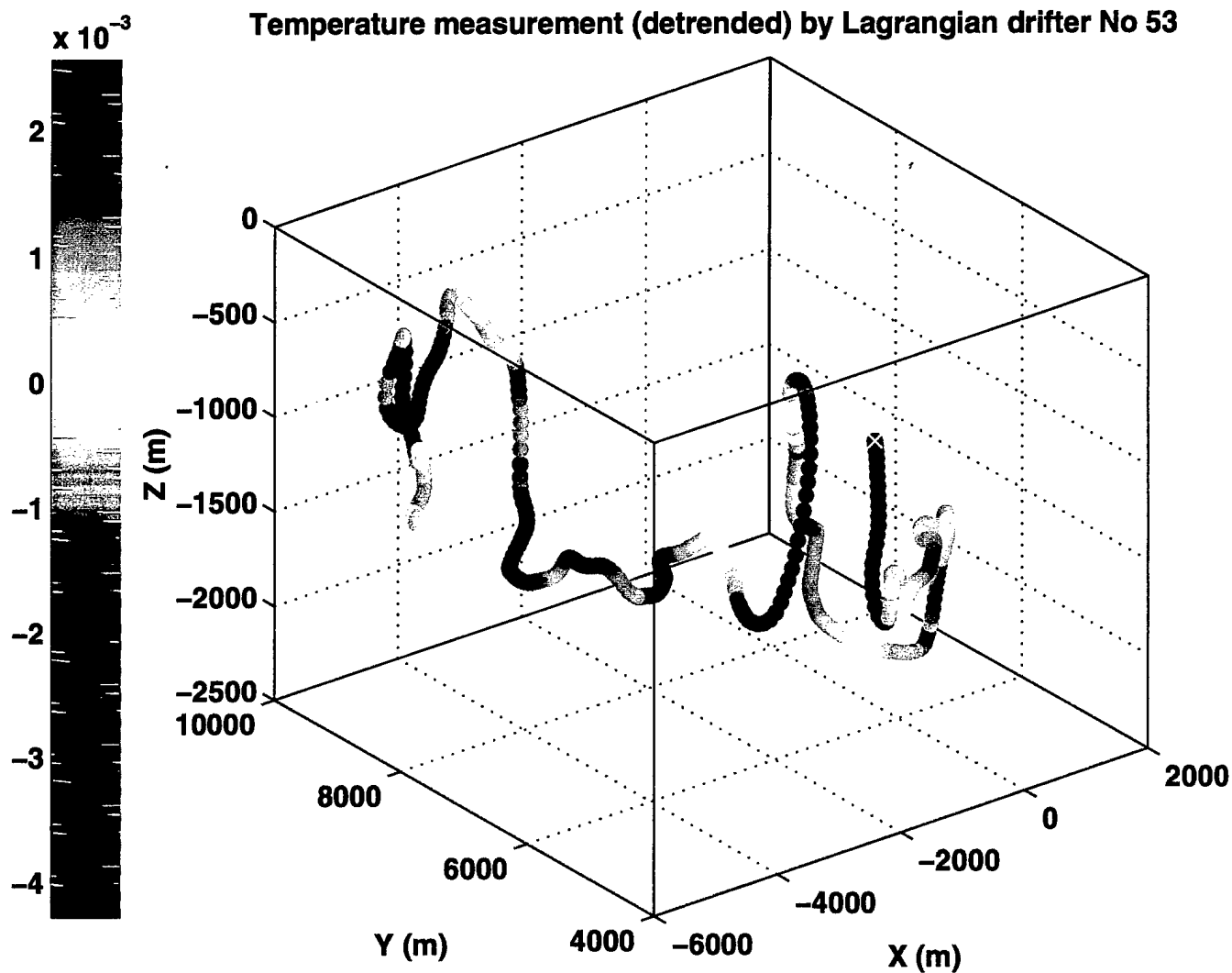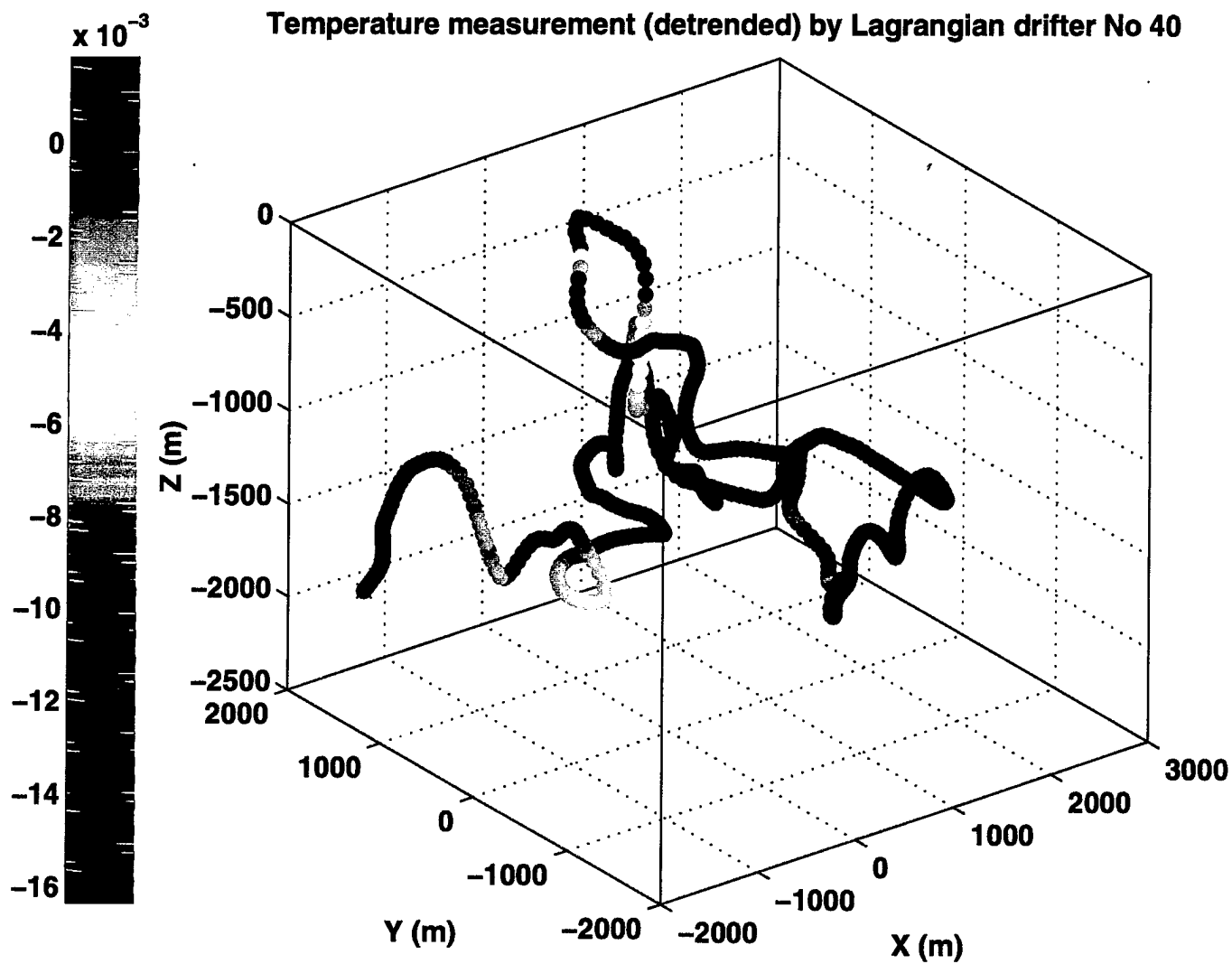
(b) Drifter #40

Figure 15. The 3-D perspective view of the locations of Drifters (a) #1 and (b) #40 and the temperature (T) observed by these drifters at that location, for the case with 400 W/m^2 heat loss and 20 m/s wind..

3.1.2. The Heat Flux

Figure 16 shows the measurement of the heat flux $\overline{w'T'}$ by the Lagrangian drifters in the three cases with 1m/s, 10 m/s, and 20 m/s wind, together with the long-term average of the Eulerian measurements. Compared with the Eulerian measurements we can see that the Lagrangian drifters detect all of the turbulent heat flux in the turbulent mixing layer.
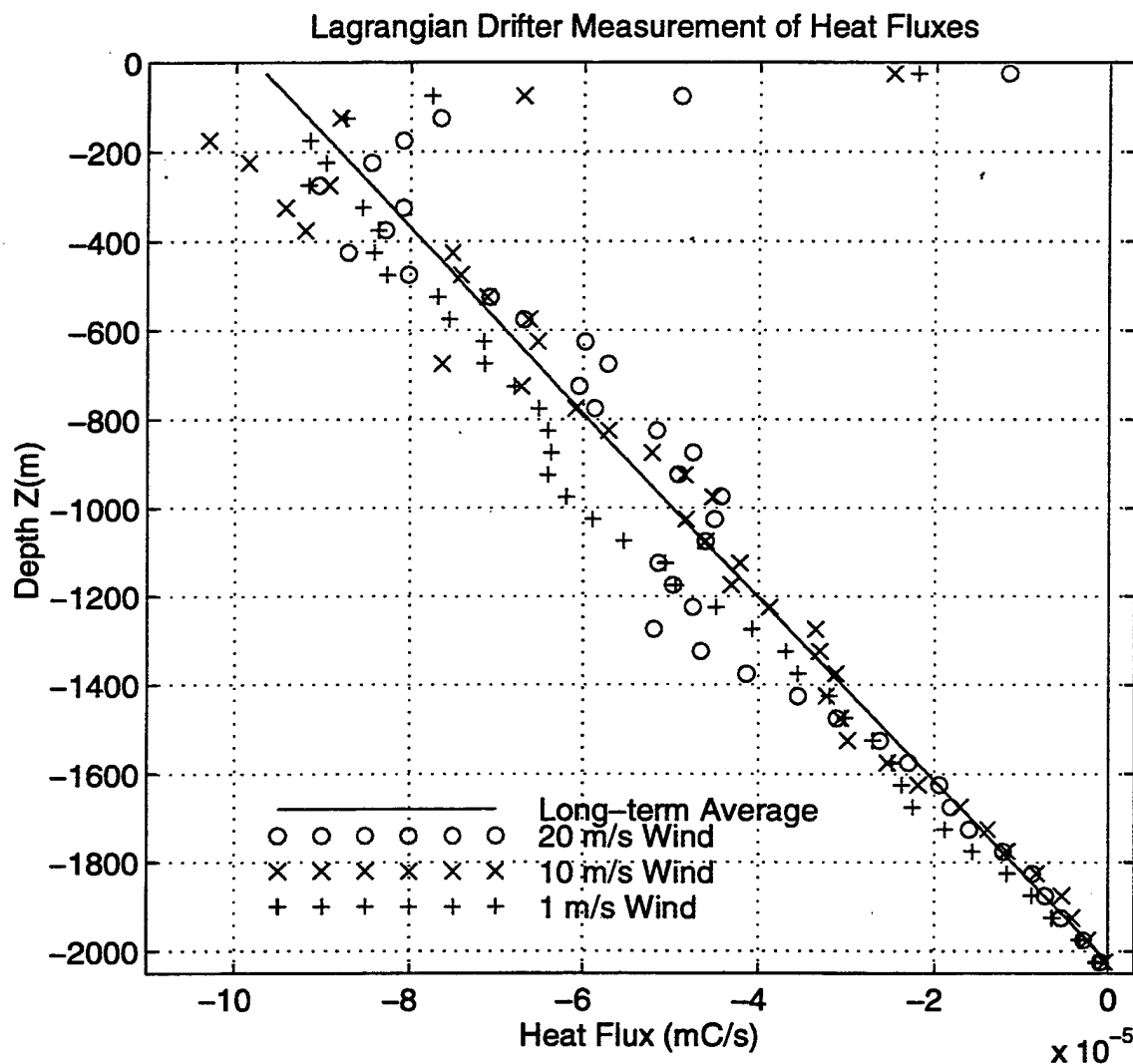
Figure 16. The measurement of the heat flux by the Lagrangian drifters for all the three cases with 1 m/s, 10 m/s, and 20 m/s wind forcing.

40

3.1.3. The Turbulent Kinetic Energy

The distributions of the total turbulent kinetic energy $\overline{(u'^2+v'^2+w'^2)}$ observed by the Lagrangian drifters for the 1 m/s, 10 m/s, and 20 m/s wind cases are illustrated in Figures 17 (a), (b), and (c), respectively. The solid line represents the total TKE; the dashed line represents the vertical component of TKE, $\overline{w'^2}$, and the dotted line and the dot-dash line represent the horizontal components of the TKE, $\overline{u'^2}$ and $\overline{v'^2}$. For all the cases the vertical TKE measured is very small near the surface, because the vertical TKE produced by the buoyancy flux is transported to depth, and it is also converted to horizontal TKE $\overline{(u'^2+v'^2)}$ by pressure constraints near the nonslip bottom. A maximum vertical TKE is detected by these drifters near mid-depth (400-600 meters), with a peak root-mean-square vertical velocity of about 3 - 4 cm/s. This agrees well with the Eulerian measurements. The drifters sensed the surface horizontal turbulent kinetic energy peak which is a result of the diverging and converging transport associated with the sinking plumes and upward motion of returning warmer water. The drifters also detected a peak in the horizontal kinetic energy near the bottom which is a result of the divergence induced by the descending plumes. Wind-induced shear production that increases the horizontal TKE near the surface and near the bottom is captured by the Lagrangian drifters. Strong wind forcing (Figure 17(c)) generates the largest horizontal TKE at the surface and near the bottom, and also generates the largest vertical TKE at 400-600 meters, as sensed by the drifters. More TKE is produced by the buoyancy flux, and the TKE dissipates with depth. Near the surface $\overline{w'^2}$ is very strongly converted into $\overline{(u'^2+v'^2)}$ and advected to depth. The total TKE is not proportional to the buoyancy flux because of the advection and conversion of $\overline{w'^2}$ produced near the surface. This tendency is verified by the following TKE transport analysis.

Figure 18 (a), (b), and (c) show the vertical distribution of the transport of TKE $\overline{w'(u'^2+v'^2+w'^2)}$ measured by the Lagrangian drifters for the three cases respectively. The solid line represents the total TKE transport; the dashed line represents the vertical component of TKE transport $\overline{w'^3}$, and the dotted line and the dot-dash line represent the

41

horizontal components of the TKE transport $\overline{wu'^2}$ and $\overline{wv'^2}$. The vertical transport component $\overline{w'^3}$ due to the vertical velocity has a negative value at the surface as a result of the downward penetrating plumes that carrying TKE downward. The $\overline{w'^3}$ term has a maximum about 500-700 meters above the bottom. This is because of the most energetic large plumes, and it has a minimum value at the bottom. This is the result of the rising returning warmer water that carries the TKE upward. At the bottom w is zero and the $\overline{w'^3}$ term is zero. Note that there is an upward transport of TKE in the upper 300 meters. Near the surface a very large amount of $\overline{w'^2}$ has been converted to $\overline{(u'^2+v'^2)}$, so the large recirculating plumes actually carried TKE upward in the upper 300 meters.

3.1.4. The Temperature Variance

The maximum temperature variance $\overline{T'^2}$ observed by the Lagrangian drifters (as shown in Figure 19 is 1.2×10^{-4} CC near the surface. The solid lines are long-term mean of the Eulerian measurements and the symbols represent the Lagrangian data. The temperature variance decreases drastically with depth. The Lagrangian drifter sampled accurately the temperature variance, compared with the temperature variance by the Eulerian measurements except at the surface in the 20 m/s case.

TKE Measurement by Lagrangian Drifters

(a) 1 m/s wind

Figure 17. The distributions of the total turbulent kinetic energy $\overline{(u'^2+v'^2+w'^2)}$ observed by the Lagrangian drifters for cases (a) 1 m/s wind, (b) 10 m/s wind, and (c) 20 m/s wind. The solid line represents the total TKE; the dashed line represents the vertical component of TKE $\overline{w'^2}$, and the dotted line and the dot-dash line represent the horizontal components of the TKE $\overline{u'^2}$ and $\overline{v'^2}$.

43

TKE Measurement by Lagrangian Drifters

(b) 10 m/s wind

Figure 17. The distributions of the total turbulent kinetic energy $\overline{(u'^2+v'^2+w'^2)}$ observed by the Lagrangian drifters for cases (a) 1 m/s wind, (b) 10 m/s wind, and (c) 20 m/s wind. The solid line represents the total TKE; the dashed line represents the vertical component of TKE $\overline{w'^2}$, and the dotted line and the dot-dash line represent the horizontal components of the TKE $\overline{u'^2}$ and $\overline{v'^2}$.

44

(c) 20 m/s wind
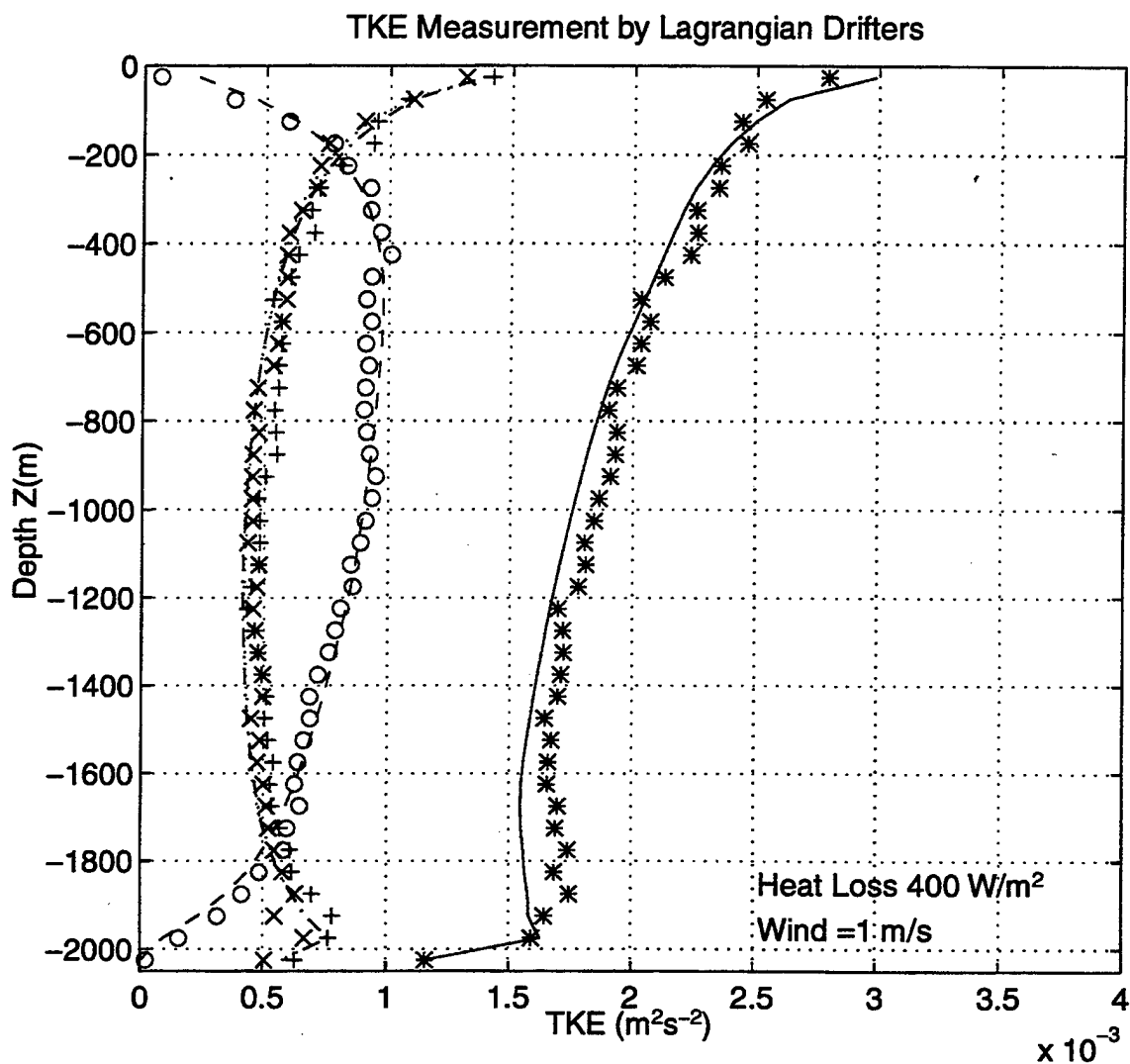
Figure 17. The distributions of the total turbulent kinetic energy $\overline{(u'^2+v'^2+w'^2)}$ observed by the Lagrangian drifters for cases (a) 1 m/s wind, (b) 10 m/s wind, and (c) 20 m/s wind. The solid line represents the total TKE; the dashed line represents the vertical component of TKE $\overline{w'^2}$, and the dotted line and the dot-dash line represent the horizontal components of the TKE $\overline{u'^2}$ and $\overline{v'^2}$.

45

(a) 1 m/s wind

Figure 18. The vertical distribution of the transport of TKE $\overline{w'(u'^2+v'^2+w'^2)}$ measured by the Lagrangian drifters for cases (a) 1 m/s wind, (b) 10 m/s wind, and (c) 20 m/s wind. The solid line represents the total TKE transport; the dashed line represents the vertical component of TKE transport $\overline{w'^3}$, and the dotted line and the dot-dash line represent the horizontal components of the TKE transport $\overline{wu'^2}$ and $\overline{wv'^2}$.

46

TKE Transport Measurement by Lagrangian Drifters

(b) 10 m/s wind

Figure 18. The vertical distribution of the transport of TKE $\overline{w'(u'^2+v'^2+w'^2)}$ measured by the Lagrangian drifters for cases (a) 1 m/s wind, (b) 10 m/s wind, and (c) 20 m/s wind. The solid line represents the total TKE transport; the dashed line represents the vertical component of TKE transport $\overline{w'^3}$, and the dotted line and the dot-dash line represent the horizontal components of the TKE transport $\overline{wu'^2}$ and $\overline{wv'^2}$.
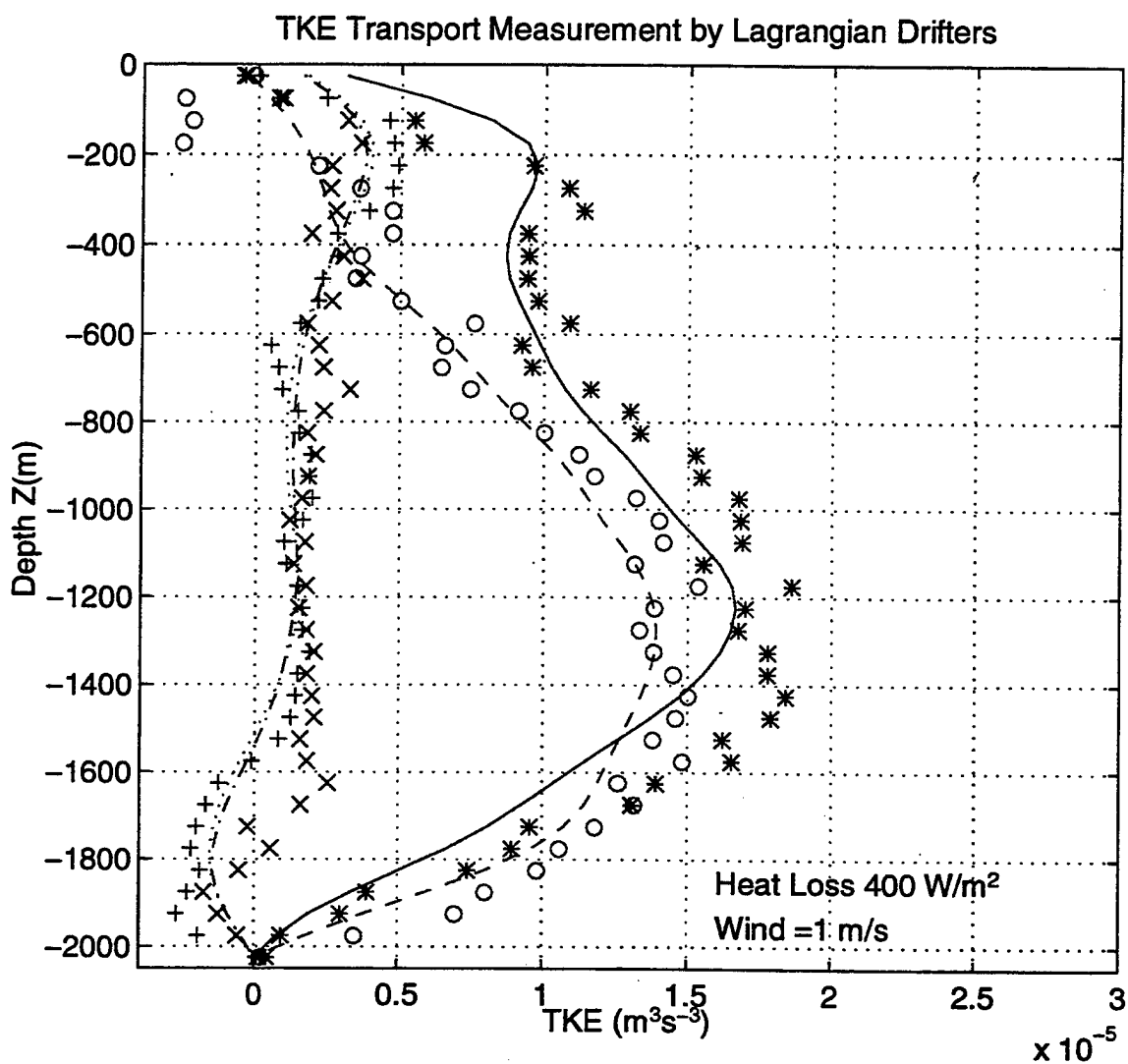
47

TKE Transport Measurement by Lagrangian Drifters

(c) 20 m/s wind

Figure 18. The vertical distribution of the transport of TKE $\overline{w'(u'^2+v'^2+w'^2)}$ measured by the Lagrangian drifters for cases (a) 1 m/s wind, (b) 10 m/s wind, and (c) 20 m/s wind. The solid line represents the total TKE transport; the dashed line represents the vertical component of TKE transport $\overline{w'^3}$, and the dotted line and the dot-dash line represent the horizontal components of the TKE transport $\overline{wu'^2}$ and $\overline{wv'^2}$.
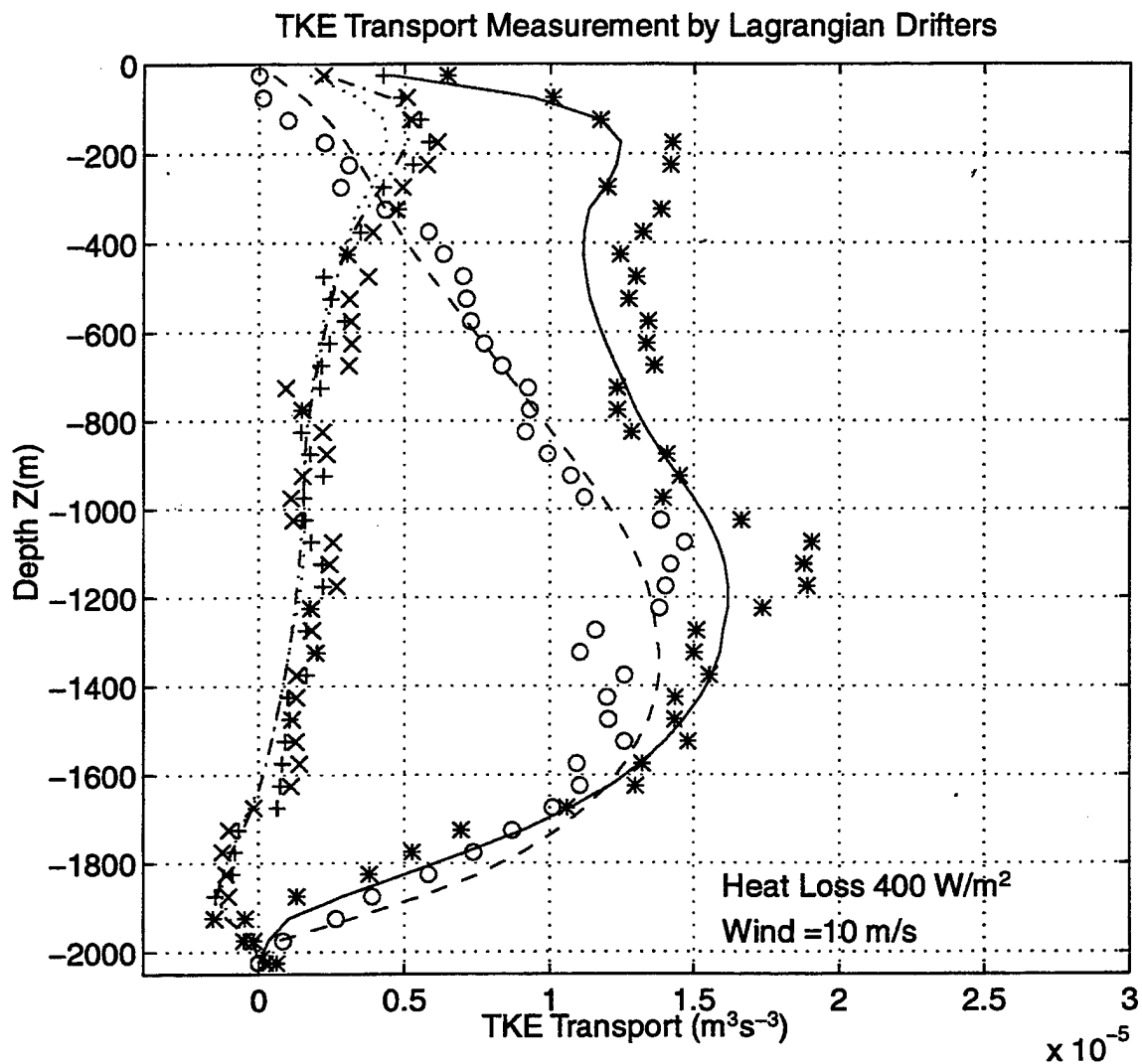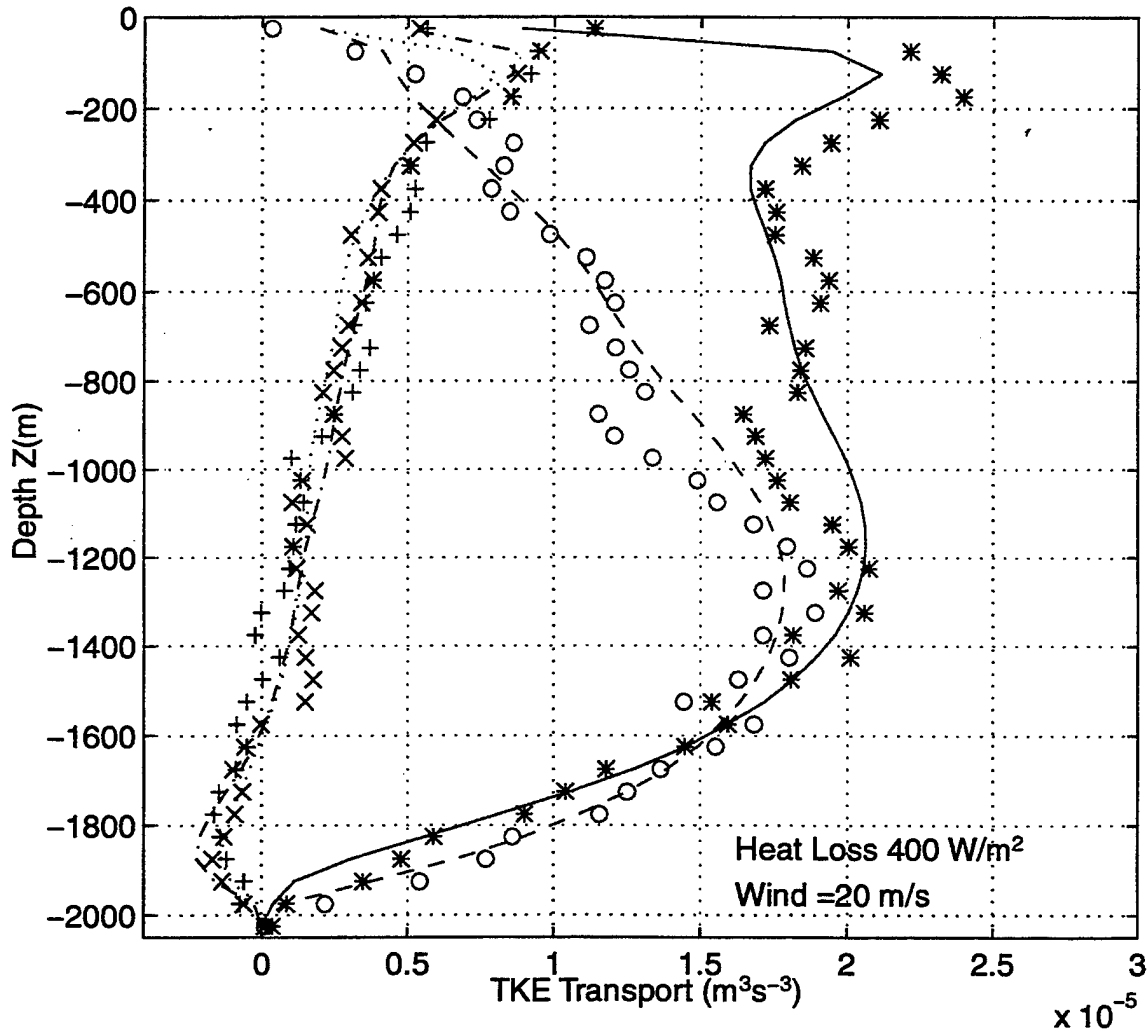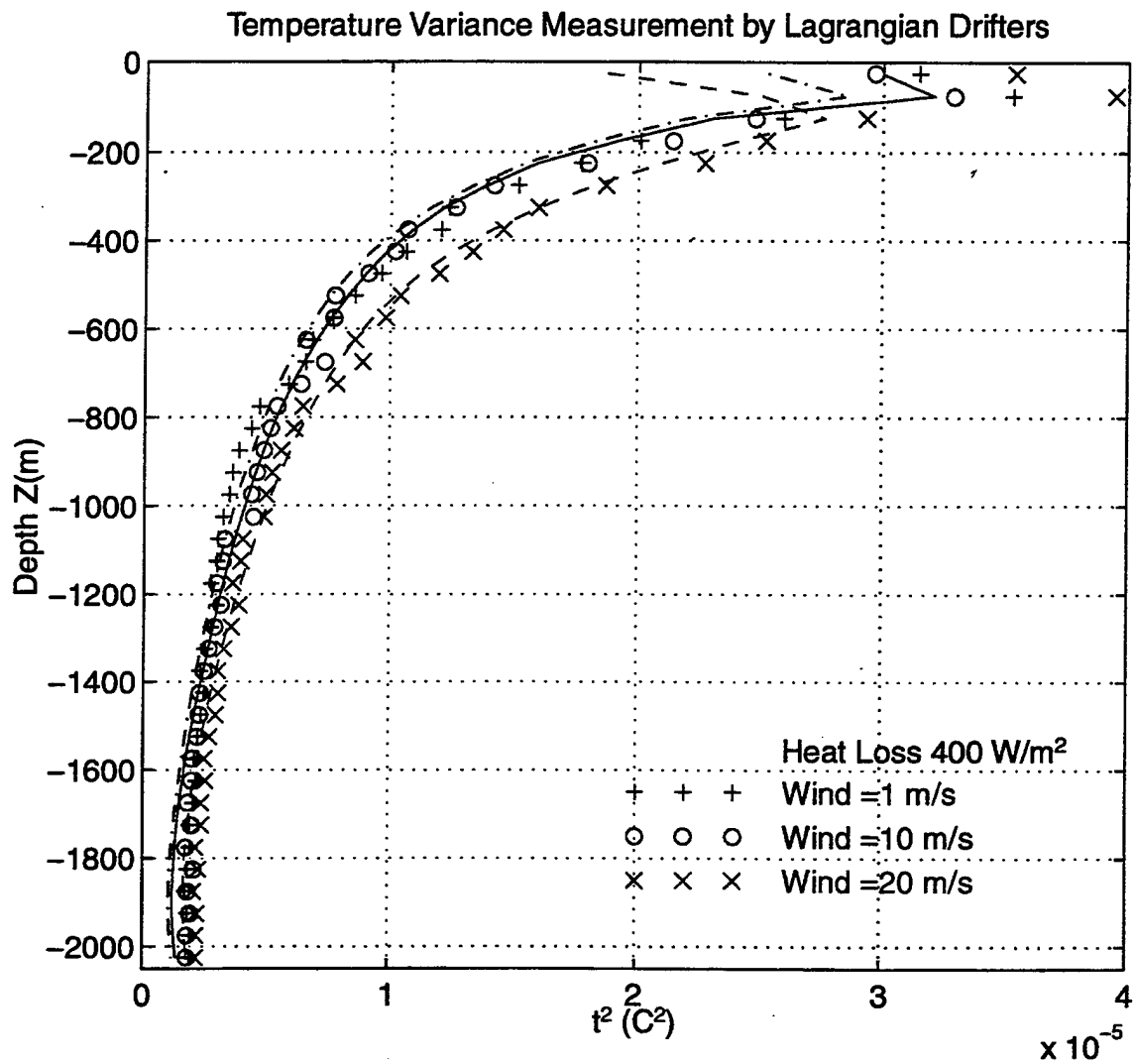
48

Figure 19. The vertical distribution of the temperature variance $\overline{T^2}$ observed by the Lagrangian drifters for the cases with 400 W/m² heat loss and 1 m/s, 10 m/s and 20 m/s wind.

3.2. ISOBARIC DRIFTERS

3.2.1. The Drifter Trajectories

Figure 20 shows the 3-D perspective view of the trajectories of the four surface drifters (# 1, #41, #81, and #121, in green), the four mid-depth drifters (#20, #60, #100, and #140, in red), and the four bottom drifters (#40, #80, #120, and #160, in blue) for the case with 400 W/m^2 heat loss and 1 m/s wind forcing. The trajectories show the motion of the isobaric drifters on horizontal planes. More details of the trajectories of individual drifters are discussed as follows.

Figure 21(a, b) shows the plan view of the trajectories of one surface drifter ((a) #1) and one bottom drifter ((b) #120) for the free convection case, together with the velocity vectors plotted along the trajectories every 200 time steps. The drifters start at the ends with circles. The velocity vectors give a clear indication of the direction of the rotation of these drifters. It is seen that the isobaric drifters are caught in cyclonic rotation induced by the converging plumes. The size of the loops give the approximate scale of these sinking plumes, which is in the range of 250-500 meters. The examination of the temperature measurements by the drifters confirm that the drifters are indeed arrested in the plumes for some time during the course of drifting.

Figure 22 (a, b) shows the plan view of the trajectories of one surface drifter ((a) #1) and one bottom drifter ((b) #40) for the forced convection case (with 20 m/s wind), together with the velocity vectors plotted along the trajectories every 200 time steps. The drifters start at the circles. In the presence of upward surface buoyancy flux, increased wind stress disrupts the Rayleigh-Benard cells. The elongation of the cells to the right of the wind direction is evident in the surface drifter trajectory (Figure 22(a)).

50
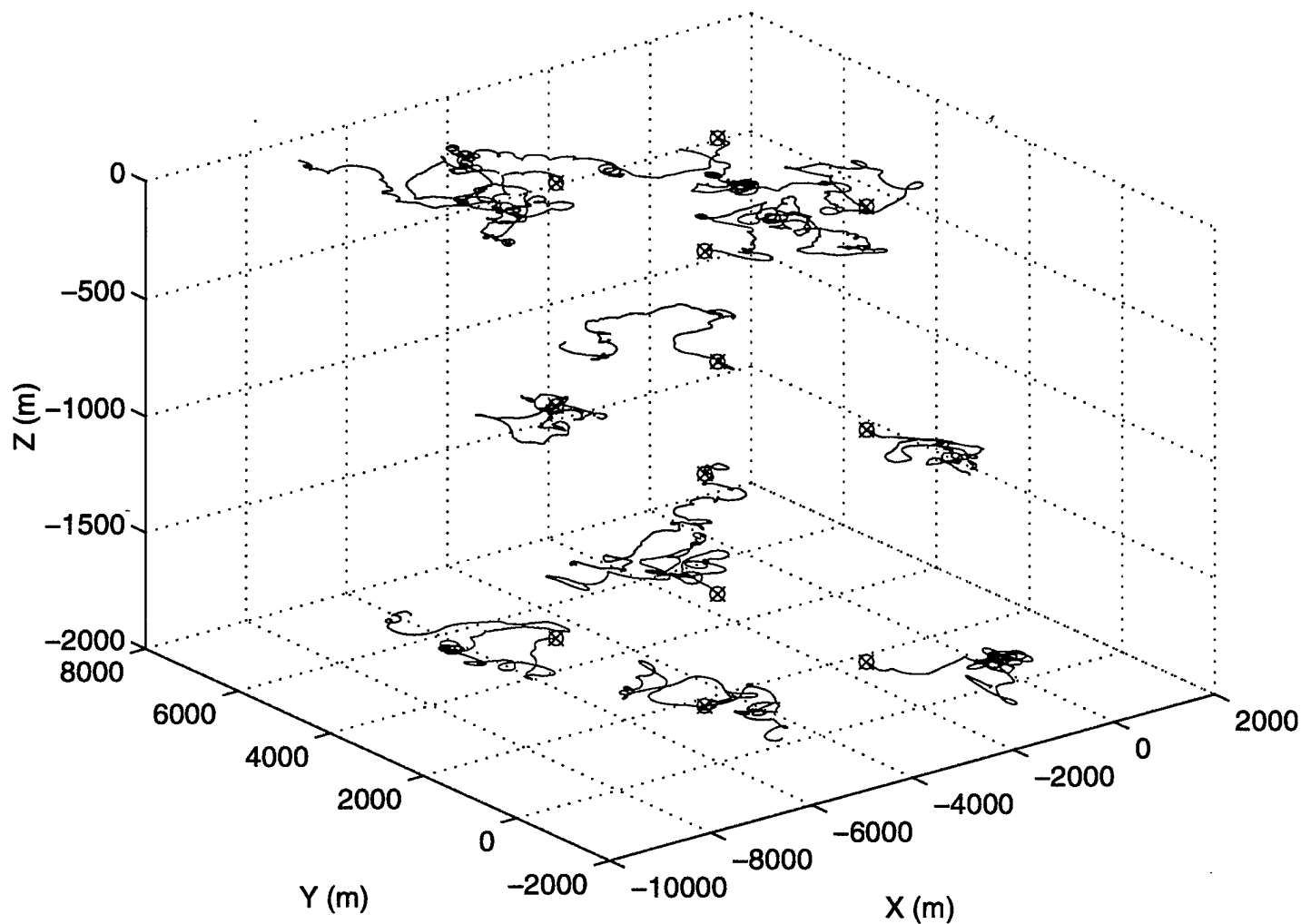
Figure 20. The 3-D perspective view of the trajectories of the four surface isobaric drifters (# 1, #41, #81, and #121, in green), the four mid-depth drifters (#20, #60, #100, and #140, in red), and the four bottom drifters (#40, #80, #120, and #160, in blue) for the free convection case.
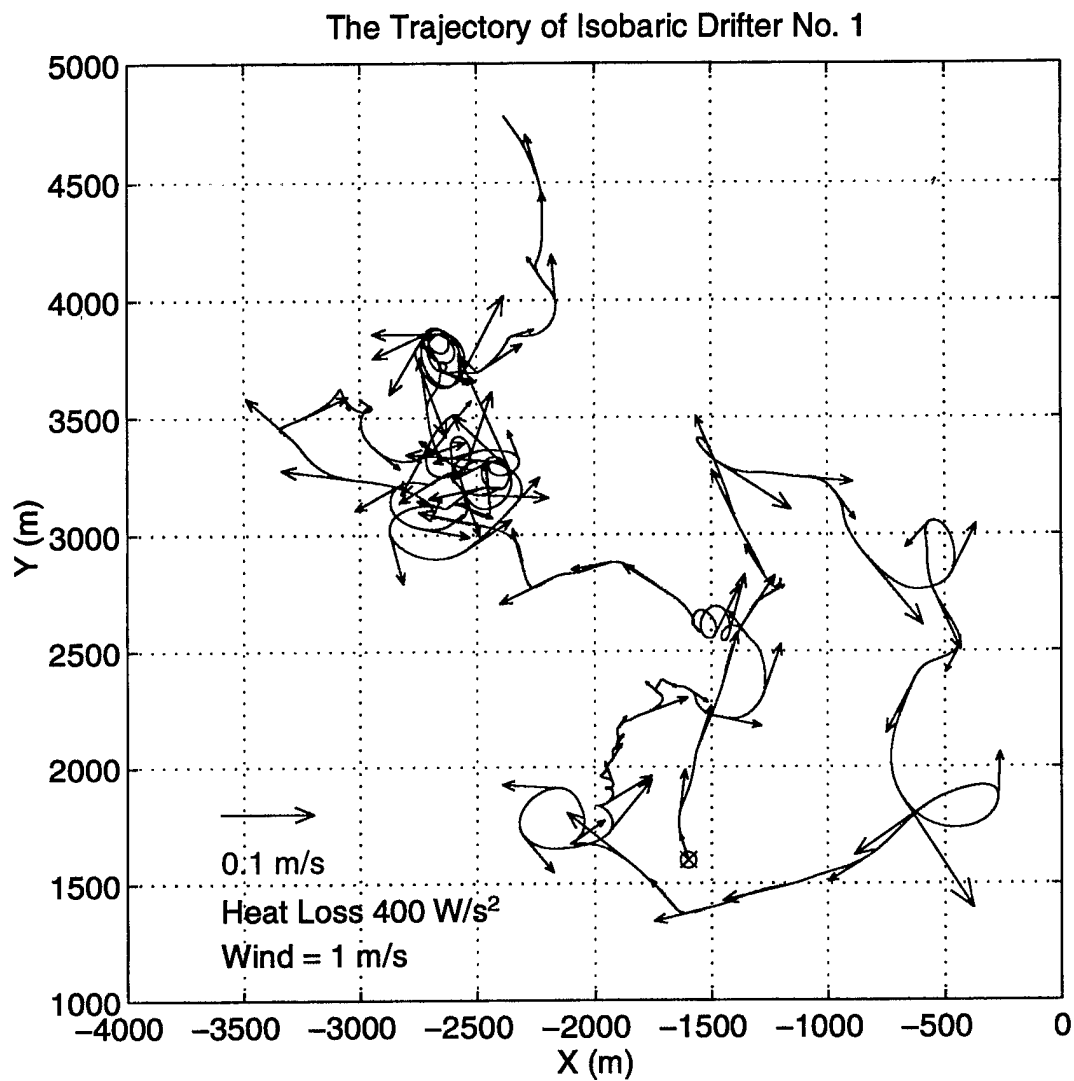
(a) Drifter #1

Figure 21. The plan view of the trajectories of one surface isobaric drifter: (a) #1, and one bottom drifter: (b) #120 for the free convection case, together with the horizontal velocity vectors plotted along the trajectories every 200 time steps.

The Trajectory of Isobaric Drifter No. 120
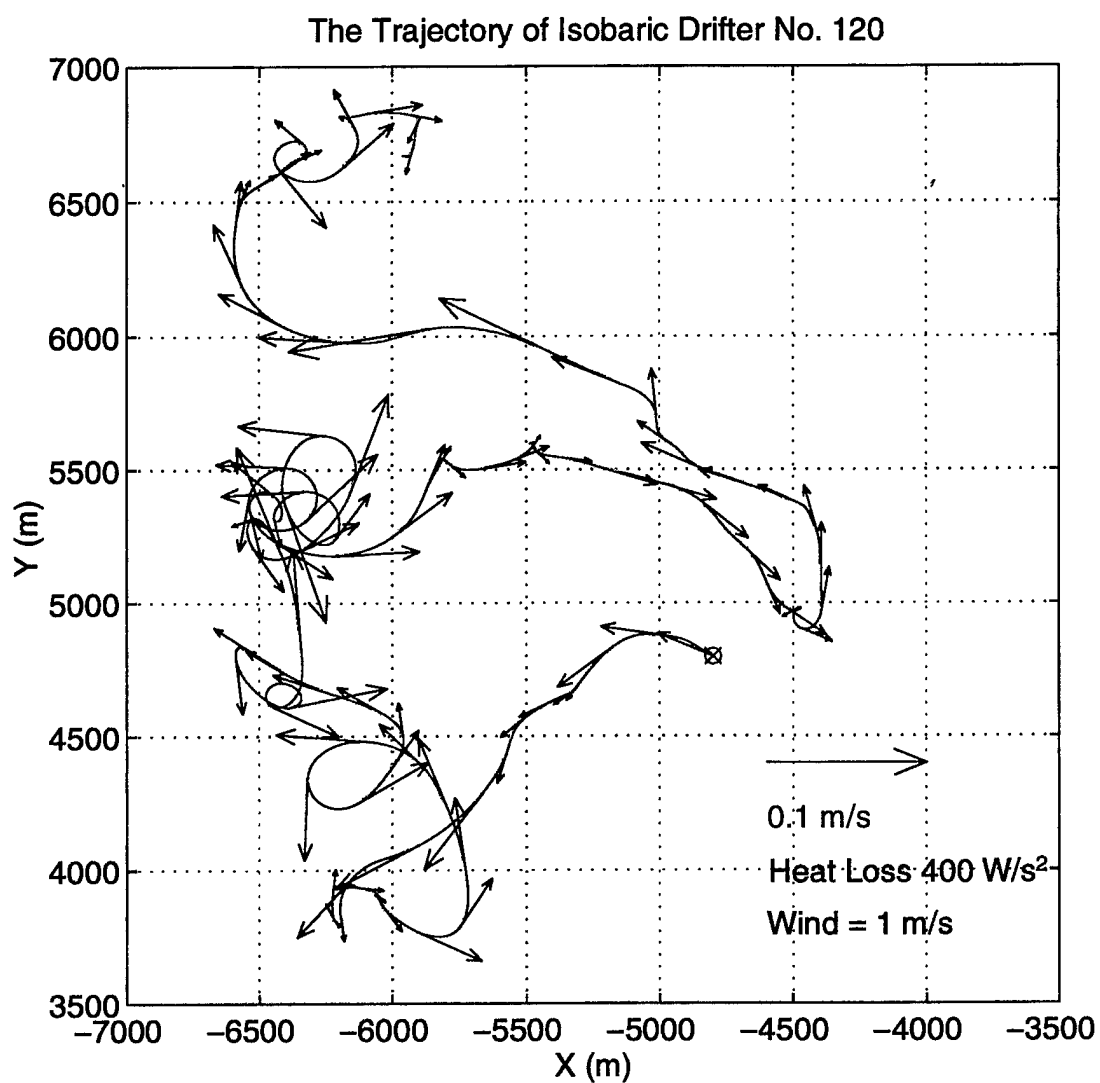
(b) Drifter #120

Figure 21. The plan view of the trajectories of one surface isobaric drifter: (a) #1, and one bottom drifter: (b) #120 for the free convection case, together with the horizontal velocity vectors plotted along the trajectories every 200 time steps.

The Trajectory of Isobaric Drifter No. 2

(a) Drifter #2

Figure 22. The plan view of the trajectories of one surface isobaric drifter: (a) #2, and one bottom drifter: (b) #40 for the forced convection case (with 20 m/s wind), together with the horizontal velocity vectors plotted along the trajectories every 200 time steps.

The Trajectory of Isobaric Drifter No. 40

(b) Drifter #40

Figure 22. The plan view of the trajectories of one surface isobaric drifter: (a) #2, and one bottom drifter: (b) #40 for the forced convection case (with 20 m/s wind), together with the horizontal velocity vectors plotted along the trajectories every 200 time steps.
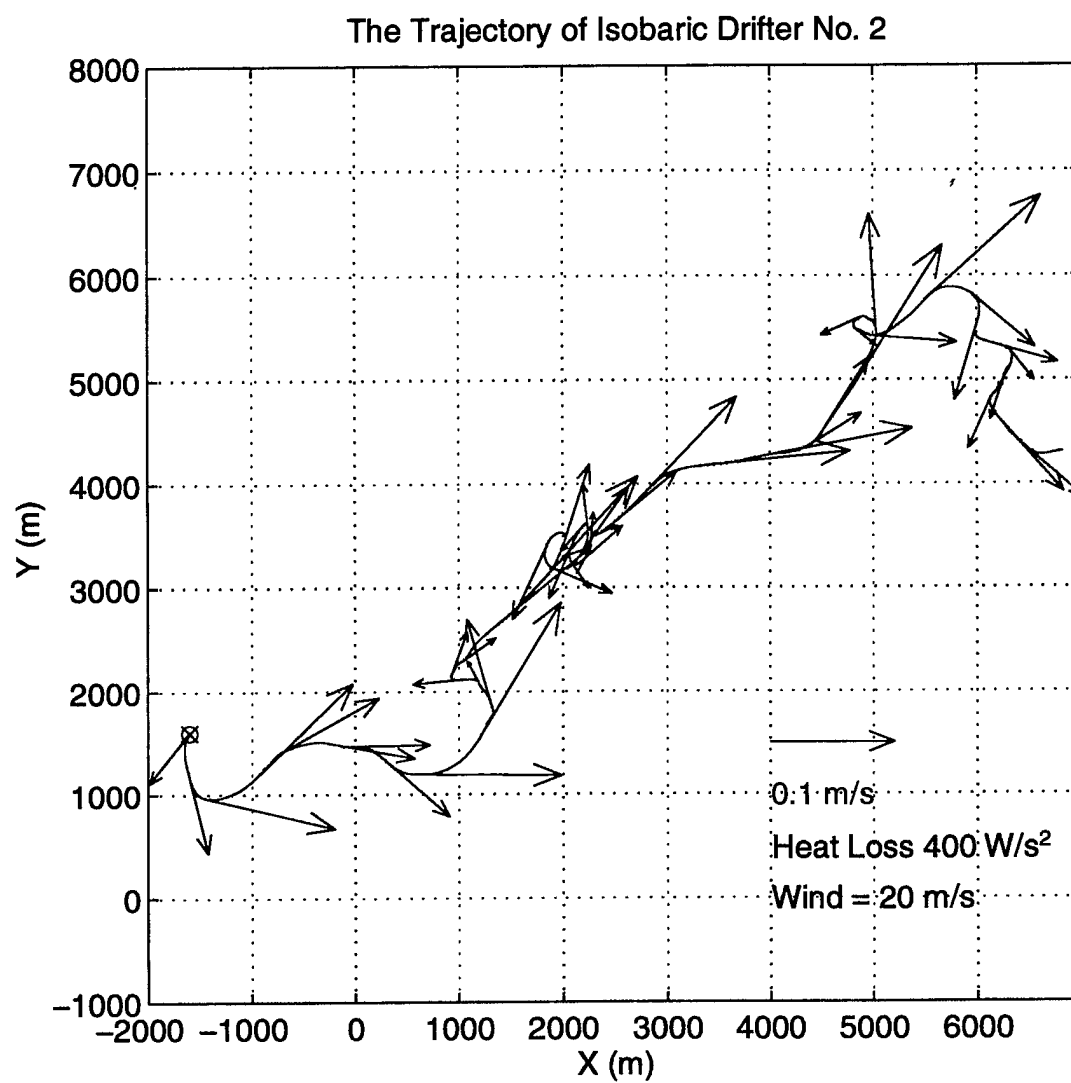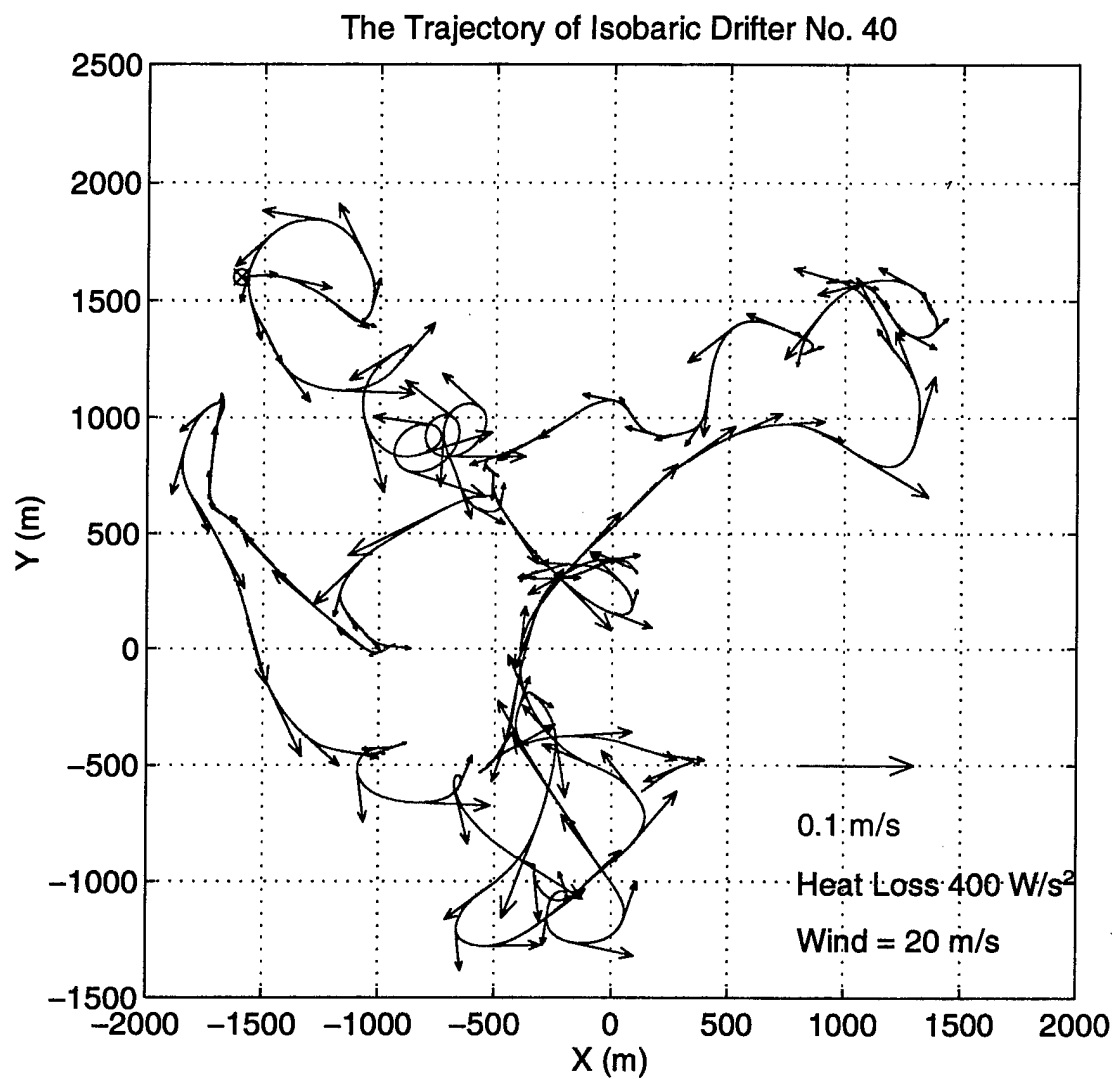
3.2.2. The Vertical Velocity

Figure 23 shows the vertical distribution of the mean vertical velocity ($\overline{w}$) measurements by the isobaric drifters for all the three cases with 1 m/s, 10 m/s, and 20 m/s wind. The mean vertical velocity is positive (note that positive Z axis in downward in the LES model simulation, so w > 0 is downward here) near the surface where there is a net downward TKE transport. The mean vertical velocity measured by the isobaric drifters is negative in the lower 1000 meters, which is a net rising transport region. The maximum downward vertical velocity is about 2 cm/s near the surface in the sinking water. The maximum upward vertical velocity is about 1 cm/s near the bottom in the returning water. Because the isobaric drifters spend more time in convergence zones, they measure a nonzero mean vertical velocity. This results in an apparent upwelling in the lower 2/3 of the mixing layer and a mean downwelling in the upper 1/3 of the mixing layer, approximately. The isobaric drifters are able to measure maximum-likely vertical velocity. The isobaric drifters are particularly useful for tracking the convective activity because they seek out convergence zones that rapidly respond to convection.

3.2.3. The Heat Flux

Figure 24 shows the measurement of the heat flux $\overline{w'T'}$ by the isobaric drifters for all the three cases with 1 m/s, 10 m/s, and 20 m/s wind. Compared with the long-term mean Eulerian measurement we can see that the isobaric drifters give a biased measurement of the heat flux. The heat flux term has a maximum near the surface and also decreases almost linearly to zero at the bottom. The maximum heat flux is only half of the actual heat flux. The reason is that the isobaric drifters seek out the sinking cold water and get trapped in the sinking plumes, thus they cannot get the unbiased statistical information of heat flux. This is confirmed again by the temperature variance measured by the isobaric drifters, which is only half of that of the Eulerian measurements.

5 6

3.2.4. Turbulent Kinetic Energy

The distributions of the vertical component of the TKE observed by the isobaric drifters for the cases with 400 W/m^2 heat loss and 1 m/s, 10 m/s, and 20 m/s wind are shown in Figure 25 (a, b, c). The vertical TKE $\overline{w'^2}$ measured by the isobaric drifters is similar to that measured by the Lagrangian drifters. It is small near surface and near bottom. It has a maximum value in depth ranging from 300 - 1000 meters. The vertical TKE component $\overline{w'^2}$ has a similar distribution with the Eulerian measurements, but it is (20-30)% smaller due to the biased measurement of the vertical velocity.

Figure 26 shows the distribution of the vertical component of the TKE transport of $\overline{w'(u'^2+v'^2+w'^2)}$ sampled by the isobaric drifters for the cases with 400 W/m^2 heat loss and 1 m/s, 10 m/s, and 20 m/s wind. The vertical transport of TKE observed by the isobaric drifters is biased due to the same reason that the measurement of w is biased. The vertical component of the TKE transport $\overline{w'^3}$ has a negative value at the surface as a result of the downward penetrating plumes that carrying TKE downward. The $\overline{w'^3}$ term has a maximum about 300-500 meters above the bottom and has a minimum value at the bottom.
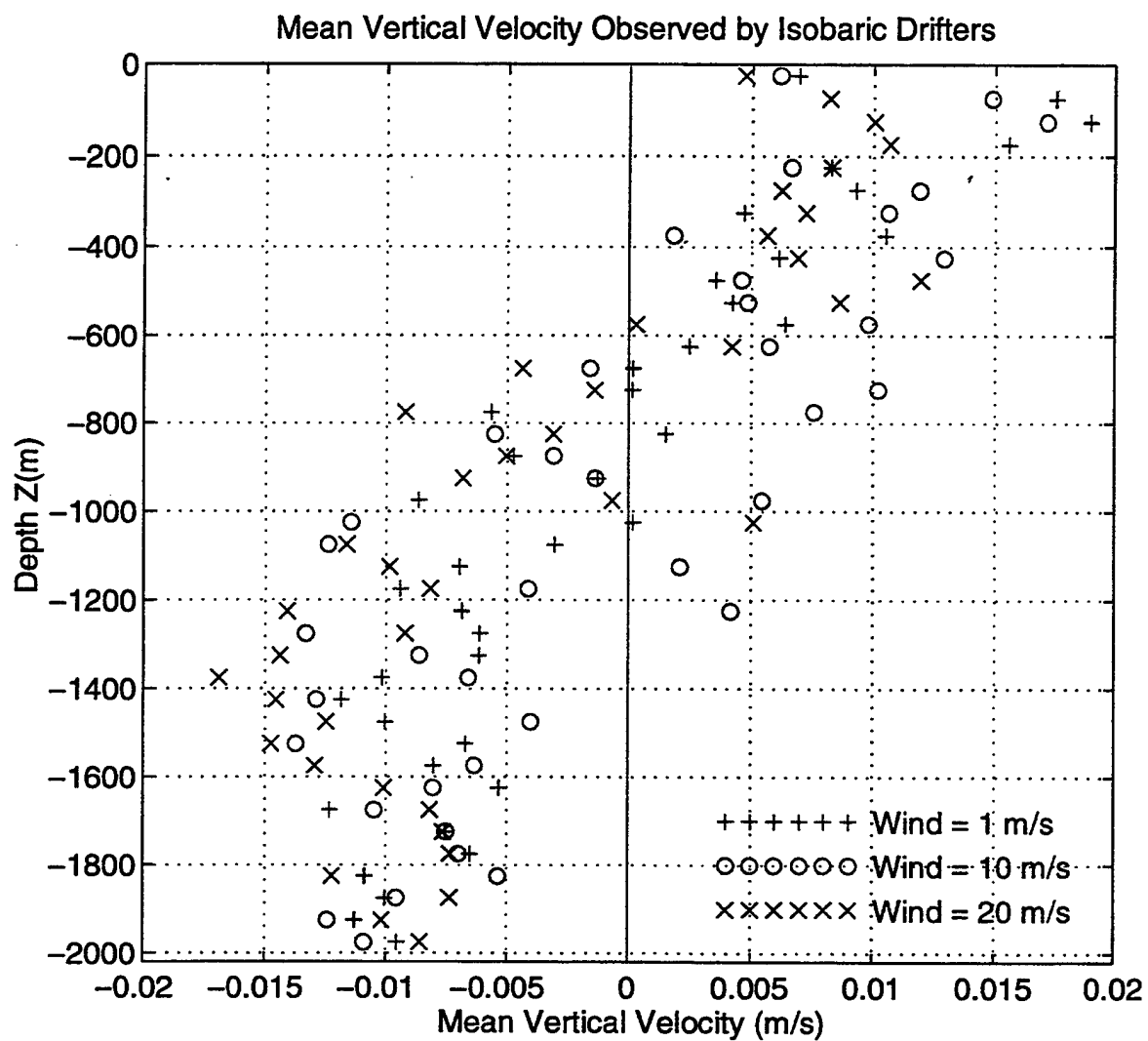
Figure 23. The mean vertical velocity measured by the isobaric drifters for all the three cases with 1 m/s, 10 m/s, and 20 m/s wind. Note: w > 0 is downward.
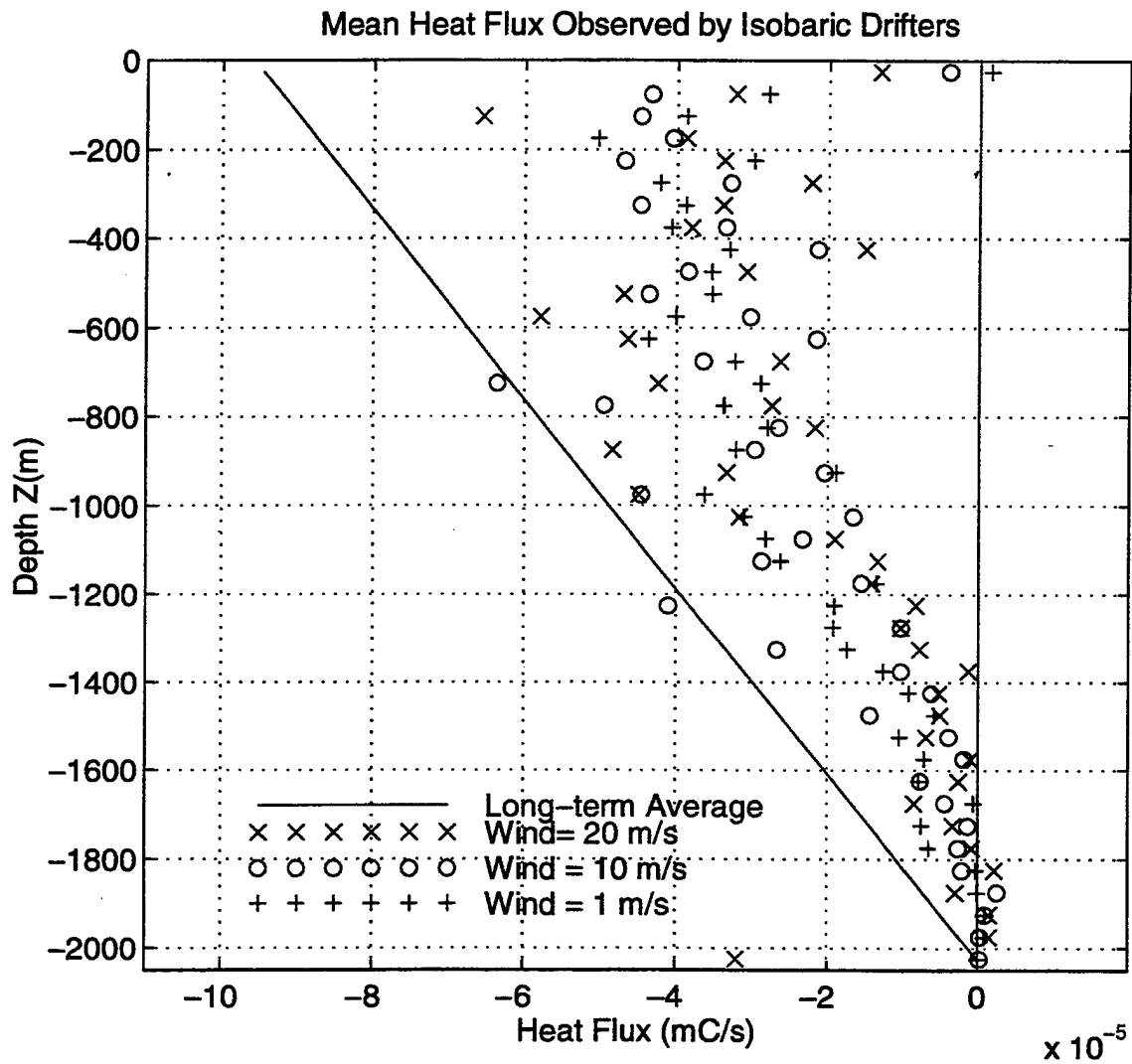
Figure 24. The heat flux measured by the isobaric drifters for all the three cases with 1 m/s, 10 m/s, and 20 m/s wind.
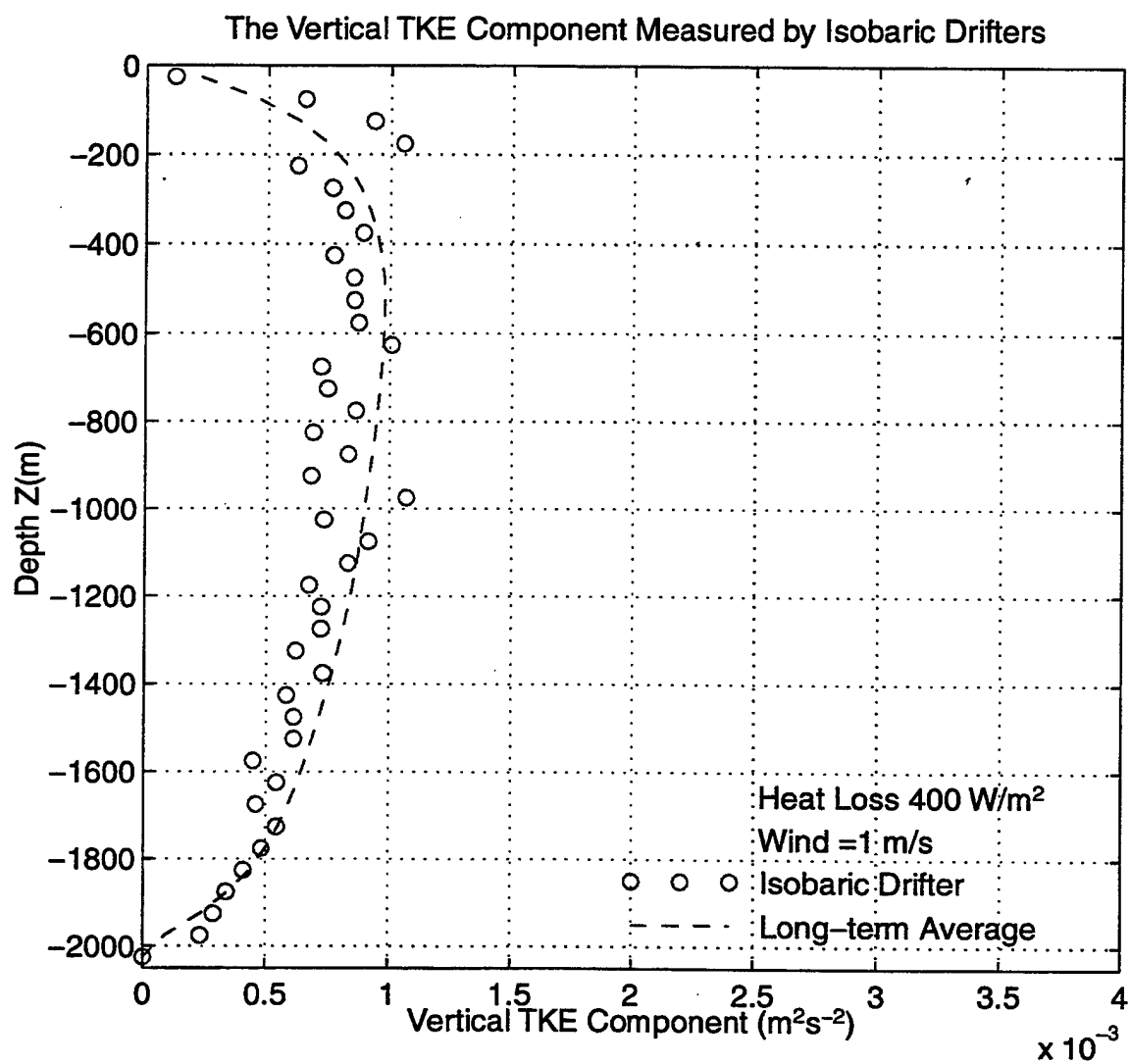
(a) 1 m/s wind

Figure 25. The distribution the vertical component of the TKE $\overline{w'^2}$ sampled by the isobaric drifters for all the three cases with (a) 1 m/s, (b) 10 m/s, and (c) 20 m/s wind.

60

The Vertical TKE Component Measured by Isobaric Drifters

Heat Loss 400 W/m²
Wind =10 m/s
O   O   O Isobaric Drifter
– – – – Long-term Average
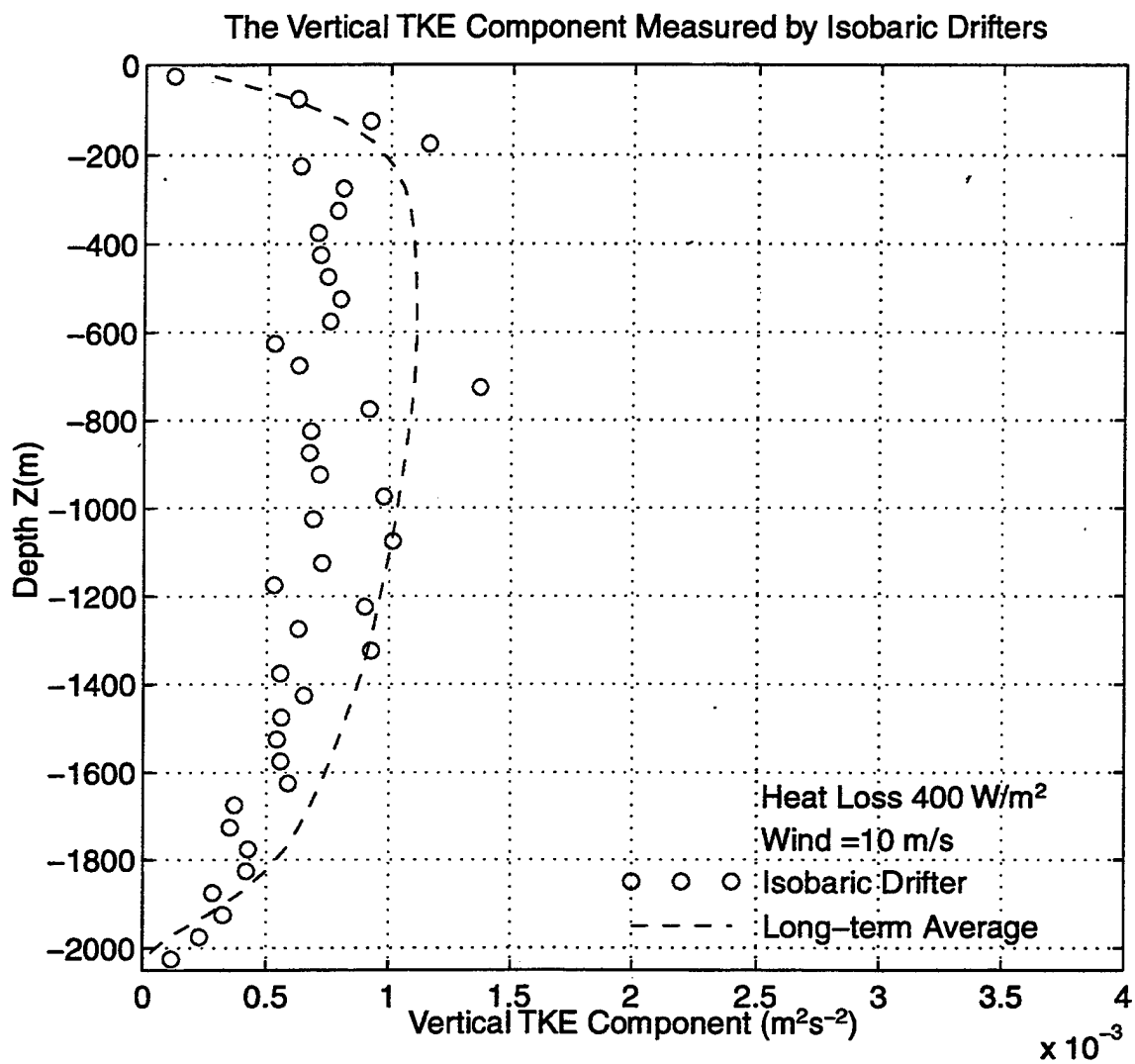
(b) 10 m/s wind

Figure 25. The distribution the vertical component of the TKE $\overline{w'^2}$ sampled by the isobaric drifters for all the three cases with (a) 1 m/s, (b) 10 m/s, and (c) 20 m/s wind.

(c) 20 m/s wind

Figure 25. The distribution the vertical component of the TKE $\overline{w'^2}$ sampled by the isobaric drifters for all the three cases with (a) 1 m/s, (b) 10 m/s, and (c) 20 m/s wind.

Figure 26. The distribution the vertical component of the TKE transport $\overline{w'^3}$ sampled by the isobaric drifters for all the three cases with (a) 1 m/s, (b) 10 m/s, and (c) 20 m/s wind. Note: $\overline{w'^3} > 0$ is downward transport.

3.2.5. Temperature Variance

The maximum temperature variance $\overline{T'^2}$ of 1.2×10^{-4} C^2 observed by the isobaric drifters, as shown in Figure 27, is near the surface (δT=0.01 °C). This value is only half of maximum of the Eulerian data. Again this is due to the fact that the fields sensed by the isobaric drifters are biased because these drifters seek out converging zones. The temperature variance decreases remarkably with depth.

3.2.6. Spectral Analysis

The covariance spectra of components of horizontal accelerations (du/dt and dv/dt) for isobaric drifters at different depths in the free convection case is shown in Figure 28. The spectrum has a peak at about 2×10^{-4} Hz near the surface where the sinking convergence zone has induced a spiral acceleration that has highly correlated du/dt and dv/dt. Near the bottom the horizontal acceleration also has a peak at about 8×10^{-5} as a result of the organized returning warmer water rotating anticyclonically.

Overall the numerical simulation indicates that the isobaric drifter measurements are heavily biased because they seek out convergence zones. In that respect the isobaric drifter may be useful for tracking the convective plumes. Further investigation is needed to establish a transform function from the biased statistical measurements of the isobaric drifters into the unbiased measurements of the Lagrangian drifters or Eulerian measurements.
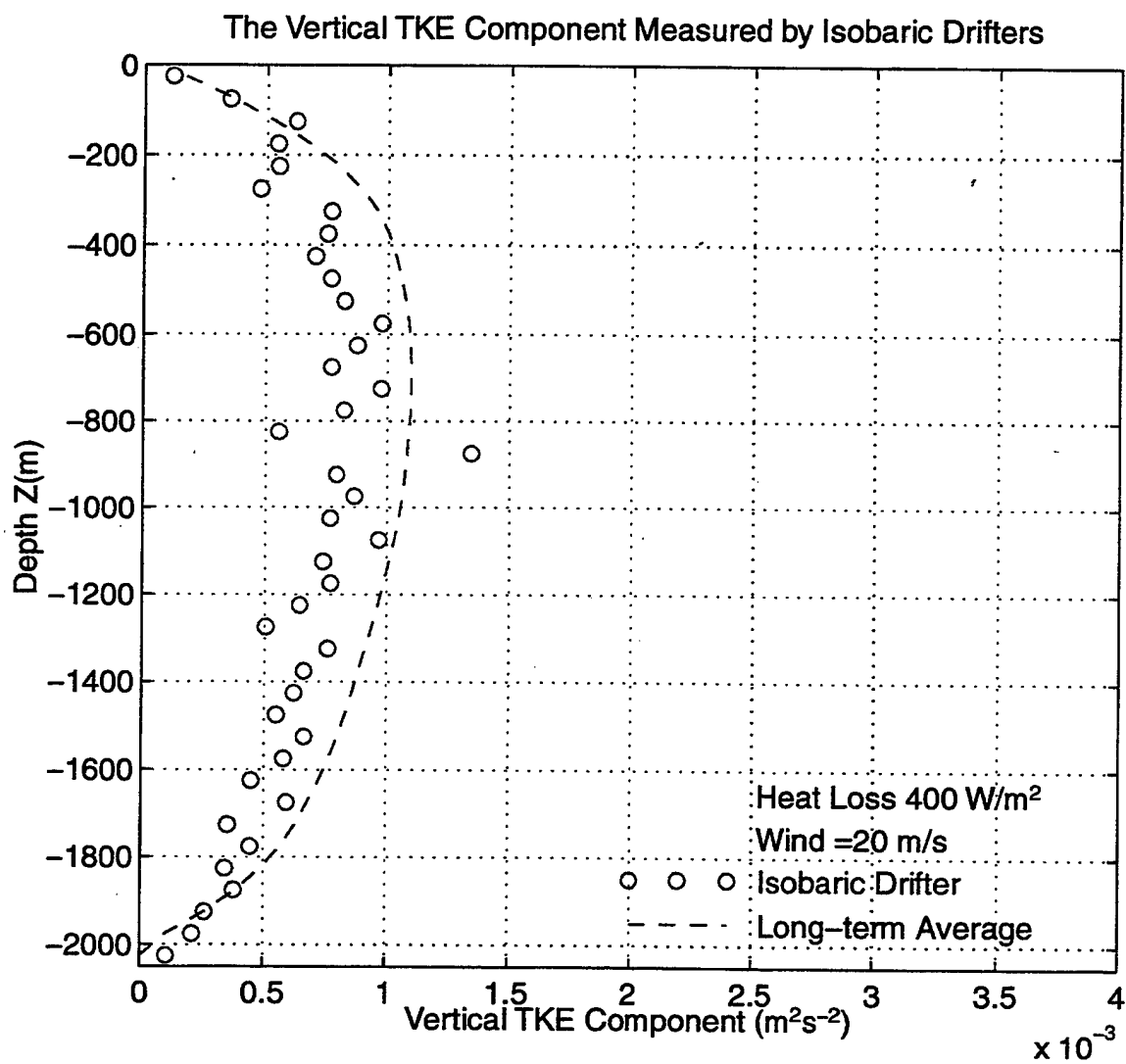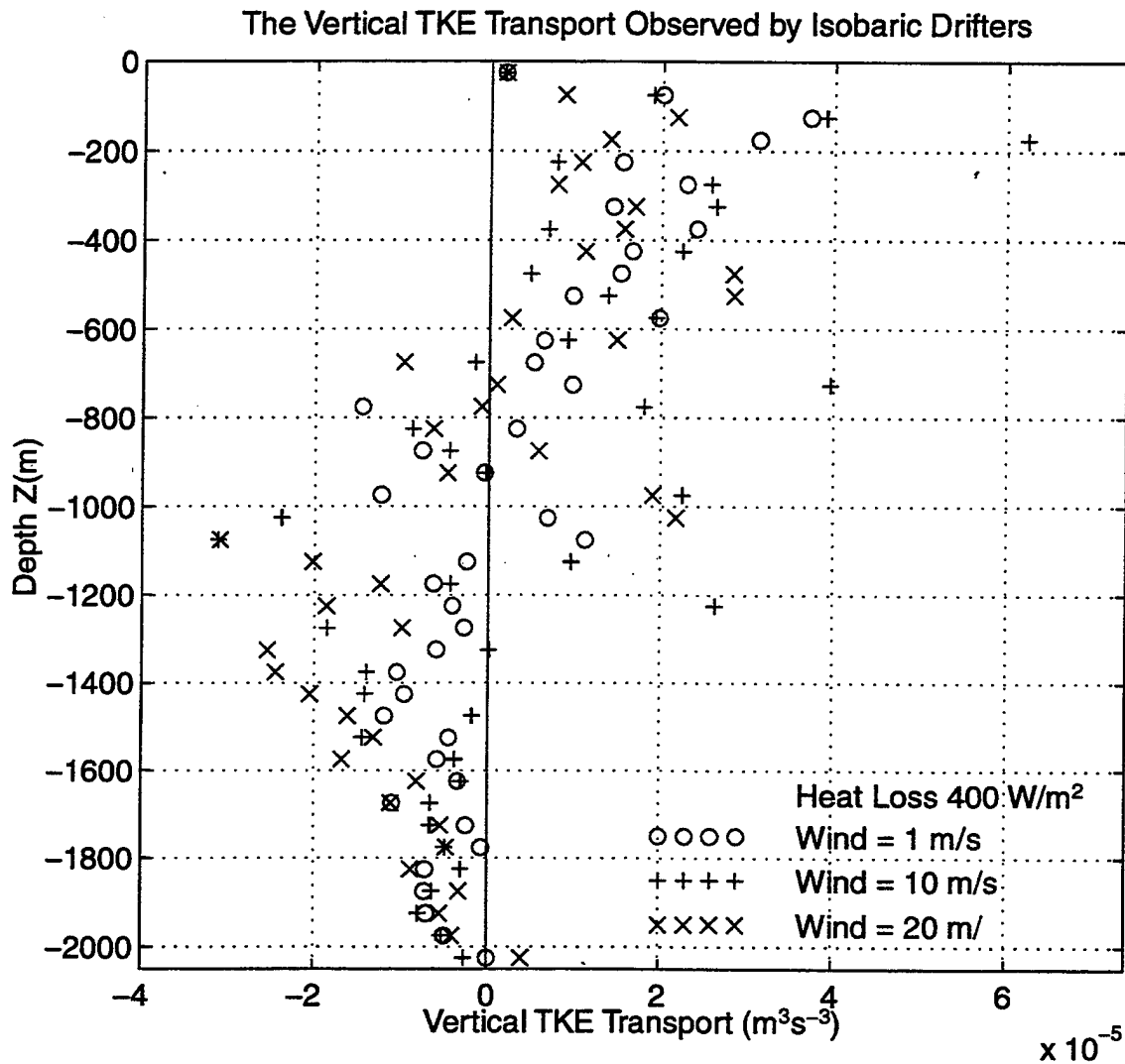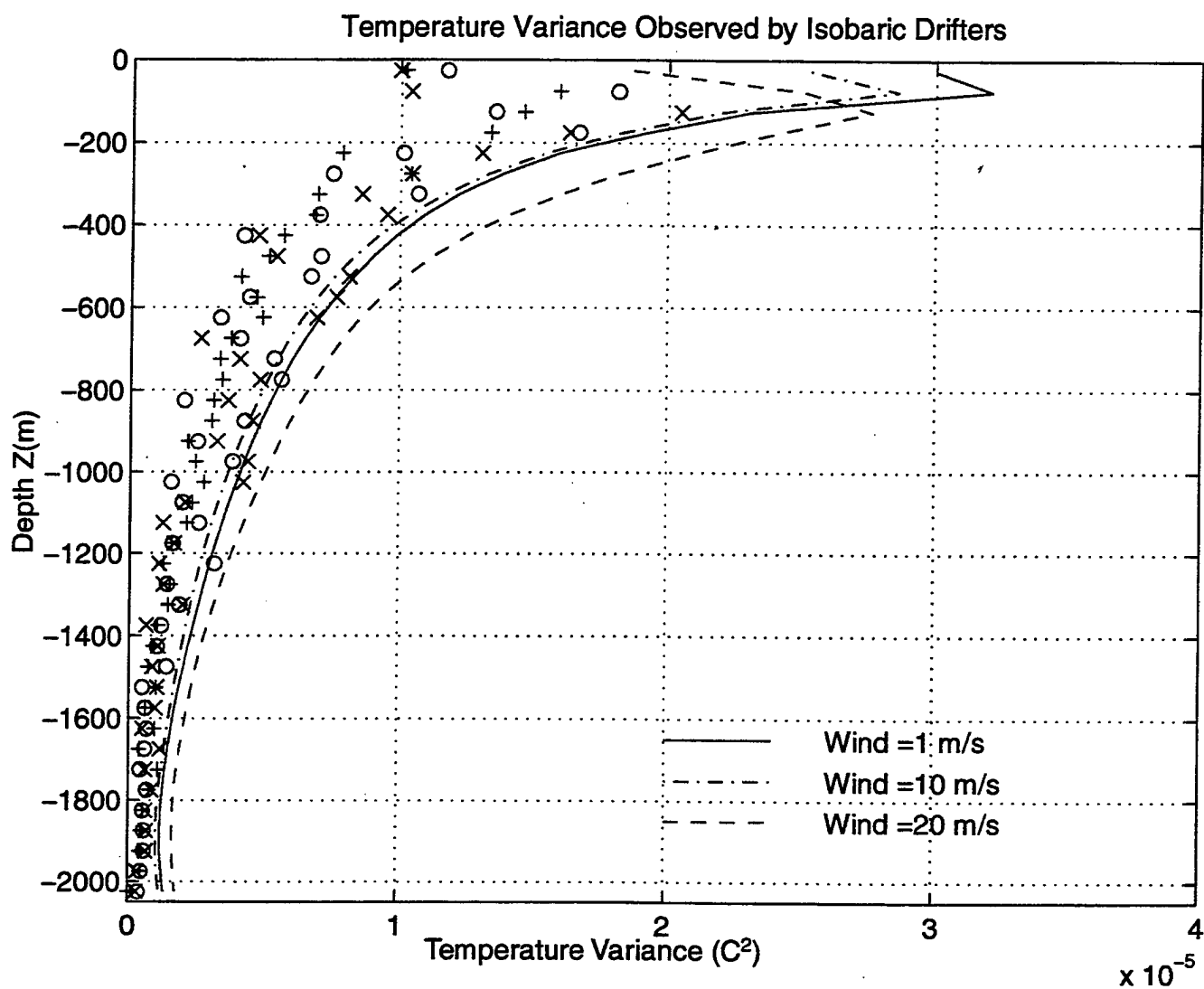
Figure 27. The vertical distribution of the temperature variance $\overline{T^2}$ observed by the isobaric drifters for all the three cases with 1 m/s, 10 m/s, and 20 m/s wind.
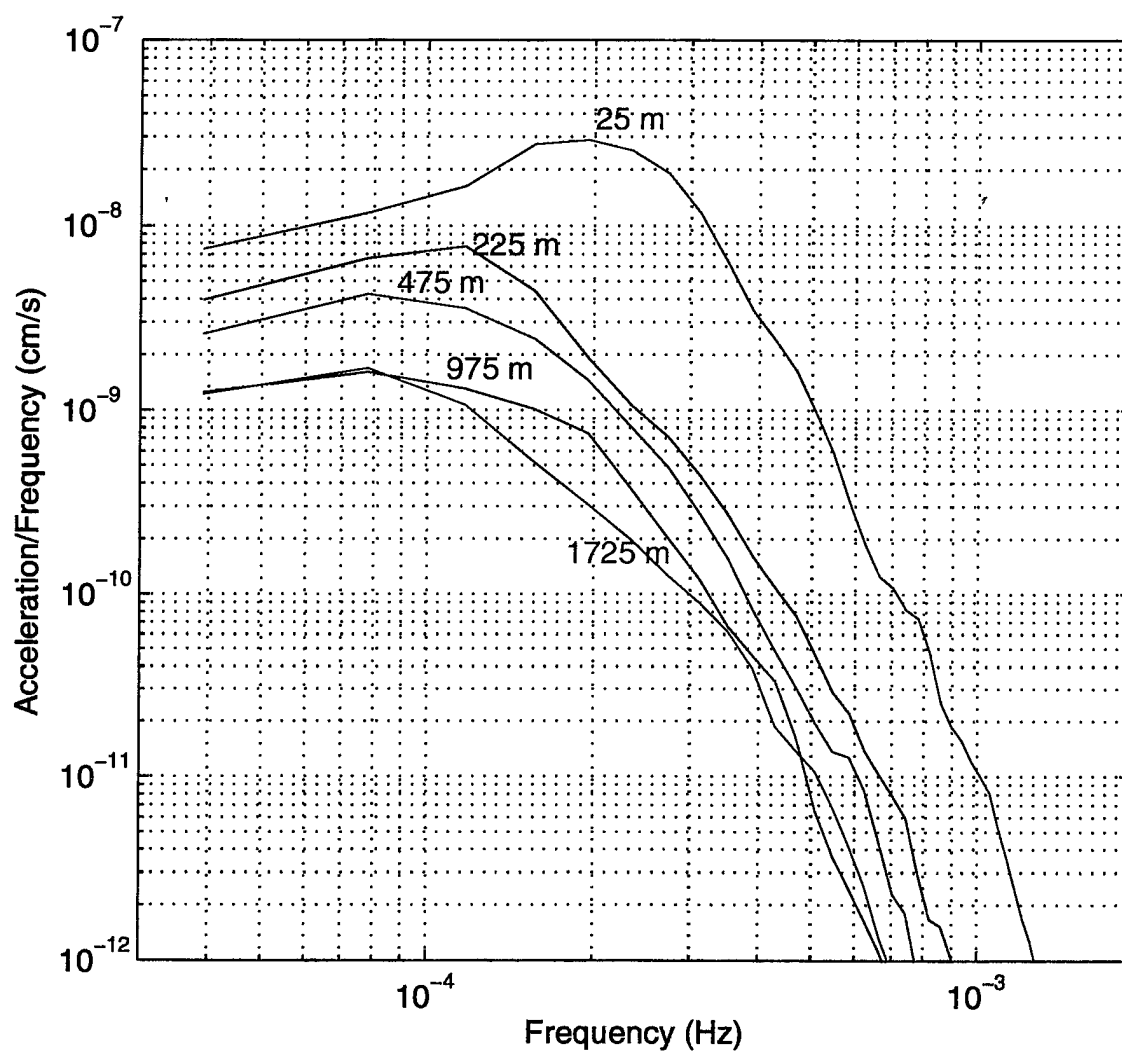
Figure 28. The covariance spectra of components of horizontal accelerations (du/dt and dv/dt) for isobaric drifters at different depths in the free convection case.

4. SUMMARY AND CONCLUSIONS

A Large-Eddy Simulation (LES) model was used to predict the fully-turbulent nonhydrostatic evolution of the oceanic flow fields that are typical of the Labrador Sea. The LES simulation indicates that either free or forced convection may dominate, depending upon the magnitudes of the wind stress, the net heat fluxed out of the ocean surface, and the mixed layer depth. Free convection dominates in the winter regimes of the periphery of the polar seas, especially in the very deeply-convecting regions of open water adjacent to marginal ice zones. Forced convection is more dominant in the stable ice-covered regions of the polar seas experiencing strong wind-stirring and kinetic energy exchange with the wind and the ice. Forced convection may be an important precursor to free convection, and the organized rolls of forced convection may help dilate the ice field to enhance heat and buoyancy exchange between the OPBL and the atmosphere.

We conducted numerical simulation of two types of idealized drifters: pure Lagrangian, and isobaric drifters. With the pre-computed LES velocity, pressure and salinity fields, the performance of the two drifter types was evaluated. The terms of the turbulent kinetic energy (TKE) budget, heat flux, and temperature variance observed by these drifters were evaluated and compared with the Eulerian calculations from the numerical experiments.

The numerical simulation indicates that the Lagrangian drifters can potentially resolve well the turbulent kinetic energy, the heat flux, and the turbulent transport, depending upon sensor accuracy on board the drifter. The Lagrangian drifter is also able to define the time-dependent vertical and horizontal scales of the convecting plumes. Compared with the Lagrangian drifters, the isobaric drifter sampling statistics are biased because these approximately fixed-depth drifters seek out convergence zones. The isobaric drifters may be particularly useful for tracking more energetic convective plumes near the surface and return flow at depth. The isobaric drifters are also able to measure maximum-likely vertical velocity. A combination of

Lagrangian and isobaric drifters may be best to both track the convecting plumes and to measure the heat flux correctly.

Many interesting questions remain and cannot be addressed by the idealized simulations presented here. How does a realistic Lagrangian drifter and a realistic isobaric drifter respond to the Labrador Sea convection with more realistic unsteady surface forcing? What are the effects of the variable large-scale oceanic flow field on the movement of the drifters that are not included in the LES simulation? What are the effects of Ekman pumping and suction? Scientifically we would like to determine the relative roles of forced (wind-driven) and free (buoyancy-driven) convection as a function of mixing depth (h), wind stress, and surface cooling in deep convection regimes like the Labrador Sea. Although we cannot answer these questions here, the present simulation does provide some new insight into the response of typical drifters to convective oceanic flow fields, and it forms a solid basis for future simulations of realistic drifters - with more specifications incorporated into the drifter models. Using drifter observations, and available ADCP Eulerian measurements, future research will be focused on simulation of observed oceanic conditions, forced by actual atmospheric analyses/observations during the Labrador Sea field experiment, 1997-1998.

5. REFERENCES

Arata, B., 1994: Deep convection in the Mediterranean Sea, Master's thesis, Naval Postgraduate School, Monterey, California, 70 pp.

Bedell, K., 1995: Detection of oceanic convection utilizing submarine-observed acceleration, M. S. thesis, Naval Postgraduate School, 84pp, in press.

Brugge, R., H. L. Jones, and J. M. Marshall, 1991: Non-hydrostatic ocean modelling for studies of open-ocean deep convection. In Deep Convection and Deep Water Formation in the Oceans, Ed. by P. C. Chu and J. C. Gascard, 325-340.

Carsey, F. D. and R. W. Garwood, Jr., 1993: Identification of modeled ocean plumes in Greenland Gyre ERS-1 SAR data, Geophys. Res. Lett., 20, 2207-2210.

Clarke R.A. and J.-C. Gascard, 1983: The formation of Labrador Sea Water, Part I: Large Scale Process, *J. Phys. Oceanogr.*, **13**, 1764-1778.

D'Asaro, E., 1994: Modeling deep convection. Workshop report on Oceanic Deep Convection ARI, 16 -17 February, Seattle.

Davis, R. E., 1982: On relating Eulerian and Lagrangian velocity statistics: single particles in homogeneous flows, *Deep-Sea Res.*, 38, S531-S571.

Davis, R. E., 1991: Observing the general circulation with floats, *J. Fluid Mech.*, 114, 1-26.

Davis, R. E., D. C. Webb, L. A. Regier, and J. Dufour, 1992: The autonomous Lagrangian circulation explorer (ALACE), *J. Atmos. Oceanic Tech.*, 9, 264-285.

Fox, D. G., and S. A. Orszag, 1973: Pseudospectral approximation to two-dimensional turbulence, *J. Comput. Phys.*, 11, 612-619.

Garwood, R. W., Jr., 1991: Enhancements to deep turbulent entrainment. In Deep Convection and Deep Water Formation in the Oceans, Ed. by P. C. Chu and J. C. Gascard, 197-213.

Garwood, R. W., Jr., S. M. Isakari, and P. C. Gallacher, 1994: Thermobaric convection, in The Role of the Polar Oceans in Shaping the Global Environment, O. Johannessen, R. Muench and J. Overland, Eds., AGU Monograph, Vol. 85.

Garwood, R. W., Jr., P. C. Gallacher, and P. Muller, 1985: Wind direction and equilibrium mixed layer depth: General theory. *J. Phys. Oceanogr.*, 15, 1325-1331.

Garwood and Harcourt, 1997: The oceanic planetary boundary layer in the Polar seas, Workshop Proceedings on Polar Processes in Global Climate, Cancun, Mexico, 13-15 November 1996, American Meteorological Society, 4.2, 4pp, in press.

Guest, A. R. W. Garwood, Jr., and R. Harcourt, 1995: Oceanic Planetary Boundary Layer (OPBL) Home Page (revised) on the Internet, http://www.oc.nps.navy.mil/opbl/.

Harcourt, R. and R. W. Garwood, Jr., 1994: Large eddy simulation of open ocean deep convection plumes, AGU Fall Annual Meeting, San Francisco, 5-9 Dec., *EOS Trans. Am. Geophys. Union*, 75s (44), 364-365.

Jones, H. and J. Marshall, 1993: Convection with rotation in a neutral ocean: A study of open-ocean deep convection, *J. Phys. Oceanogr.*, 23, 1009-1039.

Kearns, E. J. and H. T. Rossby, 1993: A simple method for measuring deep convection, *J. Atmos. Oceanic Tech.*, 10, 609-617.

Lazier, J.R.N., 1973: The renewal of Labrador Sea Water, *Deep-Sea Res.*, **20**, 341-353.

Legg, S. and J. Marshall, 1993: A heton model of the spreading phase of open-ocean deep convection, *J. Phys. Oceanogr.*, 23, 1040-1056.

Lemone, M. A. 1973: The structure and dynamics of horizontal roll vortices in the planetary boundary layer. *J. Atmos. Sci.,* 30, 1077-1091.

McDougall, T. J., 1987: Thermobaricity, cabbeling, and water mass conversion. *J. Geophys. Res.*, 92, 5448-5464.

Moeng, C.-H., 1984: A large-eddy simulation model for the study of planetary boundary-layer turbulence. *J. Atmos. Sci.*, 41, 2052-2062.

Moeng, C.-H., and J. C. Wyngaard, 1988: Spectral analysis of large-eddy simulations of the convective boundary layer, *J. Atmos. Sci.*, 45, 3573-3587.

Paluskiewicz, T., R. W. Garwood, Jr., and D. W. Denbo, 1994: Deep convective plumes in the ocean, *Oceanography*, 7, 37-44.

Schott, F. and K. Leaman, 1991: Observations with moored acoustic doppler current profilers in the convection regime in the Golfe du Lion, *J. Phys. Oceanogr.*, 21, 558-574.

INITIAL DISTRIBUTION LIST